Process Development and Characterization of Wire Arc Additive Manufactured Components

Submitted in partial fulfillment of the requirements for the award of the degree of

Doctor of Philosophy

By

T Sarathchandra Babu D

(Roll No.: 714124)

Supervisor:

Dr. M.J. Davidson

Associate Professor

DEPARTMENT OF MECHANICAL ENGINEERING

NATIONAL INSTITUTE OF TECHNOLOGY,

WARANGAL (TS), INDIA – 506004

2021

CERTIFICATE

This is to certify that the dissertation work entitled "**Process Development and Characterization of Wire Arc Additive Manufactured Components**", which is being submitted by **Mr. T Sarathchandra Babu D** (Roll No. 714124), is a bonafide work submitted to the Department of Mechanical Engineering, National Institute of Technology, Warangal in partial fulfillment of the requirement for the award of the degree of **Doctor of Philosophy in Mechanical Engineering.**

To the best of our knowledge, the work incorporated in this thesis has not been submitted elsewhere for the award of any degree.

Dr. M. J. Davidson	**Prof. A. Kumar**
Supervisor	Head,
Department of Mechanical Engineering	Department of Mechanical Engineering
National Institute of Technology	National Institute of Technology
Warangal- 506004	Warangal-506004

Dedicated

To

My beloved father Late Sri Dongari. Bangaraiah (Head Master)

APPROVAL SHEET

This Thesis entitled "**Process Development and Characterization of Wire Arc Additive Manufactured Components"**, by **T Sarathchandra Babu D** is approved for the **Degree of Doctor Philosophy**

Examiners

Supervisor

Dr. M. J. Davidson (Associate Professor. MED)

Chairman

Prof. A. Kumar, MED, NIT WARANGAL

DECLARATION

This is to certify that the work presented in the thesis entitled **“Process Development and Characterization of Wire Arc Additive Manufactured Components”,** is a bonafide work done by me under the supervision of Dr. M. J. Davidson, and was not submitted elsewhere for the award of any degree.

I declare that this written submission represents my ideas in my own words and where others' ideas or words have been included, I adequately cited and referenced the sources. I also declare that I have adhered to all principles of academic honesty and integrity and have not misrepresented or fabricated or falsified any idea/data/fact/source in my submission. I understand that any violation of the above will be a cause for disciplinary action by the Institute and can also evoke penal action from the sources which have thus not been properly cited or from whom proper permission has not been taken when needed.

T Sarathchandra Babu D.
Roll No.: 714124
Date:04-08-2021

ACKNOWLEDGMENT

I would like to express my sincere thanks and gratitude to my supervisor, Dr. M.J. Davidson, Mechanical Engineering Department, National Institute of Technology, Warangal, for his continuous guidance, support, enthusiasm, and motivation in my Ph.D. research work.

I am grateful to Prof. N.V. Ramana Rao, Director-National Institute of Technology Warangal who has been a constant source of inspiration for me. I thank Prof. A. Kumar, Head of the Department of Mechanical Engineering for his help and continuous encouragement to complete this work. I would like to express my sincere thanks to Prof. L. Krishnanand and Dr. Harikumar Voruganti (Mechanical Engineering Department), and Dr. Asit Kumar Khanra (Materials and Metallurgical Engineering Department), learned members of my Doctoral Scrutiny Committee for being helpful and generous during the entire course of this work.

My sincere thanks also go to former HODs, Prof. C.S.P. Rao, Prof. S. Srinivasa Rao, Prof. P. Bangaru Babu, Prof N. Selvaraj, and R. Narasimha Rao, Mechanical Engineering Department, National Institute of Technology, Warangal, for their encouragement, for providing access to the laboratory and research facilities. Without their precious support, it would not be possible to conduct this research.

I would like to thank my family members and relatives for supporting me throughout writing this thesis and my life in general.

Last but not the least, I sincerely express my deepest gratitude to my fellow scholars for their help and exciting discussions in research work.

T Sarathchandra Babu D
Roll No.: 714124
Research Scholar
Department of Mechanical Engineering
National Institute of Technology Warangal

ABSTRACT

Nickel based superalloy Inconel 625 has gained more attention in recent days because super alloy retains its properties at elevated temperatures up to the melting temperature. Inconel 625 is a solid solution hardened due to which it has superior high temperature mechanical strength, creep resistance, toughness, and anti-corrosion also. These unique capabilities of Inconel 625 properties make the promising replacement for specialized alloy steel in components used for fossil fuel energy systems that require high thermal and corrosion resistance. To date, researches have been focused on improving the high-temperature strength and room temperature ductility of the material. Nevertheless, the industrial application of this series of alloys is still limited by its room temperature brittleness, which also leads to a high manufacturing cost of this alloy.

In this connection, the present thesis work is focused on the development of Inconel 625 in the additive manufacturing process (AM). AM can produce customized and difficult to manufacture and difficult to machine parts in the most feasible way. AM can produce near-net-shaped components in less time. A cold metal transfer based wire arc additive manufacturing process is used to develop the Inconel 625 depositions. This production process saves a significant amount of time and money.

At first, the feasibility of the cold metal transfer process has been studied to attain the additive manufactured components. Initially, single depositions of Inconel 625 were investigated and the process parameters were optimized against bead characteristics such as bead width, bead height, penetration, and dilution. The optimum conditions were found to be current at 116.330 Amps, weld speed of 0.4633 m/min, and standoff distance of 5.115 mm. And from the results, it is proved that WAAM is capable of producing fully dense single beads without any cracks and defects. To satisfy the additive manufacturing process conditions, multi decision criteria analysis was performed on single bead deposition to know the single process parameter which satisfies the multiple decisions namely maximum bead width, minimum height, minimum penetration, and maximum microhardness. It was found that 100 Amperes current, 5 mm/min weld speed, and 0.3 mm standoff distance satisfies the combined objectives. Subsequently, an in depth study on the effect of process parameters and heat input on melting characteristics and solidification mechanism was investigated. Later, a detailed microstructure analysis was done on single bed depositions. In the microstructure, long columnar grains with primary dendrites were observed with laves phases.

Finally, using the optimized results from the single bead deposition study, a block of 150x75x75 mm^3 was prepared. Also, dissimilar deposition of Inconel 625 on the SS 304 block was made for the same dimensions. Compression, wear, and corrosion samples were extracted from the blocks, and tests were conducted as per the ASTM standards. From the results, it is observed that Inconel 625 deposited samples perform better than the dissimilar deposition samples. The present study confirms the adoption of the cold metal transfer process as an alternative to the laser-assisted additive manufacturing process. The bead geometry analysis reveals that the deposition characteristics are undoubtedly coherent with the layer additive process. The mechanical properties are comparable with the casting process, and microstructure has primary dendrite due to rapid solidification which enhances the deposition strength.

TABLE OF CONTENTS

LIST OF FIGURES

LIST OF TABLES

NOMENCLATURE

Abbreviations

AM	Additive Manufacturing
CAD	Computer-Aided Design
MAM	Metal Additive Manufacturing
RM	Rapid Manufacturing
RP	Rapid Prototyping
WAAM	Wire Arc Additive Manufacturing
LENS	Layer Engineered Net shaping
DED	Directed Energy deposition
GMAW	Gas Metal Arc Welding
TIGW	Tungsten Inert Gas Welding
EBW	Electron Beam Welding
PAW	Plasma Arc Welding
SAW	Submerged Arc Welding
CMT	Cold Metal Transfer
SMD	Structured Metal Deposition
DMD	Direct Metal Deposition
LMPD	Laser Metal Powder Deposition
LMWD	Laser Metal Wire Deposition

Nomenclature

A	Deposited Area (mm^2)
A_T	Total Area (mm^2)
B	Reinforcement Area (mm^2)
Cp	Specific Heat (J/Gr ˚C)
E_{em}	Electrode Wire Melting Efficiency (%)
E_{pm}	Plate Melting Efficiency Total (%)
E_{tm}	Melting Efficiency (%)
ΔH_f	Latent Heat Of Fusion (J/gr)
HI	Heat Input (KJ/mm)
I	Input Current (Amps)
S	Weld Speed (m/min)
T_0	Initial Room Temperature (˚C)

Greek Letters

V	Voltage (Volts)
η	Efficiency (%)
θ	Contact Angle (degree)
λ	Thermal Conductivity(w/m k)

Chapter 1

Introduction

1.1. Background

Additive **M**anufacturing (**AM**) or Rapid Prototyping(RP) or Rapid Manufacturing(RM) is an appropriate name to describe the technologies that build 3D objects by ***adding*** layer-upon-layer of material, whether the material is plastic, metal, concrete, or human tissue. According to ASTM standards (ASTM 52900), AM is defined as ***"the process of joining materials to make parts from 3D model data, usually layer upon layer, as opposed to subtractive manufacturing and formative manufacturing methodologies***"[1]. In recent days, additive manufacturing is everywhere in industrial applications and is becoming an increasingly essential technology for the direct manufacture of fully functional components and structures.

The AM technology uses a model generated in a 3D Computer-Aided Design (CAD) system which doesn't require process planning, or path planning to fabricate the part, while a careful and thorough analysis of the part geometry, type of tools and fabrication process, jigs, and fixtures, secondary machining requirements must be planned in other conventional manufacturing requirements [2]. The important features of these production lines are minimal waste, tool less production, significantly lower "time-to-market" and limited batch manufacturing.

The basic and general principle of these AM technologies is to build 3D structures through the incorporation of material in layers directly from computer-aided design (CAD) data. AM process flow consists of a computer which is having computer-aided design (CAD) software to create or design or develop a 3D structure, a fabrication machine, and raw material in the form of wire or powder. As soon as the 3D model is created in CAD software, the model geometry is converted into a tessellated triangulation file which is having the vertices data of the sliced model. Tool paths are then calculated from the slicing data thereby process parameters are identified to evaluate the path planning. To build the geometry, path planning data is uploaded to the AM equipment and hence the material is deposited or a 3D object is made in a layer upon layer sequence from the bottom-up.

A significant amount of material in the form of scrap and money can be saved by using AM technologies. The design and development of new products to promote in the market can also be promised to use the AM technologies in the manufacturing industry to produce complex shapes, prototypes, and functional parts. Existing techniques of manufacturing prototypes require highly skilled workers and usually take long periods, based on the geometrical complexity. the present machines can fabricate any type of complex geometries which are more difficult to manufacture in other conventional methods. Hence, it is noticeable that AM technology has the potential to reform and modernize the manufacturing and allied industries.

In earlier days, RP systems were developed used for prototyping and demonstration purposes. Later on, with the technology advancements in the AM machines and systems, fully functional metal parts were produced for real time applications. In rent days, researchers and industries are interested more in the fabrication of metal additive manufacturing (MAM) due to practical limitations in traditional manufacturing systems as well as promising achievements and performance of AM technologies. The MAM systems are classified based on the heat source used to melt the raw material i.e. Laser based (Selective laser melting, Powder bed fusion, Layer Engineered Net shaping, Directed Energy deposition) Arc based (Wire arc deposition with GMAW and TIG), Ion beam (Electron beam).

In present market scenarios, the industries are moving towards industry 4.0 to revolutionize the manufacturing sector. A report describes that the combination of additive manufacturing with Industry 4.0 can able to create fully customized, and dynamic products which can change the manufacturing sector in new marketing directions [3]. The Senvol database (shown in Figure 1.1) on MAM estimated the revenue of MAM to be $11000 by 2024. The premier industries like aerospace, automotive have greater demand for customized, complex, fully densified metal parts with higher structural integrity, accuracy at low production volumes. The hard to process and difficult-to-machine materials like Titanium, Nickel based alloys (Inconel, Monel, etc.), Stainless Steel, etc. are easy to fabricate and economical as well when compared with traditional manufacturing processes.

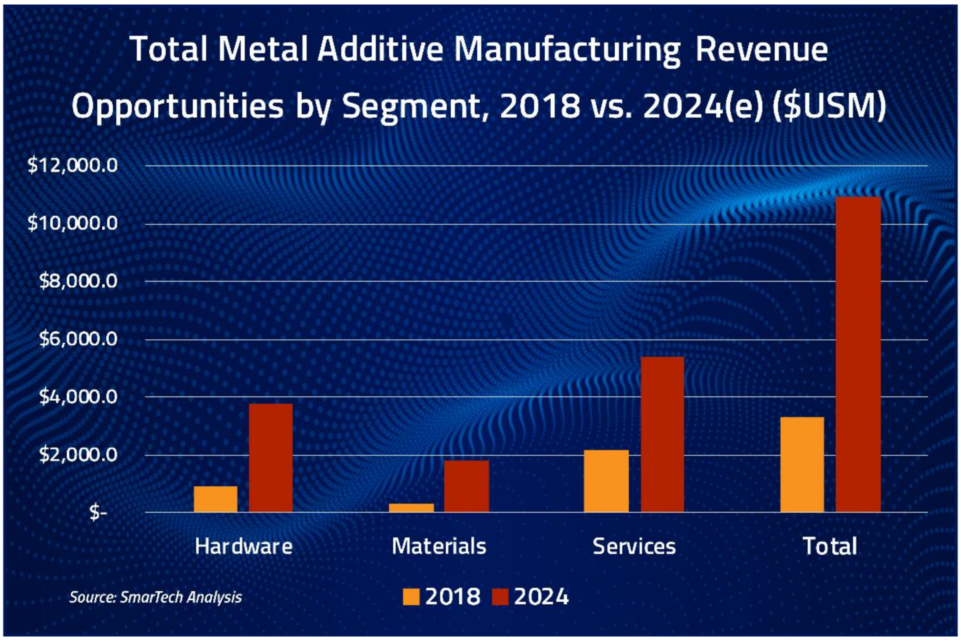

Figure 1.1 Metal additive manufacturing report by Senvol Database [4]

There are many highly automated powder-based MAM systems available in the commercial market which depends on laser and electron beam welding (EBW). Though MAM is widely used for the fabrication of a variety of metals and alloys, they have some critical issues with the existing machines. Those are

- Higher manufacturing costs due to lower deposition rates and processing speeds
- Lower machining efficiencies
- High investment cost
- Consumables availability
- Build volume is very less
- The prepared samples have low mechanical strength and therefore require post processing

Such processing restrictions make them unacceptable for some specific application and limits the fabrication of large components. To overcome these boundaries, high deposition MAM systems were developed using wire arc welding technology called Wire Arc Additive Manufacturing (WAAM) which uses an electric arc as a primary energy source to melt the materials for deposition. WAAM falls under the direct metal deposition category in AM processes. WAAM makes it possible to manufacture small scale to large scale production lines. Nowadays, it is expanding its wings in the MAM market. It has a low build and investment cost as compared to the laser assisted MAM machines. The main advantage of the WAAM system is, customized metal components are produced at higher deposition rates. Laser based and electron beam-based machines can deposit 2–10 g/min whereas arc based power sources can able to reach 50– 130 g/min due to energy efficiency in the arc deposition process. Arc based systems are 90% energy efficient while laser based depositions have 30% to 50% efficiency, and electron beam based systems are slightly higher than laser systems [5].

The arc based welding process such as Gas Tungsten Arc Welding (GTAW), Gas Metal Arc Welding (GMAW), Submerged Arc Welding (SAW), Plasma Arc Welding (PAW) can be employed as a WAAM system. In addition to the welding station, a separate mechanism has to be attached to facilitate movement in x, y, z directions during the deposition process. The movement might be given to the substrate table or the nozzle torch. Cold metal transfer (CMT) is an advancement of the GMAW process with controlled heat input. It has many advantages over regular GMAW processes like a higher metal deposition, low heat input, and arc ignition control mechanisms for different materials, etc., and hence CMT machines are widely used for the deposition of additively manufactured structures.

Materials like SS 304 and Inconel 625 are more resistant to corrosion, also are hard to machine, and difficult to customize for specific applications like marine engineering. Through conventional methods, it is very difficult to process and requires many machining operations. Hence, in the present work, processing of the hard to form metals through WAAM has been done to overcome the challenges posed by conventional methods.

1.2. The research challenges

WAAM has been in existence since the 1960s as high deposition rate arc welding systems in the form of submerged arc welding and gas metal arc welding processes. With the help of automation and computer control mechanisms shape melting and shape welding was used for higher deposition rates. In the 1990s, The Welding Engineering Research Centre (WERC) in Cranfield University initially developed structured metal deposition (SMD). To guarantee the highest quality requirements of the form welded components produced, several automated techniques and auxiliary equipment ensured online process controls. The automated production platform was embedded with a robotic controller with a motion and process control system. The machine included cleaning equipment to eliminate oxides and surface pollutants from the welded region, whereas water vapor nozzles and heating systems were used for temperature control. However, this research and development were motivated largely by the involvement of the heavy industries (e.g. power generation, nuclear, chemical, and petrochemical) in the manufacture of large modules, originally developed for fairly simple rotational geometries of thick-walled parts predominantly of low-alloy ferritic and martensitic steels. It was claimed that the industrial application of WAAM also demanded a high degree of awareness and technological competence in arc welding, residual stress engineering, and distortion. Shape welding technology was also posing considerable technological challenges, in particular in fabricating large parts in more complex forms and high strength materials. Scientific knowledge of various real-time process variables involved in WAAM production is crucial to managing microstructures, residual tension, and the part’s final configuration to achieve greater dimensional tolerances. The WAAM system's intellectual property, incorporated in the help control program, lies in the knowledge base of operation, materials, and architecture.

In the past, many studies on the relationship between process parameters and bead geometry in arc welding for single and multi-pass deposition have been carried out due to a growing need for automation and efficient welding in the last half century. Consequently, the data available for use in commercial WAAM systems are still inadequate. This is particularly valid for the newer versions of the welding method available for both GMAW and GTAW. The creation of specific process control models capable of evaluating the weld bead configuration and the plate fusion characteristics of the deposited beads from the welding process parameters is one of the key software components for the technical and commercial production of WAAM which would lead to widespread industrial application.

Advanced commercial arc welding technologies, such as cold metal transfer (CMT)which is an advancement of the GMAW process have become available to generate spatter-free welds at relatively low net heat input. Moreover, owing to greater control over melt pool solidification, these leading edge arc welding techniques will provide the opportunity for microstructure optimization.

For WAAM technology GMAW has major economic and technological advantages over GTAW practices, particularly for large-scale manufacturing. Owing to its higher deposition rate capacity of multiple kilograms an hour, as opposed to that of GTAW, the efficiency rates can be significantly improved with GMAW. Another key benefit of GMAW is the structural versatility provided by coaxial wire feeding, which enables additive patterning of more complex structures regardless of torch orientation, thereby enabling translational omnidirectional and spatial welding as well. In conventional GMAW, severe spattering conditions, arc instability, and imprecise weld bead placement are to be controlled.

1.3. Aims and objectives

The main aim of the present research is to investigate the deposition characteristics of Inconel 625 using a cold metal transfer based wire arc deposition process.

The objectives of the present study are

- To investigate the effect of process parameters on deposition characteristics and melting phenomena of Inconel 625 depositions
- To use multi decision analysis (Grey relational analysis) to evaluate the combined performance of the deposition characteristics
- To study the effect of heat input on microstructure and mechanical properties of Inconel 625 depositions
- To Fabricate WAAM structures using optimized parameters
- To prepare dissimilar material deposition of Inconel 625 on Stainless 304 in WAAM process
- To evaluate the mechanical, wear, and corrosion properties WAAMed Inconel 625 deposition

1.4. Originality and Major Contributions

The present investigations are intended to study the application of an in situ developed cold metal transfer based wire arc deposition process to fabricate Stainless steel 304 (SS 304) and Inconel 625 structures and to promote wire arc deposition as a full-fledged additive manufacturing process in the manufacturing of large and customized functional components.

Preliminary feasibility experiments were conducted to study the pool characteristics of single bead depositions at different input parameters. The effect of heat input on the single bead depositions was also investigated to study the behaviour of melt pool characteristics, later which are helpful for the development of multipass depositions. In the same way, microstructure and mechanical characteristics of the single bed depositions were investigated. Finally, with all the preceding outcomes and observations, additively manufactured components were fabricated. Especially the microstructure formations in the present study share the information of melting and solidification behaviour of additively manufactured structures at low heat input conditions. A step gradient type functionally graded SS 304 and Inconel 625 structure was made with optimized parameter levels. These attainments can enlighten the expansion of a laboratory equipped wire arc deposition process for the development of a consistent and reliable AM process.

1.5. Thesis outline

The dissertation has eight main chapters, including this introductory chapter.

Chapter 2 describes the history and development of additive manufacturing (AM) and the evolution of wire arc additive manufacturing (WAAM). Detailed literature has been presented on various WAAM systems with more emphasis on the cool metal transfer (CMT) process. The fundamentals of CMT deposition and related issues associated with the implementation of CMT as an AM machine have been addressed. Detailed literature was done on the effect of process parameters and heat input on deposited bead characteristics, microstructure, and mechanical properties for different materials processed in laser based systems as well as arc based systems.

Chapter 3 explains the experimental details such as CMT machine details, wire material, substrate plates, and consumables used for the research work. Also, the chapter describes the Wire EDM machining facilities, metallographic preparation methods, and microscopy equipment like Optical microscopes, Scanning Electron microscopes, and microhardness testing facilities. The main research findings of the present work are reported from chapters 4 to 8. Chapter 4 presents the results of the feasibility study of CMT for the WAAM system and process parameter optimization of stainless steel and Inconel 625. The results explain the effects of process parameters on bead characteristics which are later used for multilayer deposition structure. Chapter 5 presents the multi-decision analysis of bead characteristics using grey relational analysis to predict the optimum condition for the combined objective function. Chapter 6 focused on the effect of melting phenomena on deposition characteristics and bead characteristics. Chapter 7 describes the effect of heat input on microstructure and mechanical properties of single bead deposition tracks of Inconel 625. Chapter 8 describes the study on the multipass multi-track deposition of Inconel 625 and SS 304 deposition for the development of an additive manufacturing structure in the CMT process. Dissimilar deposition of stainless steel on Inconel 625 has been conducted to study the interfacial characteristics of dissimilar deposition processes. Chapter 9 gives overall conclusions of the research work and suggests some possible research directions that are needed to explore more for further consideration.

Chapter 2

Literature

2.1. Additive Manufacturing

Additive manufacturing (AM) is the process of fabricating a part by adding material layer by layer in the desired geometry to produce the final object. This method essentially uses the material in a molten state to add a layer at a time and upon solidification, it achieves the rigid shape. This method started back in 1983 and the defense and aerospace industry was among the first to adopt this technology around 1988 [3]. The materials used in this process are primarily polymers and metals. There are different types of AM processes that are developed based on energy sources that are used for the additive process such as filament heating, ultraviolet light, laser source, electron beam source, electric arc, etc. The basic steps that are to be followed for all the AM processes are outlined in Figure 2.1.

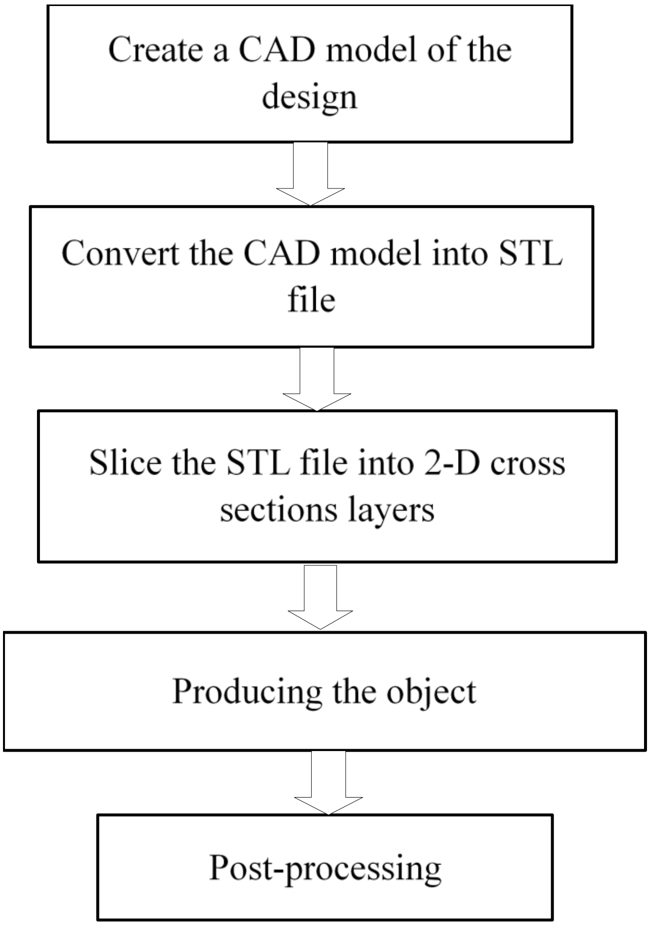

Figure 2.1 Additive manufacturing process flow chart

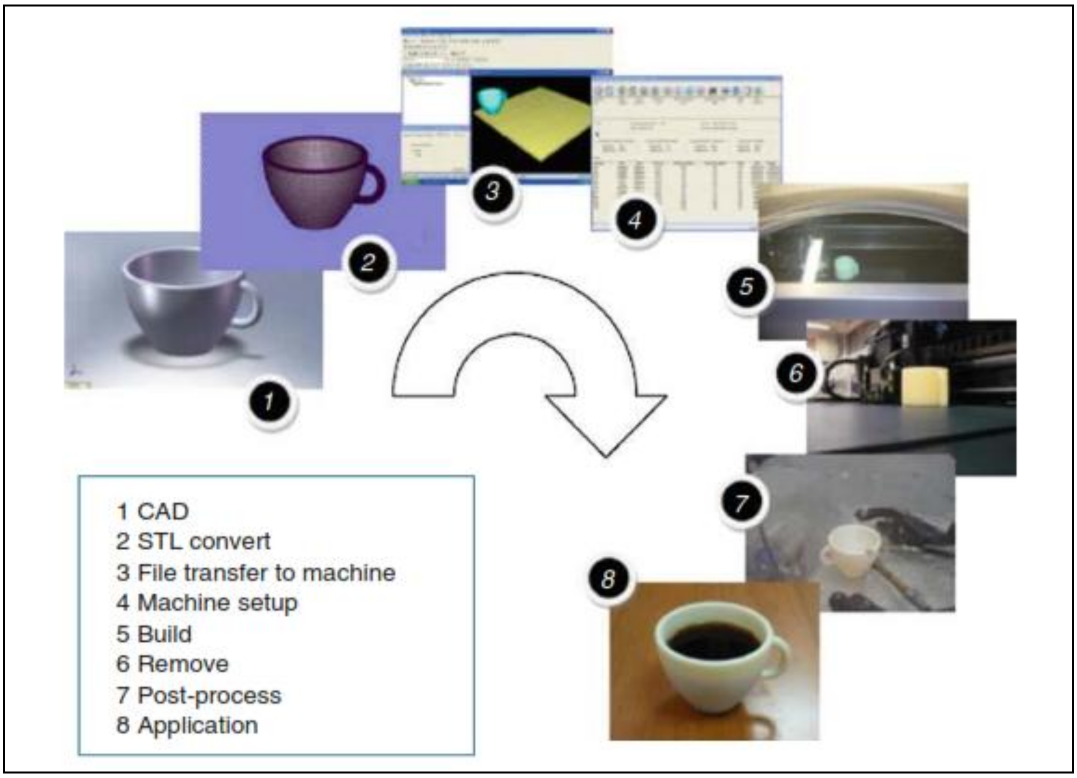

Figure 2.2 A sample demonstration of the additive manufacturing process [2]

Figure 2.2 demonstrates the various steps involved in the fabrication of a 3D model. AM as a process of manufacturing is very different from the conventional manufacturing methods like machining, forging, casting, etc. This method of manufacturing has many advantages over the other processes. One of the main reasons this method is used is because of the low buy-to-fly ratio it offers. Traditional manufacturing processes fail to do that because a lot of material is wasted in machining the required part from a larger block of metal. This causes a loss in terms of business as the materials used in the aerospace and defense industry are generally expensive. The aerospace industry these days uses a lot of carbon fiber reinforced parts because of their high strength and low weight. Along those lines, the use of titanium has increased significantly because of the electrochemical compatibility with carbon [4]. This increase in demand has resulted in a price rise which calls for a manufacturing process offering a low buy-to-fly ratio, such as AM. The flexibility of this method makes it very useful in manufacturing intricate parts and is therefore advantageous over the traditional manufacturing processes. For example, certain parts can be created with a cavity or a lattice structure inside without compromising the mechanical strength or the functionality as this would reduce the amount of material used, hence reducing the weight of the component and the cost of production [3]. This can be achieved easily by AM as it employs a layer-by-layer building approach whereas it can be challenging to machine those details from a piece of stock metal. The processes like electron beam melting and selective laser melting have been used in manufacturing the parts which have a very high level of detail, but the part size is limited due to the enclosed working chamber and low deposition rate [4]. Therefore, WAAM is the preferred method to produce larger components as the deposition rate is very high compared to the other methods and the manufacturing can be done without a closed chamber. This method offers a deposition rate of about 50-130 g/min which is one of the highest among all the AM processes.

Table 2.1 SWOT of Additive Manufacturing Technology

SWOT	HELPFUL	HARMFUL
INTERNAL	**Strengths** ✓ Enables a design-driven manufacturing process ✓ Allows for highly complex structure ✓ Provides a high degree of design freedom ✓ No assembly required	**Weakness** ≠ Reliance on plastics ≠ Slow build rate ≠ High production cost ≠ Postprocessing techniques are required ≠ Productions are discontinues ≠ Build size restrictions ≠ Reduced mechanical properties than the conventional process ≠ Limiting of Raw materials
EXTERNAL	**Opportunities** ✓ Aerospace ✓ Automotive ✓ Medical ✓ Bio Printing ✓ Nano Fabrication ✓ Marine, Oil& gas ✓ Building Construction	**Threats** ≠ 3D printers are energy hogs ≠ IP and licensing deals ≠ Gun control loopholes, Weapons can be 3d printed ≠ Bioprinting ethics and regulation ≠ Possibility of 3D printed drugs

The SWOT (Strength, Weakness, Opportunities, and Threats) analysis of AM technologies is presented in Table 2.1.

Additive manufacturing is promising due to the advantages that it offers over traditional manufacturing processes. This method is known to have worked well with metals and polymers. It offers a much lower buy-to-fly ratio as compared to conventional manufacturing as the material is added only where it is needed, unlike the conventional manufacturing processes where it is machined out from the places where it is not needed.

Other conventional methods involve the assembly of different subcomponents manufactured separately. In this case, the structural integrity of the part is affected whereas in additive manufacturing the entire part can be produced with the end product being a single piece of metal since this method follows a layer by layer approach of building. This reduces wastage of material significantly, so the material investment may be lower as compared to the conventional methods. This method is also known to be environmentally friendly as the wastage of material is relatively lower than the traditional methods. The additive manufacturing technology has been defined by BSI (British Standard Institute), ISO (International Organization of Standardization), and ASTM (American Society for Testing and Materials) together and has been divided into seven different categories by the ASTM International Committee F42.

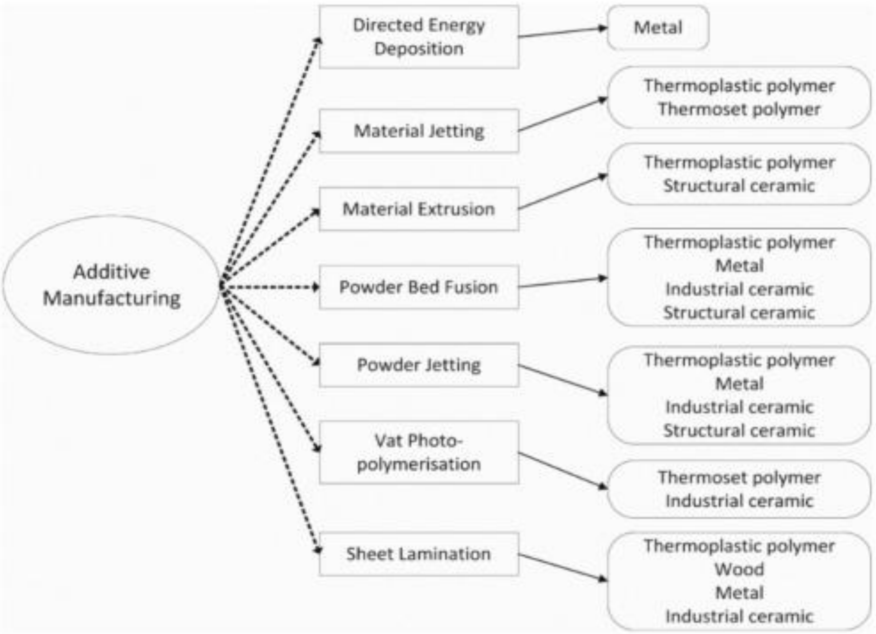

Figure 2.3 Classification of AM processes with respective material handling capabilities [7].

Figure 2.3 shows the different methods of additive manufacturing. The diagram shows that four out of all the seven methods are capable of producing metallic parts out of which WAAM falls into Direct Energy Deposition method. Methods like powder bed fusion are capable of building parts with a very high level of accuracy but have a very low deposition rate and the part size is also limited. WAAM however has a very high deposition rate at the cost of a low level of accuracy. This problem is overcome by using minimal machining after material deposition.

2.2. Metal based Additive Manufacturing (MAM) process

In recent years, there has been an increase in demand for RM applications and systems that have the capability of producing fully useable components composed of high structural integrity and within specified tolerances. There is a necessity to convert standard RP equipment into long-lasting freeform manufacturing systems capable of producing completely functional components from polymers, plastics, ceramics, and a wide range of composites. [6]. This manufacturing idea is evolved from Rapid Prototyping & Tooling (RP&T) advancements, which are today known as Additive Manufacturing (AM). AM systems combine high productivity and low cost manufacturing with the efficiency of what is known as RP's "3F's" (Form, Fit, and Function). Shape, construct and work on thick components for production or restoration. A wide range of Metal Additive Manufacturing (MAM) methods is presently available, most commonly in the form of powder beds.

MAM may be divided into two major groups depending on the physical condition (or form) of the raw materials used in processing: powders and a combination of powder-wire-based methods. A laser beam is scanned across the surface of a metallic powder bed, selectively heating and fusing layers of sequential cross sections of a CAD model until a 3D item is produced. The manufacturing process includes injecting blown metal powder or solid wire into a thin melt pool produced by laser or electron beam heating, where the material melts and quickly solidifies into metal layers. Electron beam and laser heating sources are the most widely utilized heating sources in powder-based MAM machines. Some of the existing and commercially available machines in the market are listed in Table 2.2. Fine metal powders can be used to create, remanufacture, or clad extremely small and highly complex metal parts, allowing for weight savings or additional functionality to existing or future components (Reninshaw made metal AM parts in Figure 2.4).

Figure 2.4 Examples of laser processed additive manufactured parts developed by Reninshaw ([7])

Table 2.2. Commercially available MAM machines [8]

Machine model	Process Technology	Category	Build volume	Origin	Price* (Approx.)
3D Systems DMP FLEX 100	Direct Metal Printing	Powder bed fusion	100 x 100 x 90 mm	United States	\$250,000
Additec µPrinter	Laser Metal Deposition	Directed Energy Deposition	160 x 120 x 450 mm	Germany	\$90,000
Coherent CREATOR	Selective Laser Melting	Powder bed fusion	ø 100 x 100 mm	Germany	\$100,000
Desktop Metal Production System	Single Pass Jetting™	Material Jetting	490 x 380 x 260 mm	United States	\$420,000
Desktop Metal Studio System	Bound Metal Deposition™	Extrusion	300 x 200 x 200 mm	United States	\$120,000
Digital Metal DM P2500	-	Binder Jetting	203 x 180 x 69 mm	Sweden	\$700,000
EOS M 100	Direct Metal Laser Sintering	Powder bed fusion	ø 100 x 95 mm	Germany	\$350,000
Formalloy L-Series	-	Directed Energy Deposition	200 x 200 x 200 mm	United States	\$200,000
GE Additive Arcam EBM Spectra L	Electron Beam Melting	Powder bed fusion	ø 350 x 430 mm	United States	> \$250,000
GE Additive M2 Series 5	Direct Metal Laser Melting	Powder bed fusion	245 x 245 x 350 mm	United States	> \$250,000
MarkForged Metal X	Atomic Diffusion Additive Manufacturing	Extrusion	300 x 220 x 180 mm	United States	\$99,500

Pollen AM PAM Series MC	Pellet Additive Manufacturing	Extrusion	ø 300 x 300 mm	France	€ 70,000
Rapidia Metal 3D printer	Water-based metal paste extrusion	Extrusion	200 x 280 x 200 mm	Canada	> $100,000
Renishaw RenAM 500E	Selective Laser Melting	Powder bed fusion	250 x 250 x 350 mm	United Kingdom	> $250,000
Sisma EVEMET 200	Laser Metal Fusion	Powder bed fusion	ø 200 x 200 mm	Italy	> $250,000
SLM Solutions SLM 125	Selective Laser Melting	Powder bed fusion	125 x 125 x 125 mm	Germany	$400,000
SPEE3D LightSPEE3D	Supersonic Deposition	Material Jetting	300 x 300 x 300 mm	Australia	$650,000
TRIDITIVE AMCELL	Automated Multimaterial Deposition®	Extrusion	ø 220 x 330 mm	Spain	> $250,000
TRUMPF TruPrint 1000	Laser Metal Fusion	Powder bed fusion	ø 100 x 100 mm	Germany	$250,000
Velo3D Sapphire	Laser Metal Fusion	Powder bed fusion	ø 315 x 1000 mm	United States	> $250,000
Xact Metal XM200C	Selective Laser Melting	Powder bed fusion	127 x 127 x 127 mm	United States	$80,000
XJet Carmel 700M	NanoParticle Jetting™	Material Jetting	500 x 140 x 200 mm	Israel	> $250,000

2.2.1. Laser and electron beam based MAM process

Metal additive manufacturing has gained popularity due to its capacity to create components at a low cost and with a low buy-to-fly ratio. Metal additive manufacturing processes vary based on the energy source and the kind of raw materials utilized. AM systems based on lasers and electron beams are frequently utilized in engineering applications.

2.2.1.1. Laser assisted powder deposition systems

Laser engineering net shape (LENS)[9], laser direct metal deposition (DMD) ([10][11][12]), selective laser melting[13], laser rapid manufacturing [14], [15] laser sintering [16] are some of the most popular laser beam systems used for the fabrication of additive manufacturing components. The typical laser deposition systems are depicted in Figure 2.5.

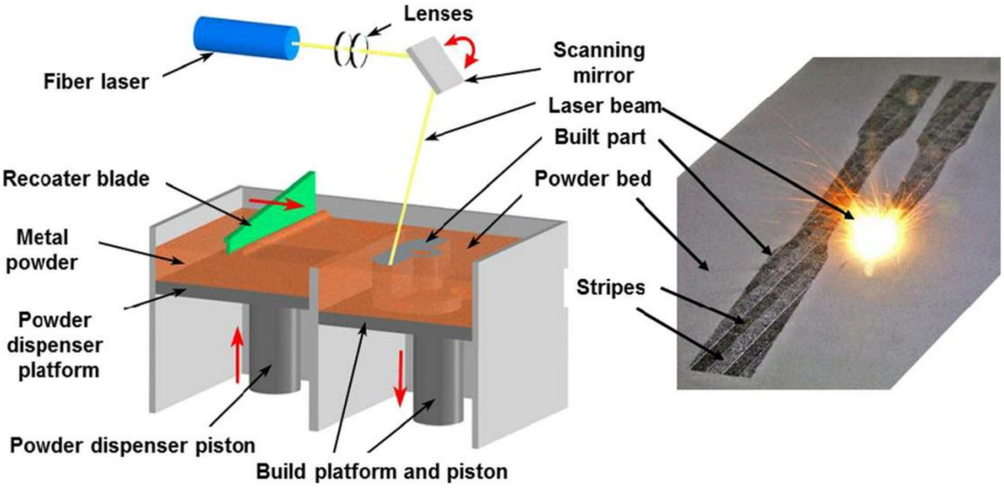

Figure 2.5 Laser powder deposition system [17]

A technical and safety requirement of these systems is the use of an environmental chamber with a regulated atmosphere that is filled with an inert gas such as argon to prevent contamination. These methods also require the powder bed to be warmed in the processing area to avoid thermal distortion and improve layer consolidation. Due to the system complexity and machinery developments, a significant practical challenge must be addressed to minimize the related building cost of such systems.

These main drawbacks in the laser powder systems are summarized as follows:

- Low production speeds and restricted build volumes.
- Metal powder capture efficiency is generally 10-33 percent.
- Because of the tiny size of the powder particles and their huge specific surface area, the metal powder feedstock has a high sensitivity to contamination by oxygen, nitrogen, carbon, hydrogen, and other contaminants.
- Poor quality powder feedstock can have a negative influence on the as-deposited material's corrosion and mechanical performance.
- Metal powders should have flowability, good packing density, and be spherical

- Metal powder recycling is still problematic, especially when different powders are mixed. When they interact with the open atmosphere it may form compounds of oxygen
- Due to gas porosity and a lack of fusion flaws, the deposited material has low integrity.
- Post-processing procedures, such as hot isostatic pressing (HIP), are frequently required to enhance the final density and strength of the components
- Energy efficiency is low, hardly 30% of the laser energy is utilized to melt the powder particle. In cases of aluminium and copper, beam reflections can reach 98 percent.
- Health and safety issues while working with the use of high-powered lasers, as well as the handling and/or exposure to hazardous reactions of fine particles
- Investment and running cost is too high

In addition to the powder based systems, in recent years significant efforts have been made to use powder and wire feeding systems to overcome the foregoing difficulties and disadvantages found when using powder feed alone.

2.2.1.2. Laser assisted wire and powder deposition systems

In recent days, many researchers and industries are focused on wire based approaches. Wire based deposition provides a cleaner environment and has greater material efficiency whereas powder assisted deposition always has material loss while feeding through the material delivery system. As opposed to the powder particles, the usage of wire offers a smaller specific area of the filler material, lowering the danger of contamination during deposition. In addition, preheating the wire allows for significantly faster deposition rates, and simple wire feeding mechanisms may be utilized instead of the complicated nozzles required for laser/powder systems. Adjustments in process parameters, such as the location of the wire tip relative to the weld pool, influences the wire feeding systems. Droplet formation during the transfer of molten wire or, on the other hand, stubbing of the wire tip against the previous layer are both frequent issues that have significant consequences for the ultimate product. If the wire is not entirely melted, the operation may be halted. To maintain process stability and material integrity, online control is required. [18].

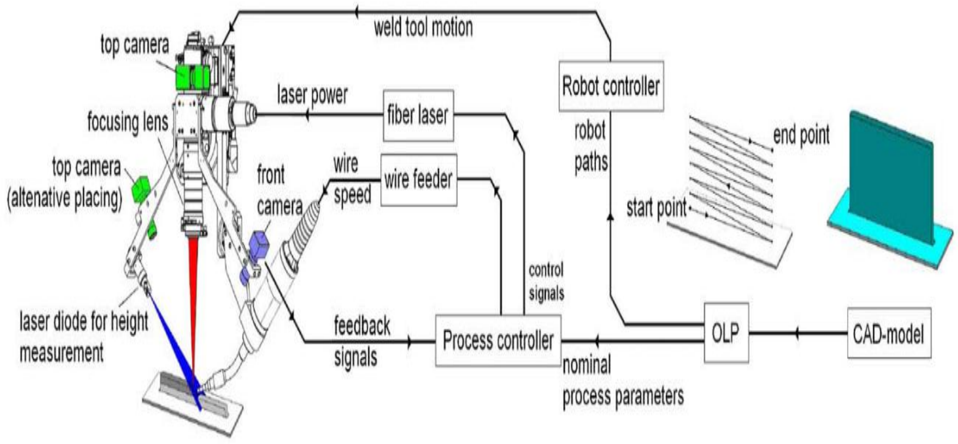

Figure 2.6 Laser wire deposition system [18]

However, it appears that though laser wire feed systems(Figure 2.6) have significant advantages to develop additive manufacturing components, there are few drawbacks which includes

- Wire has low tensile strength and is sensitive to alignment and orientation concerning the laser beam
- Because of wire bending and vibration produced by variations in wire tension during feeding, consistent and reproducible results are difficult to achieve
- Because of changes in the wire absorption coefficient and the shadowing effect on the surface, the coupling of laser energy into the material is inefficient and difficult to manage
- Because of wire feeding via a lateral feed nozzle, the process is directionally dependent.

Several researchers have tried to study the application of conventional arc welding techniques, such as gas metal arc welding (GMAW) and gas tungsten arc welding (GTAW), for the near net shape processing of 3D metal components with high mechanical strength. Because of its numerous benefits over traditional fabrication processes like casting, forging, and machining, wire and arc additive manufacturing (WAAM) has received significant attention.

2.2.1.3. Electron beam based systems

NASA Langley Research Center created the electron beam freeform fabrication (EBF3) technique to directly produce complicated geometry components, add structural features to manufactured pre-forms, and allow the creation of innovative graded property materials. The metal wire is introduced into a molten pool produced on the surface of a substrate by a focussed electron beam during the EBF3 process. Component geometry is accomplished by moving the substrate relative to the beam and building the part one layer at a time [19].

Development of materials utilizing EBM technology is of significance because it may generate dense components with lower residual stresses than related powder fusion techniques like selective laser melting, and therefore parts can be used in their as-fabricated form depending on their application. In EBM, material processing is entirely controlled by the machine, and the user receives limited input on the workflow. Temperature feedback in commercial EBM systems consists of a single thermocouple that senses the temperature at a single location below the build platform. Furthermore, the powder bed fusion technique is a layer-by-layer process, the temperature measurements are not indicative of the layer being produced and do not indicate any influence on the part's quality. It is critical to know the surface temperature during fabrication when setting processing parameters or attempting to regulate the microstructure of a material. Knowing the temperature for each process step allows the operator to change system parameters to reach the required surface temperature for a customized microstructure, enabling certification, and offer a mechanism for in situ monitoring. [20].

2.2.2. Arc based MAM process

Among the three energy sources (laser based systems, electron beam based, and arc based systems) arc based systems have higher material efficiency and high deposition rates. They are also better suited for continuous and uncluttered material supply. Hence, they are most suitable for large components.

In the arc deposition process, a layer consists of meatal beads is deposited on a substrate or a target surface and a component is made through multipass or layer upon layer strategy. The process may be GMAW, TIG, and MIG. A computer-controlled machine can be used to direct the deposition path as per the requirement. The key benefit of wire and arc manufacturing additive manufacturing is the high deposition rate, with the added freedom of selection of power source which can save production cost and lead time.

In recent days, various research works have been attempted to prove the potential of wire arc deposition systems as additive manufacturing for various engineering applications and also to develop different materials to accommodate future challenges.

Wire Arc Additive Manufacturing (WAAM) belongs to the directed energy deposition process in which the heat source is electric arc and wire is fed through the nozzle. WAAM can be attained by processes like Plasma Arc Welding [21], Gas Tungsten Arc Welding[22], and Gas Metal Arc Welding [23]. There are various advantages for WAAM over laser-assisted and plasma-assisted additive manufacturing processes, in terms of the capital cost of machines, material flexibility, etc. A simple welding station consists of an energy source, welding torch, wire feedstock, a robotic system to control the deposition bed, and an inert gas supply unit. WAAM produces higher deposition rates than powder-based additive manufacturing systems.

The flexibility to alter deposition parameters enables the WAAM to deliver the customized properties at preferred regions. Three types of metal transfer phenomena occur in the arc deposition process. They are short circuit transfer, globular droplet transfer, and spray transfer. Short circuit transfer is suitable for thin walls production because of low arc current levels and smaller weld pools. In the globular transfer process, the material transfer happens due to gravity at mid-level arc current conditions, and spray transfer suitable for thicker walls and has more penetration occurs at high arc current.

A WAAM system consists of a motion system, a welding system, and a wire feeder. The motion system can be a robotic arm or a CNC machine. A communicator is needed to have the motion system and the welder connected and be able to function in sync. Figure 2.7 displays a schematic diagram of WAAM showing the welding torch, wire feeder, argon gas tank, and the working chamber. Typically, the chamber is circulated with argon from an additional tank, but in the current research, argon was only supplied through the nozzle in the torch, so the part size wasn't limited as the welding was done in an open space.

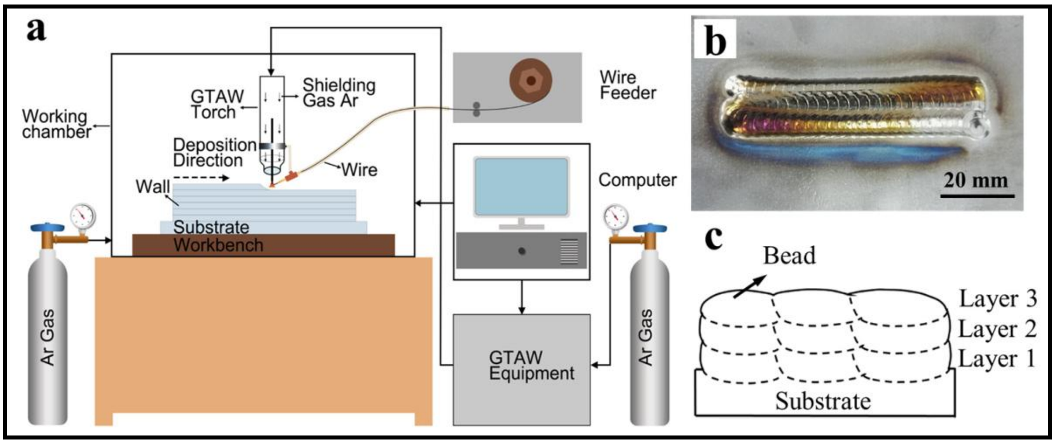

Figure 2.7 Schematic diagram of a) a typical WAAM system b) Deposited sample c) Interlayer deposition process

The term WAAM became widely accepted in the last decade, but the basic concept of the process dates back to 1920 [7]. WAAM in simple words is 3D printing using the method of welding. MIG or TIG welding methods can be used to make parts using WAAM technology. The technology is as simple as welding since all the equipment needed in this process is nothing more than what the conventional Tungsten Inert Gas (TIG) or Metal Inert Gas (MIG) welding needs. The only major difference is that a motion system is needed which can function according to the instructions fed into a computer that has to have the capability of controlling the motion system and the welder together in sync. This method is cheaper when compared to the other conventional AM processes as the requirement of any special material or tool is eliminated. This can also produce any part with almost the required shape and has no size limit. As mentioned earlier the deposition rate that can be achieved in this process is 50-130 g/min. This reduces the production time as it is much faster as compared to the other AM processes like powder bed fusion. Some researchers have found out that some mechanical properties can be of the same level or exceed in some cases for wrought products of that material [8]. This process however has some disadvantages which need to be dealt with. Since there is a huge amount of heat input during deposition, there is some amount of deformation when the part cools down [9]. Since the temperature in the build direction is high, the plate tends to bend in the direction of the build when cooling occurs. Clamping of the plate could be a solution to avoid the deformation but it gives rise to another problem which is residual stress when unclamping. This problem can be solved by using a symmetrical building approach. In this process, the same part is built on both sides of the plate. This cancels out the residual stress caused by the part built on the other side of the plate. Another benefit of this process is that two symmetrical parts can be built on either side of the plate.

Another major challenge that arises by using TIG welding in this process is the path planning of the build. With MIG welding, the torch can be moved back and forth without any rotation as the wire itself is the electrode whereas in TIG welding, the wire must be fed from the advancing side and the electrode should be on the trailing side. The angle of the wire feed and the point where the wire enters the arc should be set carefully to produce a good quality bead surface.

2.2.3. The cold metal transfer process

The cold metal transfer (CMT) process is an advancement of the gas metal arc welding process with less heat input, better weld quality, and fewer spatter disturbances as compared to other welding processes [24]. The key factor involved in CMT technology is an automatic wire feed controller. In CMT, a reciprocated wire feed mechanism is incorporated in the electrical process, and the arc initiation and short-circuiting stages are synchronized by the electrical controller [25]. Figure 2.8 shows the material transfer in the CMT process.

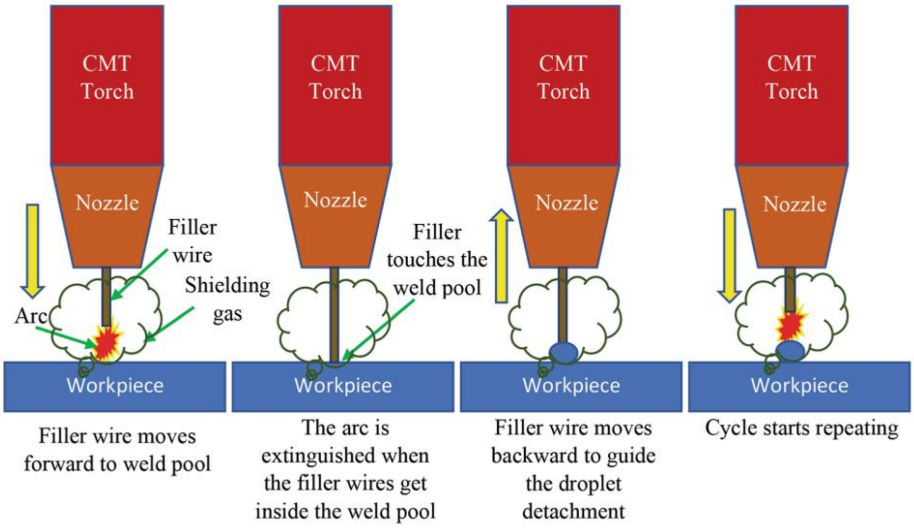

Figure 2.8 Cold metal transfer process [26]

Different types of waveforms are available (see Figure 2.9) in recently developed cold metal transfer machines to accommodate future developments in materials research. The CMT process is a promising method to employ in the AM application because of its good features in terms of reduced spatter and automated adjustment of contact tip to work distance. Cong [27] has investigated arc modes of the CMT process on porosity and bead characteristics. Hence, the present authors used the CMT machine for experimentation.

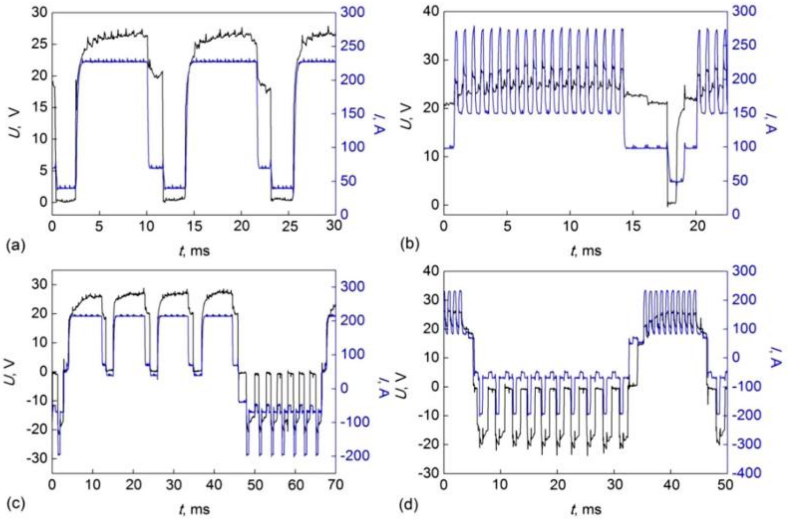

Figure 2.9 Waveforms in CMT process a) Standard CMT b) CMT P (Pulse) c) CMT ADV (Advanced) d) CMT PADV (Pulse Advanced)

2.3. Materials overview

In the present research work, Nickel based superalloy Inconel 625 and high corrosion resistance steel grade stainless SS304 were used for the experimentation. The two selected alloys have superior qualities in terms of mechanical strength and are found in many engineering applications.

2.3.1. Inconel 625

Inconel 625 (IN625) is another nickel superalloy widely used in harsh conditions. It is an anti-corrosion, and oxidation-resistant material and has outstanding strength and toughness and retains its strength up to a temperature of 1093°C because of solid solution strengthening. These materials can sustain at a working temperature near the melting point. Hence, superalloys are anti-corrosive, anti-oxidant, and withstand fatigue and creep loads. Nickel superalloys are used in most significant engineering applications because they provide an outstanding combination of mechanical strength and corrosion resistance with better metallurgical characteristics. Nickel based superalloys are used for heat exchangers, rockets, and turbines, etc. [28]

The following are the main reasons for these superalloys to have exceptional characteristics:

(a) Superalloys have a face-centered cubic structure in the microstructure due to which creep rate is low and phase transformations are restricted

(b) Solid solution strengthening

(c) The formation of precipitation phases

(d) Controlled solidification

2.3.2. Stainless steel

Austenitic stainless steels are extensively used in nuclear applications such as reactor coolant pipes, valve bodies, spacer column assembly, control rod drive mechanism, and vessel internals[29]. Stainless Steel 304 is a low-carbon austenitic stainless steel that is also known as ultra-low carbon stainless steel. The SS 304 metal products could perform well in high temperature conditions due to their good formability, corrosion resistance, excellent plasticity, and fabricating performance is also excellent. Traditional manufacturing methods are limited for the 304 components manufacturing due to the long manufacturing cycle and high cost. [30].

2.4. Design of experiments and response surface methodology

Experimentation is an essential component in research and investigations, whether it may be engineering, agriculture, medicine, or any. An experiment can be described as a test or series of tests where significant modifications are made to a system's input variables so that the system's output performance can be observed and the reasons for changing responses can be analyzed. In particular, experiments are conducted to investigate the performance of processes or a system of processes which can be followed by a simple model as shown in Figure 2.10. The variables which are predominant for the study have both controllable and uncontrollable parameters. The main motive of experimentation is to examine the effect of the process parameter on various responses.

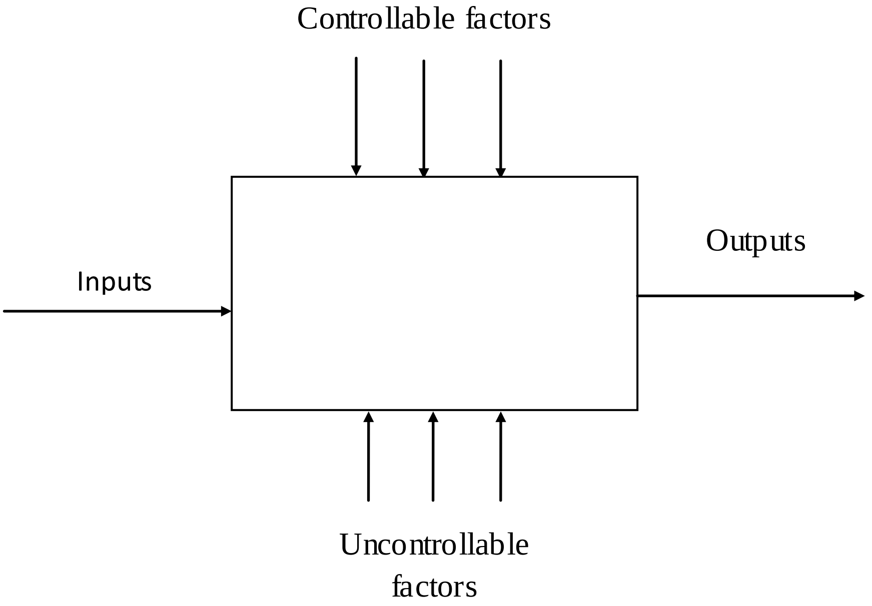

Figure 2.10 A General experimental processes

Response Surface Methodology (RSM) is a set of mathematical and statistical approaches that may be used to model and analyze issues in which a response of interest is impacted by multiple factors and the goal is to maximize or minimize the response. The fitted surface is used in the response surface analysis. As a result, the goal of RSM can be met by

- Generation and evolution of topography of the response surface (local maximum, local minimum)
- Determining the optimum region of global maxima or global minima

The RSM plays a vital role in the development, formulation, and analysis of new scientific research and products. It's also effective in improving current studies and products.

Industrial, biological, and clinical science, social science, food science, and physical and engineering sciences are the most prevalent RSM uses. In 1951, G.E.P. Box and K.B. Wilson established the RSM technique. To estimate the response variable, Box and Wilson recommended a first-degree polynomial model. They noted that this model is not an exact representation of the process, but it is simple to estimate even when nothing is known about it

(Wikipedia 2006). The orthogonal design was inspired by Box and Wilson (1951) in the case of the first-order model. Many scientists and engineers are concerned with the central composite designs (CCDs) and three-level designs of Box and Behnken for second-order models (1960)[31].

When compared to traditional experimental approaches that employ a one variable at a time strategy, RSM offers numerous benefits. RSM provides a huge amount of data from a limited number of tests. Traditional approaches are time-consuming, and a large number of tests are required to describe a system's behaviour. The interaction effect of the independent factors on the response may be observed in RSM. In addition, to learn more about the process, the empirical model that relates the response to the independent variables is employed in light of this, we may conclude that RSM is an effective technique for optimizing real-time engineering applications [32]. Because the higher-order effects are generally negligible, response surfaces are frequently approximated using a second-order regression model. Eq 2.1 is a second-order regression model (sometimes known as the full quadratic) for k number of components. The central composite design, CCD, Box-Behnken Design, as well as the most common approach, will be illustrated in the following sections.

$$y = \beta_0 + \beta_1 x_1 + \ldots. + \beta_k x_k + \cdots \beta_{11}^2 x_1^2 + \cdots \beta_{kk}^2 x_k^2 + \cdots \beta_{12} x_1 x_2 + \cdots \beta_{k-1,k} x_{k-1} x_k \qquad (2.1)$$

The Central Composite Design, or CCD, is the most often used approach of response surface design. As shown in Figure 2.11, the CCD is a two-level full factorial or fractional factorial design with additional center points and axial points. While the center point is placed in the middle of each level of a factor, the axial points are placed in the middle of each level of the other factors. As a result, the axial point coordinators are (-1, 0), (1, 0), (0, -1), and (0, 1). (0, 1). The lack of fit may also be investigated with the inclusion of center points. The distance from the center and the axial points are denoted by α.

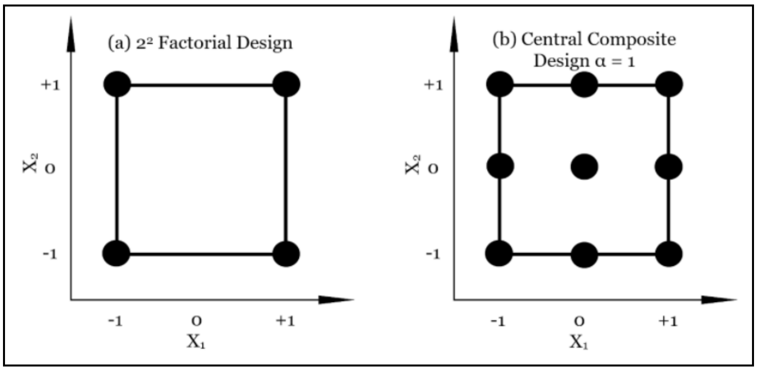

Figure 2.11 Central Composite Design, CCD (right) from the 22 Factorial Design (left) [33]

The axial points can be created in a more efficient way to get even more data from the same number of experiments. For instance, the CCD in Figure 2.12 provides more information on the response surface over CCD in Figure 2.11. The CCD in Figure 2.12 has five separate levels for each element, allowing for the use of a higher-order model, such as the cubic model if the quadratic model fails to match.

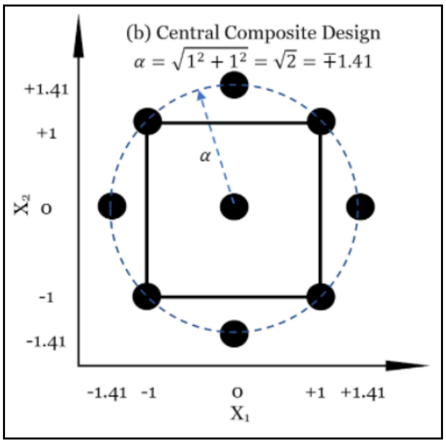

Figure 2.12 Central Composite Design, CCD from the Base 22 Factorial Design with Alpha Value 1.41 for Rotatability [33]

The systematic arrangement of the axial points along the perimeter of the circle formed for the factorial design using the corner points has certain extra benefits, including the factorial design's rotatability function. The capacity to provide consistent and stable variance throughout the whole range of the independent/predictor variables defines a successful prediction model.

2.5. Effect of process parameters and heat input on deposition characteristics

To repair or remanufacture the damaged parts, single bead depositions are more prominent, and single bead deposition studies are helpful to understand the mechanism of multi-pass multi-track depositions which in turn are used as additive manufactured objects. There is a necessity to find the optimal process parameters for automation and high productivity. The optimal settings can simplify the process characteristics and are cost effective also. Hence it is necessary to investigate the effect of process parameters on bead characteristics for a single pass cladding process. In the literature work, a review has been done on the effect of process parameters and heat input on the bead characteristics are presented.

The geometry of each bead is affected by the size of the filler wire and the wire and torch speeds for multiple bead deposition, the step over increment between subsequent beads also plays a role. [34]. Javid et al. [35] investigated single cladded layer deposition of Tungsten on Inconel 718 using a laser cladding process. Response surface methodology (RSM) is used to optimize the deposition characteristics. The findings indicated that laser power is the most important element impacting dilution and clad width, whereas scanning velocity has a significant impact on porosity and fractures. Van Thao et al investigated thin-walled 308L stainless steel components in the cold metal transfer process. The effect of process parameters on single weld bead geometry was investigated[36]. Javid et al. [35] investigated single cladded layer deposition of Tungsten on Inconel 718 using a laser cladding process. Response surface methodology (RSM) is used to optimize the deposition characteristics. The findings indicated that laser power is the most important element impacting dilution and clad width, whereas scanning velocity has a significant impact on porosity and fractures. Kindermann et al studied the process stability of Inconel 718 in cold metal transfer (CMT). CMT made IN718 has a higher melt pool size and poorer as-deposited hardness than powder-based additive manufacturing, but it has been shown to have a good aging response and a similar Laves phase area percentage [37].

Abioye [38] made single tracks on Inconel 625 with a wire-laser-assisted fabrication method. The authors varied process parameters namely wire dripping, smooth wire transfer, and wire stubbing at different cladding conditions. The geometrical characteristics of the track such as aspect ratio and contact angle were studied to determine the dilution ratio (%) of the tracks. The key parameters that had a predominant effect on the track geometrical characteristics were found to be wire deposition volume per unit length and energy per unit length of the track. Aspect ratio and dilution ratio positively impacted energy per unit length of track whereas the contact angle showed a negative impact. However, material deposition volume per unit length of track improved directly with contact angle and inversely with aspect ratio and dilution ratio. It is also observed that the aspect ratio and dilution have positive dependency while the contact angle has a negative dependency on energy per unit length. Guo et.al [39] deposited clad beads of Inconel 625 on the surface of AISI 4130 plates using hot wire pulsed TIG welding. A two-layer multiple-track weld overlay was deposited. The authors noticed columnar dendrites, and few planar crystals, and cellular dendrites near the fusion zone. Also, equiaxed grains and steering dendrites were found in the upper portion of the weld overlay. Cong et. al [40] studied the effect of heat input on bead geometry and porosity in the weld beads with different CMT arc modes and observed that the CMT-PADV arc mode has better bead characteristics and samples are free from porosity. Shen et. al [41] investigated the effect of heat input on weld bead geometry of steel joins in the submerged arc welding process and found that with an increasing heat input, the bead characteristics like bead width reinforcement, and HAZ size increased. Benyounis et.al [42] studied the effect of heat input on the bead characteristics of laser butt welding of medium carbon steel and developed correlations for bead geometry concerning the heat input. The fusion area, ferritic volume fraction, and austenitic grain size have been increased with an increase in heat input for AISI 316L steel joints made by the gas metal arc welding process. Also, 0.5 and 1.5 kJ/mm heat input conditions have lower ferrite content in the heat-affected zone and melting zone [43]. Resende et.al [44] studied the influence of weld parameters on bead characteristics. Weglowski et. al [45] investigated the effect of current on metal transfer behaviour in the gas metal arc welding process and found that welding current has a significant impact on metal transfer rate. Karadeniz et. al [46] conducted experiments on the robotic MIG welding machine to investigate the effect of the welding process on penetration and observed that with an increase in weld current, the penetration also increased. Zong et.al [47] have studied the arc, droplet, and weld pool behaviour of the TIG- MIG hybrid welding process. Qianru [48] investigated the influence of the deposition angle in the tungsten arc welding process and found that the uniform deposition was made at an angle of 60° to the substrate. Wei Wu et al [49] compared the microstructure of deposits made on 316L by the arc and cold welding processes. G. P. Rajeev et al [50] have investigated the deposition of Stellite on H13 steel by CMT process considering the dynamic and arc length correction factors. However, investigations on the bead geometry of Austenitic stainless steel, mainly SS 304 fabricated by Cold metal transfer based WAAM are rarely reported, especially for CMT-AM technology. Lee et al [51] studied the effects of process parameters on bead geometry in gas metal arc (GMA) welding. A central composite based RSM design was used to estimate the correlation between the welding parameters and bead characteristics. It was observed that welding current and torch positions have a significant effect on bead geometry. Pavan Kumar et al [52] used a neural network backpropagation technique to forecast bead characteristics in the cold metal transfer welding process. Typically, it is observed that high welding speeds or low heat inputs normally produced poor fusion. The model used welding current, welding speed, and heat input as input parameters and predicted bead characteristics as output parameters. It was found that the training data has good agreement with the experimental data. Sravanthi et al [53] performed a lap welding joint between Al alloy and mild steel by Cold Metal Transfer technique using Al- 12% Si filler wire with a weld speed range of 0.5–1 m.min−1. The lap joint was tested against mechanical strength and corrosion strength. A small fraction of intermetallics were observed at higher weld speeds which resulted in reduced corrosion. Sivasakthivel et al [54] used a model based on a neural network to estimate the bead geometry of preheated stainless steel plates in the gas metal arc welding process.

The welding arc behavior in the cold metal transfer process was studied by Shukla [55]. A ten-layer wall was deposited on a base plate. During the boost phase of the CMT cycle, when the majority of the base plate and electrode melts, the welding arc had a high intensity. The welding arc intensity steadily rises from the first to the fifth layer for a given process parameter but stayed relatively constant from the fifth to the tenth layer. The bead width steadily grew from the first to the fourth layer, and then stayed relatively constant from the fifth to the tenth layer. In recent years, the welding community has eagerly embraced the developing technology of wire arc additive manufacturing (WAAM) to produce various classes of structural materials. Thermal management is critical in wire arc additive manufacturing (WAAM) to avoid heat buildup and deal with constraints such as deposition cycle, geometry, and mechanical properties, and anisotropies. CMT Advanced stands out as a popular choice for reducing the amount of heat transmitted to the layers being deposited while maintaining the same deposition rate. Niles and Jackson [56] studied the effect of arc distribution, process parameters in the GTAW process and observed that the melting and thermal efficiencies increased with weld speed. The authors have compared the amount of energy that goes into the base metal and the amount of energy spent on melting the fusion zone. Modenesi [57] developed numerical models to predict the temperature distributions and melting rate of feed wire in the gas metal arc welding process. The efficiency of the model was improved by adding constants related to the melting rate and welding current. The authors correlated the results with the arc characteristics. Liu et. al [58] used a triple wire arc method to increase melting efficiency. A mirror-symmetrical wire arrangement was adopted with the main wire in the center and two symmetrical wires on both the left and right sides of the main wire. The wire polarity of the main wire and the side wires acted as anode and cathode and the arcs developed between these wires superimposed and improved the penetration, the melting area, and the melting efficiency of the base metal. Suban et.al [59] demonstrated the effect of shielding gas and weld current on melting rate and found that the shielding medium has a negligible influence on the melting rate and is depends on the welding current only. Li et al studied the end lateral extension path strategies while deposition of single beads. Response surface method is used to conduct the experiments considering the process parameters weld current, travel speed, path offset distance. The results significantly improved the quality of the deposition bead [60].

2.6. Microstructure, mechanical, wear, and corrosion properties of WAAMed components

The microstructure of any manufacturing component depends on the type of solidification process. In the direct metal deposition process, the material directly falls on a substrate or a target surface and solidifies immediately due to rapid cooling. The grain shape and size are greatly influenced by the cooling rate. The mechanical properties are influenced by the microstructure formations, chemical compounds evolved while processing, post heat treatment conditions, etc. Hence, in this section, a brief review of the microstructure and mechanical properties of the AM processed samples has been presented.

Shuai studied the microstructural changes in selective laser melting (SLM) processed samples and observed elongated, columnar grains as fabricated samples while rectangular and equiaxed grains after heat treatment[61]. Huebner et al have studied the microstructure formations in Inconel 625 - WC metal matrix composite in laser cladding process with a weight percentage of 20 and 30 of WC. The authors observed precipitates of spherical oxide in both samples[62]. Leary et al. fabricated Inconel 625 lattice structures of 2 mm, 3mm, and 4 mm sizes at 2%, 4%, 6% strain rates using the Selective Laser Melting (SLM) process. It was observed that FCC with a 2 mm cell configuration has better specific strength and modulus than the other configuration lattice structures [63]. Marchese et al investigated the laser powder bed fusion processed (LPBF) Inconel 625 for microstructure and mechanical characterization. The samples had very fine dendritic structures with γ'' phases aged at 700 °C for 24 h[64]. Pleass used the SLM process to investigate the effect of powder particle sizes and flowability on process capability and observed that powder particles smaller than 10-µm diameter were responsible for the formation of agglomerations and make the process difficult[65]. Koutiri studied the porosity and fatigue behavior of Inconel 625 deposited by a selective laser melting process[66]. Gonzalez compared the microstructure of Inconel 625 processed through binder jetting process, laser powder bed fusion, and electron beam processes. Columnar grains are formed in EPBF and equiaxed grains are formed in binder jetting and LPBF. [67]. Hu used selective laser melting (SLM) to study the mechanical and microstructural behavior of laser welded Inconel 625 specimens. The tensile strength of the welded joint was found to be higher than the base material. The welded region consists of columnar grains whereas as-received SLM samples have equiaxed grains[68]. Dinda used a direct metal deposition method to fabricate Inconel 625 samples containing columnar dendrites. The columnar dendrites were found to follow the direction of the laser scan while deposition[69]. Abioye deposited Inconel 625 single track beads using a wire-based laser deposition process. The individual effects of process parameters on bead characteristics were investigated. A high quality surface was obtained at a low contact angle (<80°), and 5% and 13% of dilution ratio[38]. Abioye studied laser cladded Inconel 625 coating to study the corrosion performance and found that the corrosion resistance of laser cladded Inconel is very close to that of the wrought Inconel 625 alloy. The authors observed columnar dendrites at the clad-substrate interface[70]. Marchese investigated heat treated Inconel 625 alloy samples in the laser powder bed fusion process. The anisotropy in the material was eliminated by the heat treatment. Equiaxed grains were formed at heat treatment conditions of 1080˚C and 1150˚C [71]. Zhong compared the solidification behavior of Inconel 718 and Inconel 625 and observed that the Inconel 625 has faster cooling rates than Inconel 718 due to stronger convection in the melt pool[72]. Rivera et al investigate the grain refinement and densification of Inconel 625 processed by the additive friction stir process. The EBSD results showed that fine grains of size 0.27 µm are formed at the interface regions [73]. Wang used the gas tungsten arc welding process to manufacture the Inconel 625 structure as an additive product and observed the microstructure at different locations of the deposited structure. Cellular grains were observed near the substrate, and columnar dendrites to equiaxed grains were observed while moving to the top region[74]. Sandeep et al. conducted experiments in the shielded metal arc welding process (SMAW) to study the fatigue and wear behaviour of Inconel 625 clad beads at 80 Amperes and 105 Amperes of welding currents. It was observed that the fatigue performance is higher for high weld current clads than the specimens with lower weld current processed samples[75]. Fesharaki compared laser cladding and TIG cladding process on microstructure of Ni-based Inconel 625 coatings. The microstructure observed at the coating surface was coaxial, columnar, and cellular dendrites, and with laser coating, a finer microstructure was formed [76]. Feng et al studied the microstructure of laser cladded Inconel 625 coating in shielded metal arc welding (SMAW) process and found that the coatings had a finer microstructure as compared with arc welded samples[77]. Rajani investigated the microstructure of Inconel 625 in explosive forming by varying the process parameters and found that at low impact energies linear interfacial structures are formed whereas at high impact energies wavy interfaces are formed[78]. Yangfan investigated the microstructure of Inconel 625 deposited by the CMT process. Microstructural examinations revealed that cellular grains are formed near to the substrate, columnar dendrite at the middle portion of the structure, and dendrites with secondary arms at the top portion of the deposit[79]. Wang et al [80] successfully fabricated NiTi alloys in the cold metal transfer process. From the bottom to the top portion of the depositions, the anisotropic Ni_4Ti_3 microstructure is observed, and due to the formation of Ni_3Ti, the tensile strength and hardness improved. Yangfan et al [79]fabricated Inconel625 alloys using Cold Metal Transfer (CMT). The average microhardness of the produced specimens improved marginally from 248 HV to 253 HV. The yield strength (YS) improved from 376 MPa to 400 MPa, while the ultimate tensile strength (UTS) increased from 647 MPa to 687 MPa. Xu et al [81] compared the microstructure of Inconel 718 deposited with laser-powder-based AM and WAAM. When compared to the tiny grains of laser powder bed fusion and wrought Inconel 718, the as deposited WAAM Inconel718 had big columnar grains and many laves phase. It is observed that laser powder deposition and wrought alloy have fine grains and WAAM deposited samples have large columnar grains. Gao et al. used the CMT process to manufacture 9Cr Ferritic/martensitic nuclear grade steel. Untempered martensite with columnar and equiaxed grains dominated the microstructure and also microstructure anisotropy was observed at different locations of the deposited wall[82]. Li et al. demonstrated the fabrication of 91-grade steel in the wire arc additive manufacturing process. CALPHAD is used to study the thermodynamic characteristics of the depositions. With an ultra-fine and high-density dislocation embedded martensite lath and amounts of -ferrite, the as-built P91 steel manufactured by WAAM has significantly greater strength than typical wrought material. After homogenization at 1200°C for 2 hours, the heterogeneous structure created by the WAAM process is eliminated. The WAAM P91 steel has outstanding mechanical characteristics, with an ultimate tensile strength of 774 MPa, yield strength of 686 MPa, and ductility of 19.4 percent, thanks to optimized homogenization (1200°C for 2 hours) and aging (760°C for 2 hours) heat treatments [83]. Rodrigues et al introduced SiC particles while preparing high strength alloys in the WAAM process. Fe3C precipitates and grain refinement occurs due to the high melting point of SiC particles. The refined grain structure and finely scattered Fe3C were found to increase the mechanical strength of the SiC-added components, which was described in the refinement of grain structure. [84]. Seow et al investigated Inconel 718 microstructure processed in WAAM. In addition, the WAAM process promotes columnar grain growth and the formation of a strong fiber texture, resulting in grain structural anisotropy. Using specific Post-deposition homogenization heat treatments, this undesirable microstructure may be corrected. The improved heat treatment significantly reduced grain structure anisotropy, resulting in nearly isotropic high-temperature tensile characteristics[85]. Xu et al attempted to develop large scale metallic components in the wire arc additive manufacturing process. The as-deposited samples exhibit low strength than the aged samples. Through the production of substantial quantities of finely dispersed precipitates, the samples aged for 3 hours considerably decreased microstructural heterogeneity and enhanced mechanical characteristics by 24.7 percent [86].

2.7. Literature on dissimilar material deposition

Sasahara et al. studied the dissimilar deposition of stainless steel and Ni alloy on a wire arc deposition welding station. As a consequence, the mechanical characteristics of the produced alloy were found to be equivalent to those of the bulk material. Also, recommended that the arc deposition process can be used to produce highly functional shapes made of different materials [87]. Nam et al. developed stainless steel and Fe functionally graded material using the direct energy deposition (DED) process. The authors observed that the prepared FGMs have pores at the interfaces[88].

Shen et al investigated the wire-arc additive manufacturing (WAAM) process to produce a functionally graded iron-aluminum with a composition ranging from 0% to 50%. The results of the experiments demonstrate that the WAAM technique used to produce iron aluminide functionally graded material with full density, appropriate composition, and adequate mechanical characteristics[89]. Unel et al investigated dissimilar joining of aluminum and steel using a robotic controlled cold metal transfer (CMT) welding process. The study explores the microstructure-strength connection while accounting for the heat input-intermetallic compound (IMC) layer formed between aluminum and steel after establishing the optimal process parameters based on the peak load for mechanically sound welds. Fe2Al5 and FeAl3 phases were observed in the microstructure investigations[90]. Tian et al studied dissimilar material deposition of Al alloy on Ti alloy using a cold metal transfer based wire arc deposition process. The interface layer between the Ti and Al alloys was observed to have a continuous layer and a discontinuous layer. The modulus of elasticity and hardness between Al and Ti alloys were studied. The fracture is observed in the interfacial layer [91]. Wang et al. studied the influence of arc current on the microstructure, phase formation, microhardness transition, and dry-wear characteristics of NiTi and Ti6Al4V using the wire arc additive manufacturing (WAAM). Crack-free and dense coatings were produced and NiTi2 phase with fine α Ti dendrites. This work demonstrates that the use of in-situ dual wire arc additive manufacturing of surface coatings for better wear resistance[92]. Zhu et al. investigate the laser cladding process factors that influence the microstructure growth of single pass and multi-pass cladding layers of Invar alloys. The top layer is made up of equiaxed crystals, whereas the bottom is made up of columnar crystals. The hardness of the cladding layer gradually decreases from top to bottom[93]. Yan et al. investigate the laser-wire deposition of 316 L stainless steel. Process optimization has been done to deposit multi-layer single-pass and single-layer multi-pass depositions. The deposited samples have epitaxial column growth also ferrite formations in the grain boundaries in their microstructure. Also, it is observed that the successive layers have cellular and columnar grains. The laser depositing products have plastic and ductile behaviour [94]. Sawant et al studied the deposition characteristics of single-track and multi-track deposition of Stellite 6 using the micro-plasma transferred arc powder deposition process. The most significant parameter that impacts energy and deposition material usage was found to be micro-plasma power. The dendritic microstructure of single-track deposition is finer than that of multi-track deposition[95]. Deshmukh et al investigate the multitrack deposition CO-Cr alloy using the Plasma Tungsten Arc Welding process. Process parameters were optimized to attain the minimum distortion and minimum surface residual stresses. Also, observed that there is a strong metallurgical bonding between the multi-tracks with no defects on the surface [96].

2.8. Chapter Summary

In this chapter, a comprehensive introduction on the development of metal based additive manufacturing, and the evolution of wire arc additive manufacturing systems especially with a special focus on the Gas Metal Arc Welding (GMAW) process have been discussed. And the current status of research on Inconel based superalloys and related fabrication methods, mechanical and metallurgical characterization techniques. After literature review, the below are observed

- Additive manufacturing methods are effective in manufacturing customized and complex geometries which can not be produced in conventional manufacturing and machining process
- WAAM processed components relatively produces direct functional parts at a lower cost than power fed additive manufacturing process
- There are no size limitations in the WAAM process hence medium and large sized functional parts can be fabricated
- Most of the current Additive manufacturing machines are based on lasers as primary energy sources. There is limited literature available on arc based deposition methods
- Very little literature has reported on the cold metal transfer process as arc based additive manufacturing methods
- There is a necessity to investigate the effect of process parameters and process conditions on WAAM deposited components. Even though parameters effects are reported in the literature, an in depth study on bead characteristics are to be evaluated
- The effect of heat input on bead geometry, mechanical properties, and microstructure formations are rarely reported
- Also, multi decision models are required to obtain better additive manufacturing components that satisfy both bead characteristics as well as mechanical properties

In summary, this research subject aims to apply CMT based WAAM process to develop Inconel based superalloys. At the same time, a dissimilar deposition of Inconel on stainless steel has to be fabricated with the same process conditions. From the literature review, the following objectives are framed for the present research work.

- Feasibility study on CMT process and to optimize the process parameters for additive manufacturing process
- Investigate the effect of heat input and cooling rate on deposition characteristics and melting phenomena
- Multi decision analysis of bead characteristics fabricated in wire arc deposition process for additive manufacturing using Grey relational analysis (GRA)
- Investigate the effect of heat input on microstructure and mechanical properties of CMT deposition
- Mechanical, wear, and corrosion study of multi pass multi-track deposition Wire arc additive manufacturing

Chapter 3

Experimental Methods and Characterization Techniques

3.1 Introduction

This chapter discusses the experimental setup and equipment used in the present research work. The details of the equipment along with the specifications used for the preparation, microstructural characterization, and estimation of mechanical properties are presented. The chapter explains the experimental setup for the fabrication of wire arc additive manufacturing (WAAM) samples with a cold metal transfer (CMT) process. The details about various devices, equipment, and methodologies used to evaluate various deposition characteristics are also supplied. The process parameters are selected based on the previous literature and trial experiments were conducted to identify the ranges and levels to conduct the experimentation. The experiments were well planned and conducted to observe the deposition characteristics such as bead height, width, penetration, dilution, hardness, etc. The central composite design based response surface experimental was used, and the Grey Relation Analysis (GRA) was performed to identify the optimum combination of process parameter levels.

3.2 Experimental Setup

Experiments were conducted on Fronius made manual CMT machine attached with a 3 axis manual controlled workstation. The deposition torch was held stationary in a vertical position through which filler wire feeding was done at a fixed angle. The table bed can be moved in three axes. Shielding gas has an equal proportion of Argon and CO_2 gas to reduce atmospheric effects. Figure 3.1 shows the pictorial representation of the CMT machine used in this study. Figure 3.2 shows the experimental setup of the CMT deposition station. It consists of a CMT controller unit, a wire feeding unit, 3 axis table, and a deposition nozzle/torch. Feedstock wire is fed through the wire feeding unit. An in-house developed 3 axis working table is used for the deposition process. The substrate plate is clamped to the table with screws to avoid distortions during bead deposition. The working table has movements in X and Y directions while the deposition is done through the nozzle which is attached to a frame that moves up and down in the z-axis as shown in Figure 3.2. The inert gas is supplied along with the feeding wire through the nozzle. Inconel 625 filler wire of 1.2 mm diameter which is commercially available in industrial markets is used for deposition.

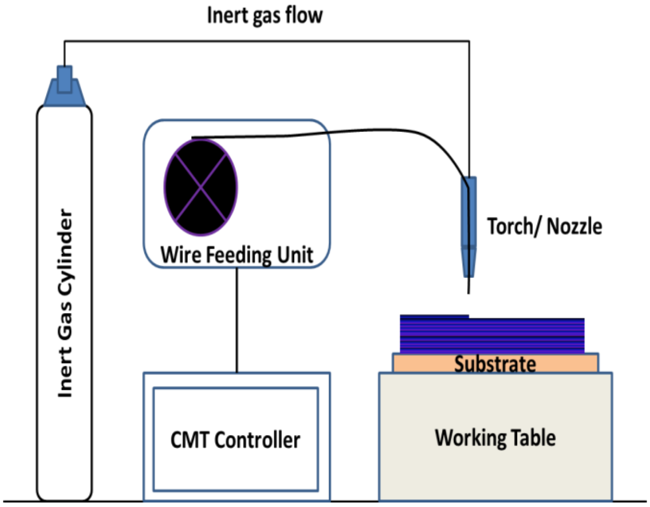

Figure 3.1 The outline diagram of the cold metal transfer process

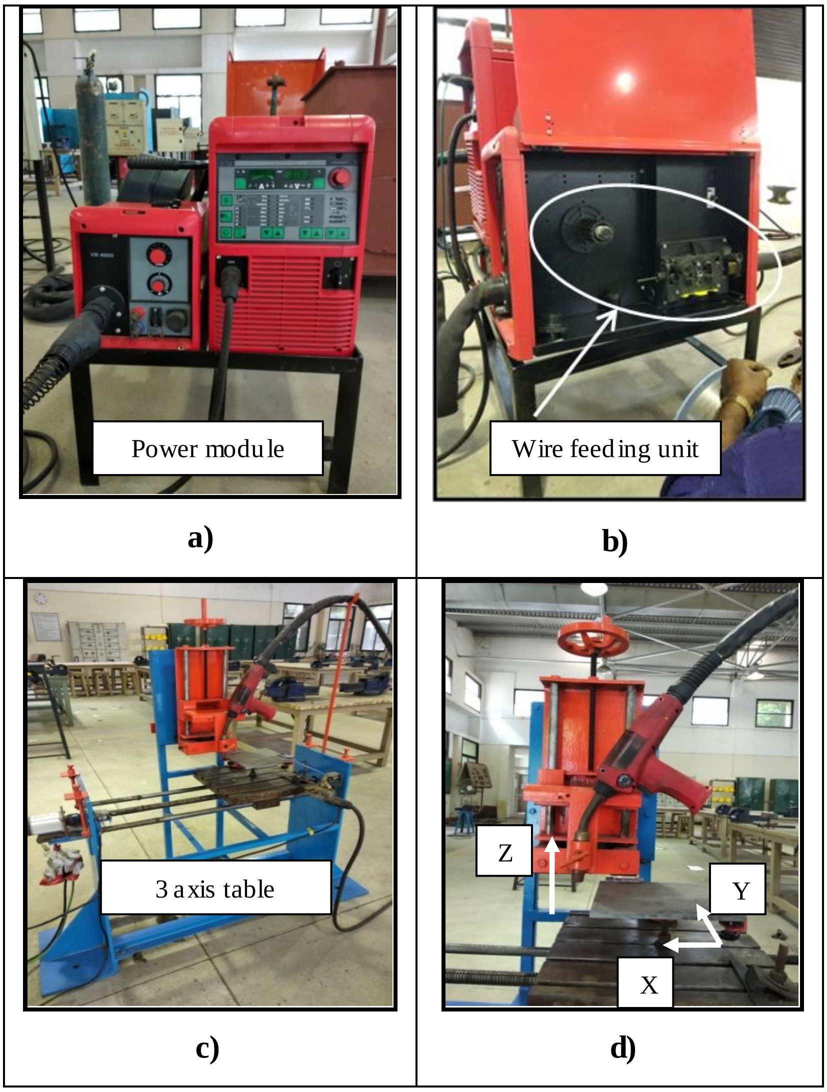

a)

b)

c)

d)

Figure 3.2 Cold metal transfer deposition setup a) Power Source Controller b) Wire feeder c) 3 axis table and d) deposition nozzle/torch

The chemical composition of the wires is shown in Table 3.1 and Table 3.2 and physical properties are mentioned in Table 3.3. A mild steel plate of size 250 x 250 x 10 mm was used as the substrate for deposition. Before cladding, mild steel plates were sandblasted over the surface and cleaned to avoid contamination.

Table 3.1 Chemical composition of Inconel 625

Elements	Ni	Cr	Mo	Nb	Fe	Al	Ti	C	Mn
Percentage	Bal.	20-23	8-10	3.15-4.15	Max 5	Max 0.4	Max 0.4	Max 0.1	Max 0.5

Table 3.2 Chemical composition of SS 304

Cr	Ni	Mn	Mo	Cu	Al	Si	P	Co	N	C	Fe
17.61	8.85	3.97	0.008	1.17	0.015	0.49	0.01	0.11	0.05	0.06	Bal.

Table 3.3 Physical properties of Inconel 625 and Stainless steel 304

Physical property	Inconel 625	Stainless steel 304
Density	8.44 g/cm^3	7.78 g/cm3
Elastic modulus	205 GPa	190 GPa
Poisson's ratio	0.308	0.27
Melting point	1350 °C	1450 °C
Thermal Conductivity	9.9 W/m-K	12 W/m-K
Co eff. Thermal expansion	1.52x10^-5 /°C	1.6x10^-5 /°C

3.3 Experimental Design

Input current (I), welding speed (S), and Standoff Distance (D) are observed to be the most affecting process parameters on bead characteristics. Parameter ranges were identified by conducting trial experiments. Based on trial experiments, the below mentioned parameters levels listed in Table 3.4 were selected for experimental design. Table 3.5 shows the experimental design condition as per the central composite experimental design for 3 parameters and 3 level response surface designs.

Table 3.4 Process parameters for experimentation

Process Parameters	**-1**	**0**	**+1**
Current (Amps)	90	100	110
Stand Off Distance (mm)	4	5	6
Weld Speed (m /min)	0.2	0.3	0.4

Table 3.5 Central composite response surface design for conducting experiments

Std.Order	Run Order	Current in A	Standoff Distance in mm	Weld Speed in m/min
5	1	90	4	0.4
9	2	100	5	0.3
10	3	100	5	0.3
1	4	90	4	0.2
12	5	100	5	0.3
11	6	100	5	0.3
2	7	110	4	0.2
8	8	110	6	0.4
3	9	90	6	0.2
7	10	90	6	0.4
6	11	110	4	0.4
4	12	110	6	0.2
13	13	83.67	5	0.3
14	14	116.33	5	0.3
18	15	100	5	0.46
15	16	100	3.36	0.3
19	17	100	5	0.3
20	18	100	5	0.3
16	19	100	6.63	0.3
17	20	100	5	0.14

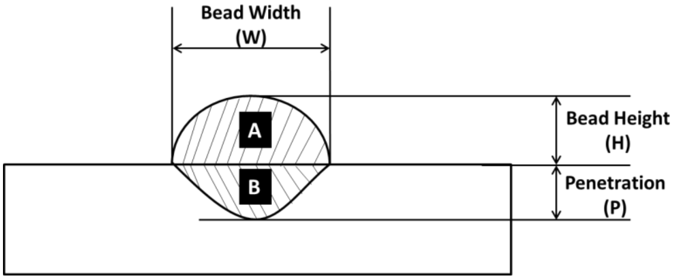

Figure 3.3 Bead geometry measurements

Figure 3.3 shows the bead geometry and corresponding measurements to be observed from the bead. The weld bead profiles were examined by using a 3D optical microscope and the bead dimensions viz., bead width (W), bead height (H), Penetration (P) were measured using open software ImageJ. The percentage of dilution was calculated by using

$$\% \text{ Dilution} = (B/(A+B)) * 100 \qquad (3.1)$$

Where A- Area of reinforced added metal
B- Area of penetration into the substrate

3.3.1. Development of mathematical models

The response function representing any of the weld bead dimensions can be expressed as

$$Y = f(I, S, D) \qquad (3.2)$$

Where Y is the response, e.g. penetration, dilution, etc.
I the welding current (A), S the welding speed (m/min) and
D is standoff distance (mm).

The second-order polynomial (regression) equation used to represent the response surface for K factors is given by,

$$Y = b_0 + \sum_{i=k}^{k} b_i X_i + \sum_{\substack{i,j=1 \\ i+j}}^{k} b_{ij} X_i X_j + \sum_{i=1}^{k} b_{ii} X_i^2 \qquad (3.3)$$

Where b0 is the free term of the regression equation,
the coefficients $b_1, b_2, \ldots, b_k$ the linear terms,
the coefficients $b_{11}, b_{22}, \ldots, b_{kk}$ the quadratic terms and
the coefficients $b_{12}, b_{13}, \ldots, b_{k-1k}$ are the interaction terms

For three factors, the selected polynomial could be expressed as given below:

$$Y = b_0 + b_1 I + b_2 S + b_3 N + b_{12} IS + b_{13} ID + b_{23} SD + b_{11} I^2 + b_{22} S^2 + b_{33} D^2 \qquad (3.4)$$

The values of the coefficients of the above polynomial were calculated with the help of statistical software, Minitab17.

3.3.2. Sample Preparation

The fabrication process is carefully controlled and deposited on the substrate such that deposited beads have good geometry without pores, blowholes, and other processing defects. After deposition, the samples were extracted from the middle portion of the deposition tracks using a wire electric discharge machine (EDM). The wire EDM specification is specified in Table *3.6*. The grain formation and related characteristics are observed from the fusion region perpendicular to the deposition direction. The machined samples were polished with 800 to 2000 grit size emery papers and later polished with velvet cloth and aluminum oxide slurry to attain a mirror finish for microstructure examinations.

Table 3.6 Specification of wire electric discharge machine (Electron Eco cut)

Parameter	***Specification***
Max. table Size	*370 X 600 mm*
Max. workpiece height	*200 mm*
Max weight	*300 kg*
Main travUse X, Y)	*250, 350 mm*
Auxiliary table traverse (u,v)	*30, 30 mm*
Max. cutting angle	*±5°/100 mm*
Max. wire spool capacity	*6 Kg*
Dry run speed	*80 mm/min*
wire diameter	*0.25 mm*
Display	*Colour LCD*
minimum input command	*0.001 mm*
Interpolation function	*Linear and Circular*
Simultaneously controlled axes	*X, Y, u,v*
Min. resolution	*0.001 mm*
Data / Output	*USB 2.0, Keyboard, RS232C Isolated serial interface*
Input power supply	*3 phase, AC 415V, 50Hz*
Average power supply	*1.3 to 2.3 kVA*
Dielectric fluid	*Deionized water*
Tank capacity	*140 Liter*
Paper filter	*10μ Single cartridge*

3.4. Characterization Techniques

3.4.1. Microstructural characterization

3.4.1.1. Scanning electron microscope

The microstructures of the composite surfaces are observed using scanning electron microscopy (SEM), as shown in Figure 3.4. SEM is a type of electron microscope that produces images of a sample by scanning it with a focused beam of electrons. The electrons interact with atoms in the sample, producing various signals that contain information about the sample's surface topography and composition. SEM is a completely computer-controlled unit with a conventional tungsten-heated cathode intended for high and low vacuum operations. It is sophisticated, user-friendly software for controlling the microscope and capturing the image using windows platform has superior optical properties, offers good clarity of flicker-free digital image, processing, and measurements, has images stored in standard formats, provides an automatic arrangement of the electron microscope and several other automated processes and these among the specific features of the equipment. The technical specifications of SEM are given in Table 3.7.

Figure 3.4 Photograph of Scanning electron microscope

Table 3.7 The technical specifications of SEM.

Make/Model	*Tescan, VEGA 3 LMU*
Electron Gun	*Tungsten heated cathode*
Resolution	*3nm at 30kv / 2nm at 30 kb*
Magnification	*2x – 1,000,000x*
Maximum field of view	*24mm at WD30 mm*
Accelerating Voltage	*200V to 30kV*
Probe current	*1pA to 2μA*
Scanning Speed	*From 2ns to 10ms per pixel adjustable continuously*
Chamber suspension	*Pneumatic*
Specimen Stage	*Compucentric, fully motorized*

3.4.1.2. Energy Dispersive Spectroscopy (EDS)

Figure 3.5 EDS coupled with SEM

Energy dispersive spectroscopy (EDS) is an analytical technique that is used for the chemical composition or elemental analysis of a material. EDS has also known as Energy Dispersive X-ray Analysis (EDXA). It is an analytical technique used for the elemental analysis or chemical characterization of a sample. It relies on the interaction of some source of X-ray excitation and a sample. Its characterization capabilities are due in large part to the fundamental principle that each element has a unique atomic structure allowing a unique set of peaks on its electromagnetic emission spectrum. The confirmation about the elemental composition of a specimen can be overlaid on top of the magnified image of the specimen by using a process known as X-ray mapping. An EDS coupled with SEM, as shown in Figure 3.5 was used in the present study.

3.4.1.3. Three-Dimensional Optical Microscope

The 3-dimensional surface profile of the Electro-Discharge machined surfaces was generated using an optical microscope in Figure 3.6, Model: HUVITZ LUSIS HC-30MU. The complete specifications are listed in Table 3.8. The Z-axis autofocus helps the simple acquisition of 2-D images with samples of varying focal depths of the machined surface. The advantages of Z-axis features are topographic analysis and 3D Profiling through Panasis software, which generates a composition of all the 2D images into 3D profiles.

Table 3.8 The Specifications 3-D optical microscope.

Z-axis module Specifications	
Stroke Distance	*30mm*
Resolution	*0.01µm*
Repeatability	*0.5µm*
Maximum Speed	*1.4mm/sec*
Weight	*5kg*
Dimensions	*Width:240mm; Depth: 157mm; Height: 202.5mm*
Load capacity	*15kg*
Microscope Specifications	
Eyepiece	*10x Wide Field, Diopter Adjustable*
Observation Tube	*Trinocular Erect*
Mountable Objective Lens	*Plan Fluor EPI 5X, 10X, 20X, 50X and 100X*
Accuracy and repeatability	*Accuracy of magnification ±15 - ±20µm, repeatability of magnification±10 - ±15µm*
Lamp Halogen	*12V, 100W halogen lamp*
Camera	*Image sensor, 3 megapixel*
Illumination	*Reflected bright field/dark field/ polarized*
Filter	*Neutral Density Filter, Differential Interference contrast filter*
Focusing Unit	*Stroke 30-45 mm, Resolution 0.01 – 0.05µm, maximum sample height 15-25mm*
3D Imaging and measurement	*Panasis professional*

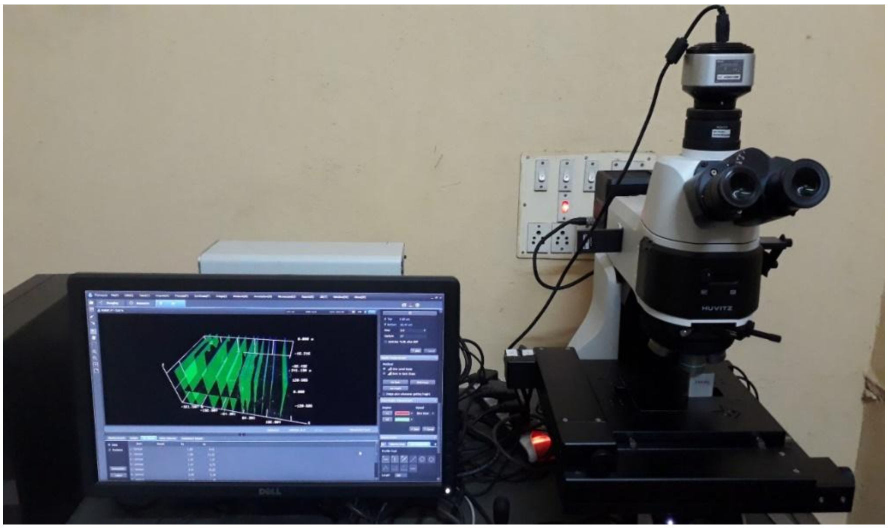

Figure 3.6 Optical type 3-D microscope

3.4.1.4. Optical Microscope

The microstructures of the composite surfaces are observed using an optical microscope, as shown in Figure 3.7 (Make: QASMO optical microscope DIC polarizer, Model: QX4RT). The optical microscope produces images of a sample due to color contrast by scanning it with a focused beam of light.

Figure 3.7 Optical Microscope

3.4.2. Mechanical, wear, and corrosion tests

3.4.2.1. Compression test

A compression test is one of the major types of mechanical tests to find the strength of the materials for many engineering applications. In materials, the strength of importance may be measured in terms of either stress required to obtain appreciable plastic deformation or the material can withstand the maximum stress. These measures of strength are used with appropriate caution in engineering design. The various materials and processes can be compared by measuring the compression properties of the newly developed materials and processes.

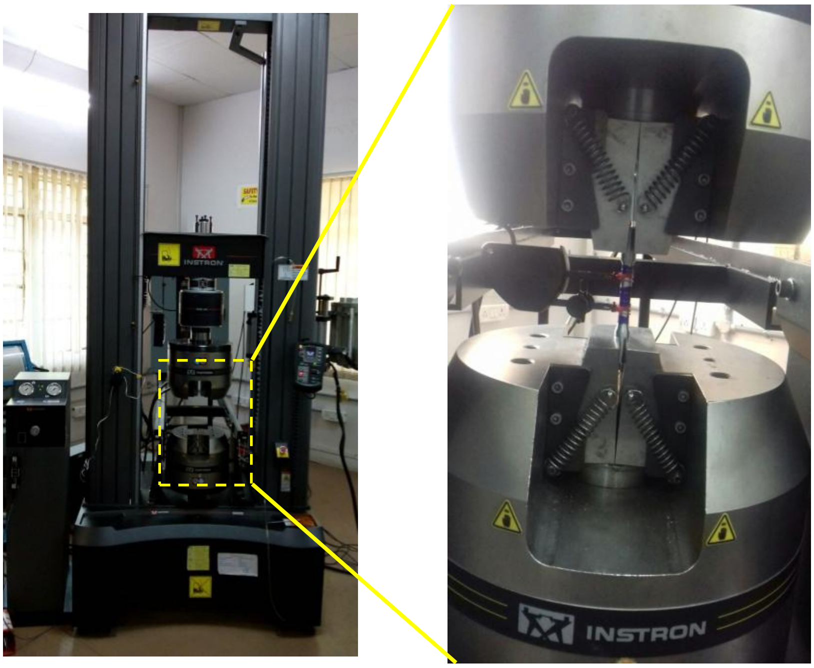

Figure 3.8 Universal Testing Machine (UTM)

The properties are frequently used to predict the performance of a material under forms of loading other than uniaxial tension. A tensile test was carried out on the electromechanical tensile test machine. The test data were used to determine the ultimate tensile strength, yield strength, and percentage elongation of the materials. The mechanical properties are evaluated by conducting the uniaxial tensile and compression test on the Universal testing Machining (UTM), which is shown in Figure 3.8. The specifications are presented in Table 3.9.

Table 3.9 The specifications and features of UTM

Make/Model	*INSTRON 5985*
Capacity	*250kN*
Vertical test space	*1430mm*
Load measurement accuracy	*+/- 0.5% of reading down to 1/1000 of load cell capacity*
Data acquisition rate	*2.5kHz*
Speed range	*0.00005 to 1016mm/min*

3.4.2.2. Hardness Test

The term hardness refers to the ability of a material to resist permanent deformation. The larger the resistance to deformation, the harder the body appears. There are four common methods available to measure the hardness of any material such as Brinell, Knoop, Rockwell, and Vicker's hardness tests. Vickers hardness testing method is simple as compared to others and is suited well for all metals. In this method, an indenter of a straight diamond pyramid with an angle between opposite faces of 136°, is applied under a specific load onto the surface of the material to be tested for a set time interval. According to the law of proportional resistance, the indentation surface is proportional to the force applied. For microhardness studies, usually, the range of load is taken to be 5g to 1000g and the dwell time is considered in the range 10 to 15sec. Shimadzu HMV Vicker’s microhardness tester with a diamond indenter having an angle of 136° between opposite faces was used to measure microhardness, which is shown in Figure 3.9. Since the indentation depth and area cover during Vicker’s micro hardness test are limited to few micrometers, the position of the indenter on the specimen has a great influence on the hardness number value particularly in the case of multi-phase inhomogeneous composite materials. Therefore, the Brinell hardness test, according to ASTM E10, is also conducted on all fabricated specimens. The deepest and the widest indentations in this method compared to other hardness testing methods will more accurately account for the hardness of the bulk portion. The photograph of the Brinell hardness test machine is shown in Figure 3.9.

Figure 3.9 Vicker’s microhardness tester

3.4.2.3. Wear test

The wear test of Inconel 625 and dissimilar deposition of stainless steel and Inconel 625 was carried out using a pin-on-disc wear testing machine (Ducom Bangalore, Model: TR-20). The pin-on-disc wear testing setup is shown in Figure 3.10. In this test, the specimens were ground up to 1500 grit SiC abrasive paper to ensure complete contact with the counter body. Before the test, polished specimens were cleaned thoroughly with ethanol. The cylindrical samples (10 mm × 15 mm) were prepared for the wear tests. The samples having a contact area of 78.5 mm^2 were maintained for each sample. The abrasion wear test parameters were listed in Table 3.10. The average of three test values was considered to calculate weight loss and wear coefficient. An accurate analytical weighing balance of 0.0001 g resolution was used to measure the initial and final weights of samples.

Table 3.10 Summary of abrasive wear test conditions

Parameter	**Value**
Applies force (N)	20,30,40
Counter-body	EN31
Pin diameter (mm)	10
Sliding velocity (m/s)	0.25
Sliding distance (m)	500
Track diameter (mm)	70
Time (mins)	20
Temperature (^{o} C)	Room temperature
Test environment	Air

.

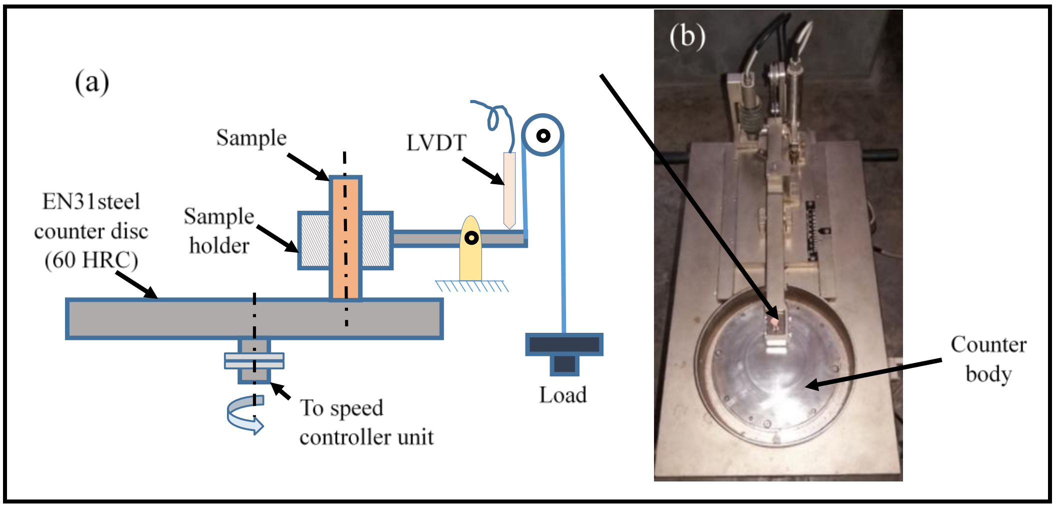

Figure 3.10 Pin-on-disc wear test setup (a) Schematic representation and (b) Photograph of sliding wear tester.

The pin-on-disk wear test was conducted according to the ASTM G99 standard in dry sliding conditions under a maximum load of 40 N and a sliding velocity of 0.25 m/s. In the current study, wear tests of Inconel 625 specimens were conducted at a sliding velocity of 0.25 m/s. The wear test samples were prepared with the dimensions of Ø10 × 15 mm. The EN 31 Grade steel disc (C: 0.90-1.20%, Si: 0.10-0.35%, Mn: 0.30-0.75%, Cr: 1.00-1.60%, S: 0.05%, and P: 0.05%) with the hardness of 60 HRC (~ VHN: 7.2 GPa) was used as a counter body for the wear test.

The wear volume loss was calculated by measuring the weight loss and density of samples. The specific wear rate (w) is calculated using Eq. (3.5); whereas, Archard wear equation, (Eq. 3.6) was used to determine the wear coefficient (t).

$$Sp.\,wear\,rate, w = \frac{(W_{initial} - W_{final})}{\rho \times \ell \times d} \tag{3.5}$$

$$Wear\,coefficient = w \times H \tag{3.6}$$

Where, W $_{initial}$: weight of the sample before the wear test, W$_{final}$: weight of the sample after the wear test, ρ: experimental/measured density of the sample, d: sliding distance, and H: hardness. At least two tests were done under similar wear test conditions and the average values were reported.

3.4.2.4. Corrosion measurement

Polishing of working electrodes (Inconel 625, C$_{15}$Al) was done using emery papers up to 2000 grit size and the samples were thoroughly washed with distilled water. After polishing, a three-electrode cell glass assembly with Inconel 625 as a working electrode with an exposed area of 0.7854 cm^2, Ag/AgCl /1M KCl electrode as a reference electrode, and platinum spiral electrode as a counter electrode was used for corrosion tests. All electrochemical experiments were conducted in a stagnant, naturally aerated neutral 3.5 mass per volume (m/v) % NaCl solution (pH: ~ 8.2) at room temperature. The electrochemical impedance spectroscopic (EIS) studies and polarization experiments were performed using PARSTAT 4000 Potentiostat/Galvanostat (see Figure 3.11).

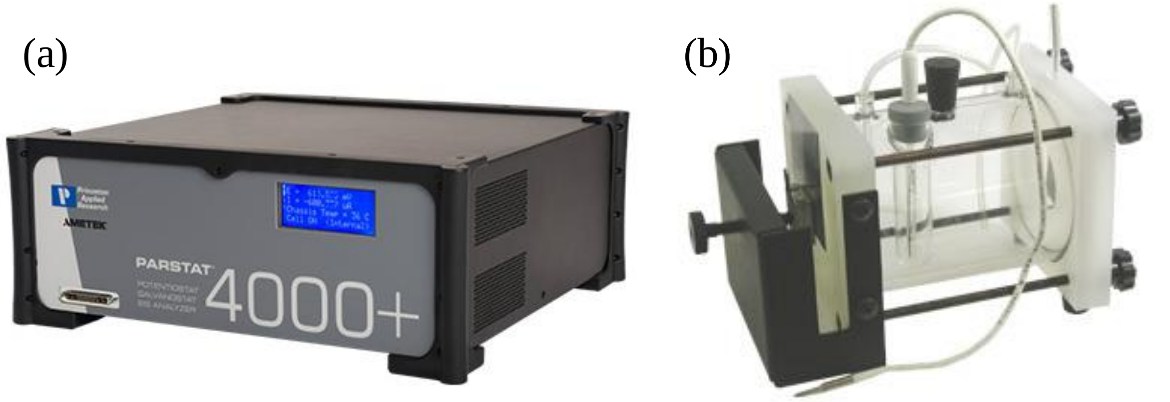

Figure 3.11 The photograph of the corrosion test setup. (a) Corrosion work station and (b) corrosion test cell.

The electro-potentials were measured against the standard potential of the saturated calomel electrode and standard hydrogen electrode at 0.245 V. The polarization studies were carried out at a scan rate of 1 mVs−1 and the impedance (Z) measurements were taken in the frequency range from 0.1 Hz to 60 kHz. The superimposed AC signal amplitude was set to 20 mV with a peak to the peak measuring system. All electrochemical experiments were conducted at least two times for repeatability. After electrochemical studies, the surface morphology of the Inconel 625 and dissimilar deposition samples were investigated using SEM-EDS to understand the corrosion behaviour.

3.5. Chapter summary

In this chapter, an overview of cold metal transfer based on the wire arc additive manufacturing process, experimental design, sample preparations, characterization methods, and related equipment has been discussed with relevant illustrations and specifications.

Chapter 4

Feasibility Study and Parameters Optimization of Single Bead Deposition of Stainless Steel and Inconel

In the present chapter, the feasibility of the cold metal transfer process to make additive manufacturing components are investigated. The effect of process parameters on single bead deposition of stainless steel and Inconel are studied thoroughly. Commercially available filler wires are used for the deposition process. Central composite is used for experimentation and ANOVA was used to estimate the effects of current, weld speed, standoff distance on bead characteristics. Regression models were developed to relate process parameters and bead deposition characteristics.

4.1 Introduction

Austenitic stainless steels are extensively used in nuclear applications such as reactor coolant pipes, valve bodies, spacer column assembly, control rod drive mechanism, and vessel internals due to their very good corrosion resistance and superior mechanical properties [29], [97]. The 304 grade (maximum 0.08 percent C) is most commonly used in the 300 ASS series due to its superior low-temperature toughness in addition to corrosion resistance [98]. Sensitization (grain boundary depletion of chromium and precipitation of chromium carbide near or at the grain boundaries) of the weld clads is one of the potential problems in the welding of ASSs. Sensitization leads to degradation of corrosion resistance as well as the mechanical properties [99].

Nickel-based superalloy Inconel 625 has retained superior properties even at elevated temperatures up to 1500˚C with high strength, resistance to corrosion, fatigue strength, and thermal fatigue resistance. Apart from high chromium content, Inconel 625 is embedded with other alloying elements like Molybdenum (Mo), Niobium (Nb), Iron (Fe), etc. which contributes to the solid solution strengthening. These superior qualities offer a choice for diverse applications in engineering structures. Hence, these Ni-based alloys are used in aerospace, marine, petrochemical, nuclear reactors, etc.[100]. Even though many production methods are available for manufacturing Inconel 625 based components, high production rates and complex structures have limited their commercial applications. Additive manufacturing (AM) would be an alternating feasible production method for superalloys [74].

There are extensive studies conducted on the processing, optimization, and microstructural developments of materials processed in additive manufacturing and allied technologies, but the cladding process and the conditions are different for each case [101]–[105]. Zumelzu et al showed that the highest mechanical characteristics can be achieved by using a shielded metal arc welding (SMAW) method using the E316L16 electrode under low thermal input circumstances and 5 percent ferrite in the welded region [101]. Laser and laser tungsten inert gas (TIG) hybrid welding has been reported to be useful compared to standard TIG welding procedures as they generate lower dendrite sizes and also do not substantially deteriorate the mechanical characteristics of 304 ASS [8]. Lu et al. systematically researched the impact of argon and oxygen in helium base protected gas tungsten arc welding on arc ignitability, bead protection, and weld penetration 304 SS [11]. Rahul et al observed that the protected metal arc welding method does not result in important carbide precipitation or intermetallic stages even at the lowest heat input. The ferrite content and grain size improved with enhanced heat input. This research demonstrates that electron backscattered diffraction is essential to quantitatively change the grain size in the area impacted by fusion/heat as it can consider twin borders as part of the grain in the calculation of grain size [106]. Qianru [48] investigated the influence of the deposition angle in the tungsten arc welding process and found that the uniform deposition was made at an angle of 60° to the substrate. Wei Wu et al[49] compared the microstructure of deposits made on 316L by the arc and cold welding processes. G. P. Rajeev et al [50] have investigated the deposition of Stellite on H13 steel by CMT process considering the dynamic and arc length correction factors. However, investigations on the bead geometry of Austenitic stainless steel, mainly SS 304 fabricated by Cold metal transfer based WAAM are rarely reported, especially for CMT-AM technology. Lee et al[51] studied the effects of process parameters on bead geometry in gas metal arc (GMA) welding. A central composite based RSM design was used to estimate the correlation between the welding parameters and bead characteristics. It was observed that welding current and torch positions have a significant effect on bead geometry. Pavan Kumar et al [52] used a neural network backpropagation technique to forecast bead characteristics in the cold metal transfer welding process. Typically, it is observed that high welding speeds or low heat inputs normally produced poor fusion. The model used welding current, welding speed, and heat input as input parameters and predicted bead characteristics as output parameters. It was found that the training data has good agreement with the experimental data. Sravanthi et al [53] performed a lap welding joint between Al alloy and mild steel by Cold Metal Transfer technique using Al- 12% Si filler wire with a weld speed range of 0.5–1 m.min−1. The lap joint was tested against mechanical strength and corrosion strength. A small fraction of intermetallics were observed at higher weld speeds which resulted in reduced corrosion. Sivasakthivel et al[54] used a model based on a neural network to estimate the bead geometry of preheated stainless steel plates in the gas metal arc welding process. The model predicted the bead characteristics within a 4% error. Also, an empirical regression equation was developed for bead geometry to optimize the process parameters.

4.1.1. Scope of work

Single-pass beads are most useful for remanufacturing and repairing purposes. The quality of cladding for additive manufacturing predominantly depends on bead geometry. Hence, it is required to have an optimum range of bead parameters to ensure the desired mechanical properties.

In the present work, austenitic stainless steel 304 and Inconel 625 were used for experimental study. Many input factors contribute directly or indirectly to material performance characteristics in the WAAM process. These include input power, weld travel speed, wire feed, standoff distance, inert gas flow rate, path planning, deposition strategies, *etc.* The present study more emphasize on to study the feasibility of single bead deposition to use additive manufacturing process by optimizing the process parameters. In later chapters, the optimized conditions are used to fabricate multi-pass multi-track deposition which in turn can be called additive manufacturing structures.

4.2. Materials and methods

Experiments were conducted on Fronius made manual CMT machine attached with a 3 axis manual controlled workstation. The deposition torch was held stationary in a vertical position through which filler wire feeding was done at a fixed angle. The table bed can be moved in three axes. As a shielding gas, an equal proportion of Argon and CO_2 were used. For deposition, commercially available Stainless Steel 304 and Inconel 625 filler wires with a diameter of 1.2 mm were used. A mild steel plate of size 250 x 250 x 10 mm was used as the substrate for deposition.

Input current (I), Standoff Distance (D), and welding speed (S) are observed to be the most prominent parameters on bead characteristics. Parameter ranges were identified by conducting trial experiments. Based on trial experiments, the levels of the parameters chosen as current 90 to 110 Amperes, standoff distance 4 to 6 mm, and weld speed of 3 to 5 m/min as mentioned in Table 3.4. Since stainless steel and Inconel have the same melting temperature range, the experimental process parameters are the same for both materials. Based on the levels of parameters, a circumscribed central composite design with 20 experiments is selected to predict the quadratic behaviour of the responses. The central composite design is shown in Table 3.5

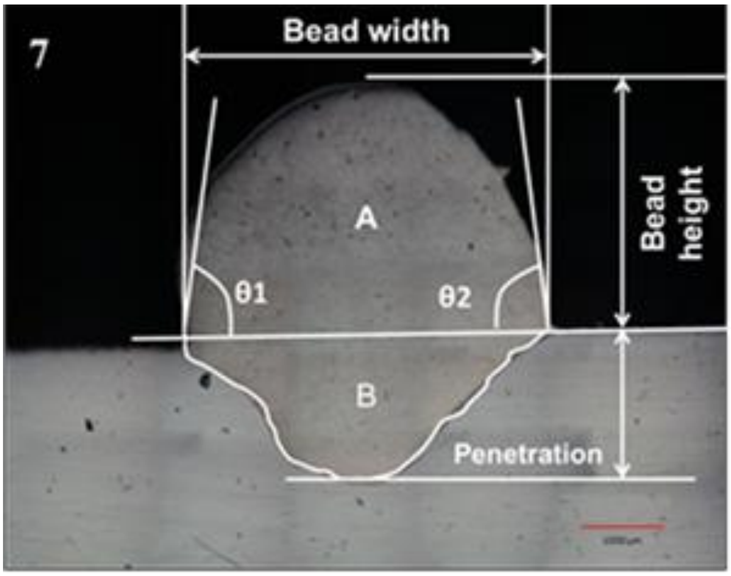

Figure 4.1Cross-section of Inconel 625 sample and measurements

Figure 4.1 shows the bead geometry and the corresponding measurements to be observed from the bead. The deposited bead structure was examined by using a 3D optical microscope and the bead geometry was measured using open source software ImageJ. The dilution was obtained by using eq 4.1

$$\%Dilution = \frac{B}{A+B} * 100 \tag{4.1}$$

Where A- Reinforced area of and

B- Penetration area

The response function in terms of process variables can be expressed [107] by Eq 4.2, 4.3 and Eq 4.4

$$Y = f\,(\text{Current, Standoff Distance, Weld speed}) \tag{4.2}$$

The general polynomial equation for regression analysis of Y response with K factors can be written as [108]

$$Y = b_0 + \sum_{i=k}^{k} b_i X_i + \sum_{\substack{i,j=1 \\ i+j}}^{k} b_{ij} X_i X_j + \sum_{i=1}^{k} b_{ii} X_i^2 \tag{4.3}$$

For the three process parameters chosen in this study, the polynomial regression equation can be written as

$$Y = b_0 + b_1 I + b_2 S + b_3 N + b_{12} IS + b_{13} ID + b_{23} SD + b_{11} I^2 + b_{22} S^2 + b_{33} D^2 \tag{4.4}$$

4.3. Results and discussion

Inconel 625 and Stainless steel 304 were successfully deposited on a mild steel substrate plate by the cold metal transfer process. Visually no defects are observed on the bead surfaces. Defects such as lack of fusion, cracks, and porosity need to be controlled to a minimum level to achieve sound mechanical properties. Precise control of heat input and thermal history, proper shielding gas and tight gas seals, high-quality feedstock, and clean substrate surfaces are helpful to reduce defects during the stainless steel WAAM process[109]. Some of the authors reported macroscopic defects in the deposition process which are presented in Table 4.1.

Table 4.1 General defects in WAAM process

Author	**WAAM process**	**Material**	**Defects**	**Reasons**
Gordon et al.[110]	WAAM	304stainless steel	Porosity	Insufficient energy for complete melting of the layers; gas generation
Wu et al.[111]	WAAM	Metals (Steel, Al, Ti, etc.)	Porosity	Contaminants of wire and substrate, Insufficient fusion or spatter ejection
			Delamination	Incomplete melting or insufficient re-melting of the underlying solid between layers
Tian et al.[112]	GTAW	Inconel 625	Solidification cracking	Existence of liquid film at terminal solidification
Dong et al.[113]	GTAW	Intermetallic Al/Cu	Grain boundary crack	Intermetallic phase-equilibrium is freely broken

In forthcoming discussions, bead quality characteristics are discussed in depth. Figure 4.2a shows the single bead deposition tracks as per the experimental design. After deposition, 10 x 10 mm samples were extracted from the plate by using wire EDM. Figure 4.3 and Figure 4.4 show the cross-sectional profiles of the samples in the middle portion of the track. While measuring the bead geometry, it was assumed that the clad geometry is uniform throughout the track. The samples were cut at the middle portion of the track as the entrance and exit portions of the track bead were irregular and more amount of material was deposited at the entrance. Figure 4.3 shows the responses that are observed from the samples.

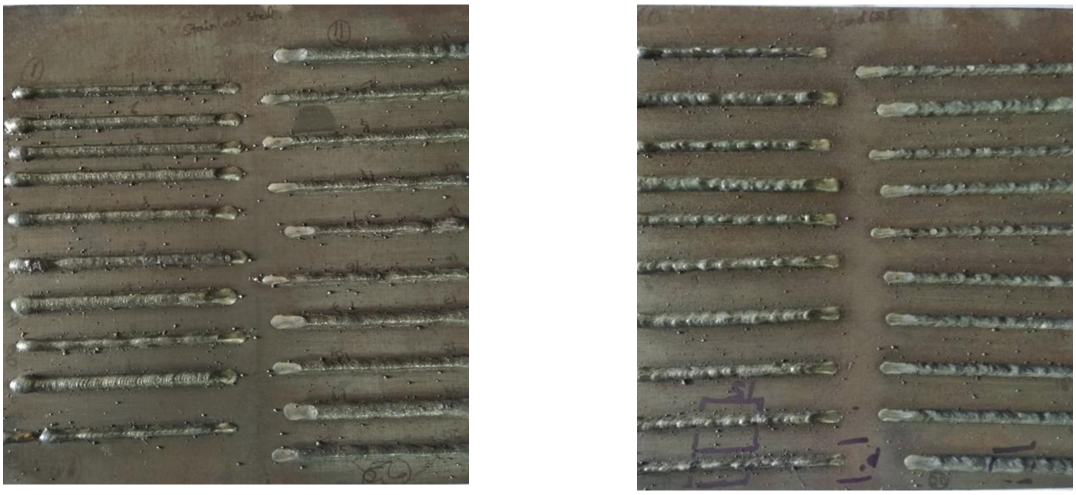

a) b)

Figure 4.2 a) SS 304 deposition clads on mild steel substrate b) Macro images of bead profiles

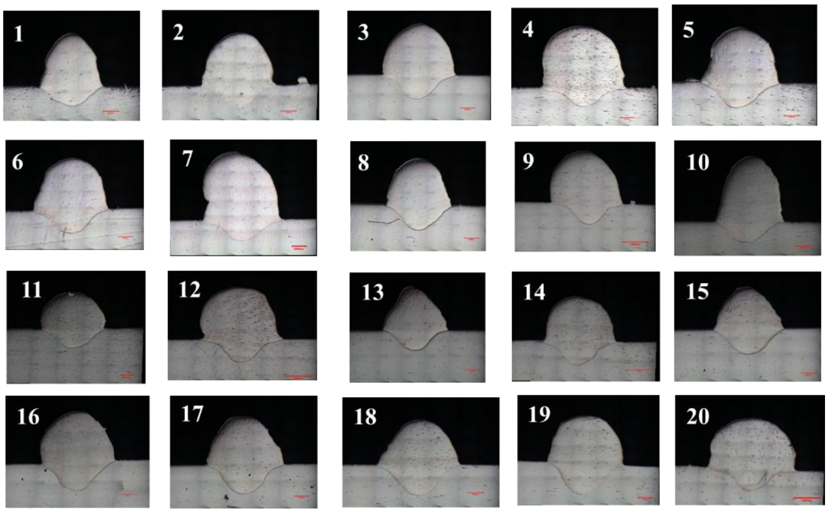

Figure 4.3 Micrographs of Inconel 625 depositions

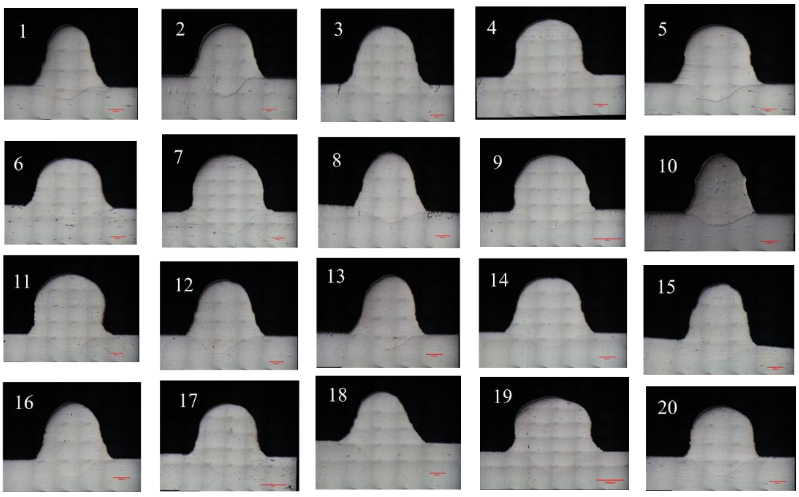

Figure 4.4 Micrographs of SS304 depositions

Table 4.2 Response table for Inconel 625 deposition characteristics

Sample No	Bead Width	Bead Height	Penetration	% of Dilution
1	3.90	3.22	1.20	22.78
2	4.73	3.73	1.79	26.08
3	5.16	3.73	1.42	21.21
4	5.64	4.07	1.25	17.80
5	5.08	3.52	1.71	25.64
6	4.83	3.53	1.52	26.49
7	4.50	3.10	0.77	19.14
8	5.16	3.12	1.74	20.54
9	4.50	3.92	0.79	22.94
10	3.21	2.85	1.13	22.45
11	4.50	3.24	0.87	30.24
12	5.91	3.87	1.65	22.76
13	4.13	3.06	1.28	28.10
14	5.21	3.02	1.71	26.75
15	4.43	2.35	1.33	34.34
16	4.64	2.95	1.67	28.67
17	4.66	2.90	1.68	30.72
18	4.90	3.16	1.84	30.03
19	4.80	3.06	1.94	30.79
20	5.88	3.42	0.86	24.68

4.3.1. Direct effects of CMT process parameters on bead characteristics

Current, standoff distance, and weld speed are the predominant parameters that affect the bead characteristics. Current corresponds to the bead penetration depth. The higher the current, the more will be the increase in bead penetration and vice versa. For weld joints, penetration should be between 30 to 40 % for better weld strength, and for additive manufacturing or cladding, it is recommended in between 10-30% [114]. Weld speed is an important process parameter that affects the continuity and homogeneity of bead geometries. Standoff distance is the distance between the delivery nozzle and the deposition surface. As the standoff distance is high, bead depth will be small and is well spread. When the standoff distance is less, bead depth would be more. However, bead quality and geometry would depend on all the process parameters simultaneously. The effect of process parameters is discussed in detail in the experimental design analysis section.

Table 4.3 Response table for stainless steel 304 deposition characteristics

Run Order	Bead Width(mm)	Bead Height(mm)	Penetration (mm)	% Dilution
1	5.15	1.98	2.30	17.63
2	5.79	3.52	1.43	19.96
3	6.12	3.38	1.16	18.65
4	6.40	3.66	1.49	16.51
5	6.07	3.59	1.17	21.64
6	5.99	3.16	1.20	21.05
7	5.63	4.10	1.00	18.72
8	5.15	3.29	0.84	21.47
9	6.41	3.93	1.35	14.47
10	3.74	2.80	0.53	17.62
11	6.30	4.42	1.20	14.18
12	4.81	2.19	1.78	21.83
13	5.44	3.15	1.02	17.74
14	5.49	3.36	0.87	18.13
15	4.81	3.24	0.96	19.53
16	4.87	3.21	1.24	26.18
17	5.99	3.38	1.18	20.22
18	5.97	3.46	1.28	15.88
19	3.63	2.05	0.82	17.93
20	5.57	3.47	1.17	18.83

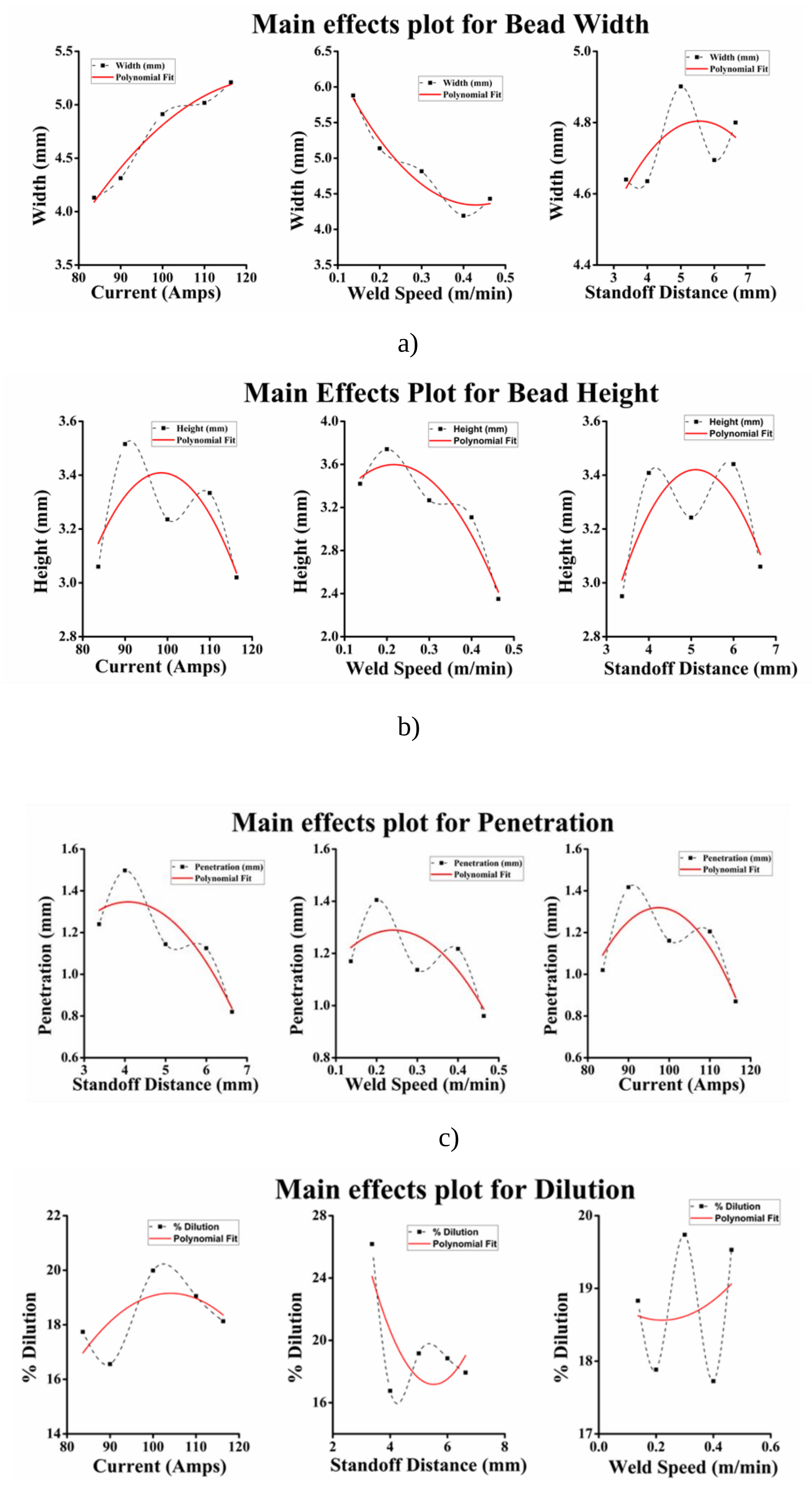

a)

b)

c)

d)

Figure 4.5 Main effect plots of Inconel 625 for a) Bead width b) Bead height c) Penetration and d) Dilution

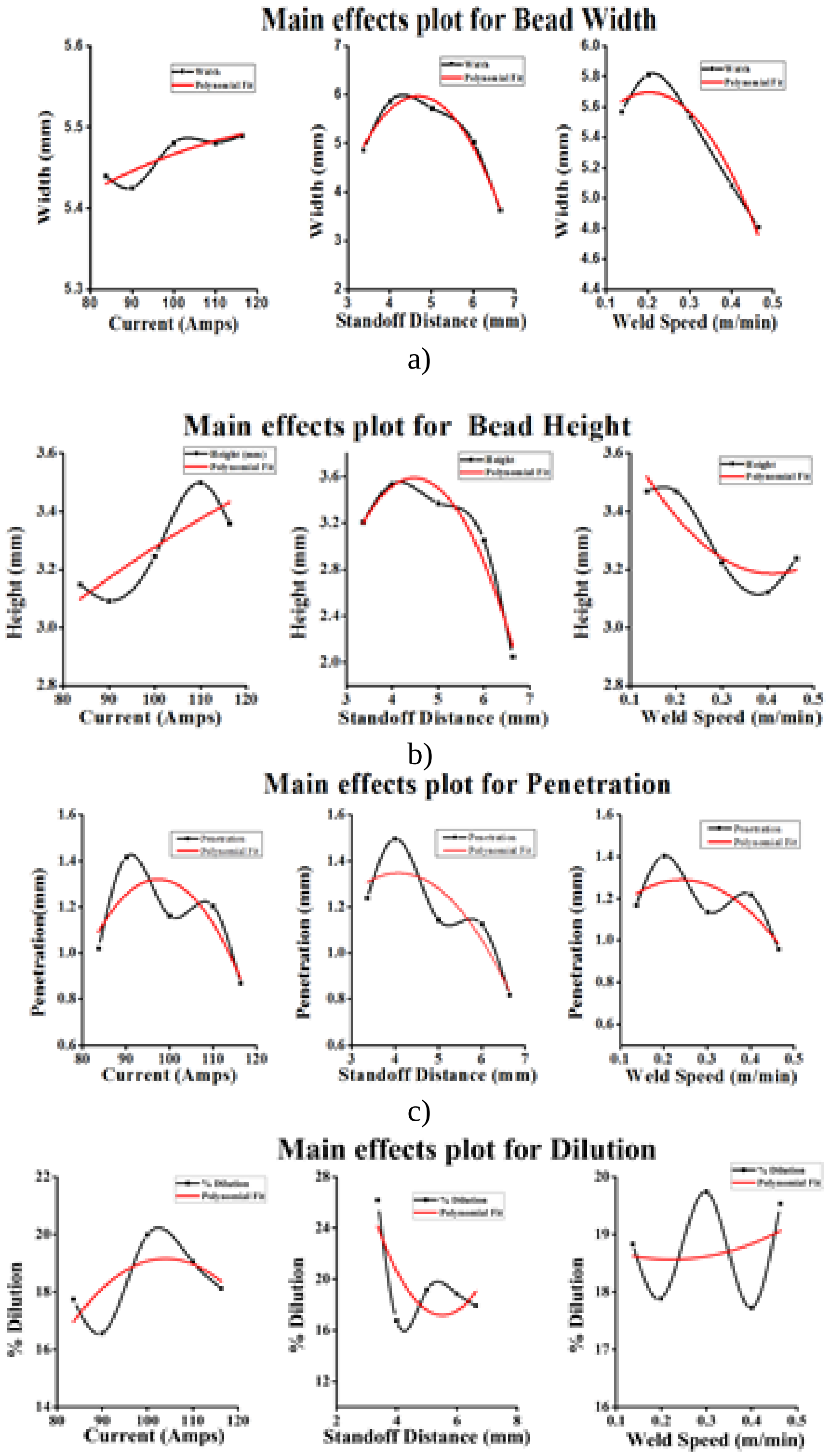

a)

b)

c)

d)

Figure 4.6 Main effect plots of SS304 for a) Bead width b) Bead height c) Penetration and d) Dilution

Figure 4.5a and Figure 4.6a show the process parameters' effect on bead width. Higher current flow enhances material deposition leading to larger molten metal flow in the lateral direction and this increases the bead width. The same trend has been reported by Palani et al [107]. The bead width increases with an increase in standoff distance at the initial stage and then it decreases. The torch/nozzle would be away from the deposited surface at a standoff distance. Hence, the arc force will be diminished and tend to spread out so that the width increases with standoff distance. When the standoff distance increases, the torch will not maintain the potential gap and deposition will not happen properly and the bead width decreases beyond a cut-off standoff distance. At higher weld speed, the time to deposit the material is less and hence results in thin and narrow beads. Similar kinds of results were reported by Balan et al [115].

The effect of process parameters on bead height is depicted in Figure 4.5b and Figure 4.6b. An increase in current yields increased weld bead convexity leading to enhanced melting rate and bead height. Hence, bead height increases with current. The bead height increases with standoff distance and then decreases beyond a cut-off standoff distance. The distance between the deposition nozzle and bead surface increases with an increase in standoff distance which leads to a thin and tiny bead in the deposition direction. The same trend has been reported by Kannan et al [116]. The bead reinforcement height was found to decreases when weld speed increases. The bead is therefore big at low weld speeds, whereas it is small at elevated speeds. The bead was wider, flatter, and smoother for low weld speeds.

From Figure 4.5c and Figure 4.6c, it is observed that initially, the penetration increases with an increase in current and then decreases. More heat input is available with an increase in current and hence the penetration increased. Further enhancement of heat input causes bead convexity and the penetration into the substrate is reduced. An increase in standoff distance results in decreased penetration depth. As the torch is moved away from the substrate plate, the deposited material will not penetrate much into the substrate plate. Hence, penetration decreases when the standoff distance increases. Palani et al [117] have reported similar observations. With an increase in welding speed the penetration decreases. The deposited bead becomes small, and it has less time to settle down at higher welding speeds. Hence, the weld pool becomes flat and thin.

The effect of current, standoff distance, and weld speed on dilution is depicted in Figure 4.5d and Figure 4.6d. It is observed that with an increase in current the dilution increases and then decreases with current beyond the cut-off limit. As the heat input increases with current, the convexity area of the bead increases, leading to greater penetration. The same trend has been reported by Balan et al [115]. With an increase in standoff distance, the dilution increases. The arc length will be more when standoff distance increases which result in a wide arc area at the weld surface. It causes a wide bead resulting in an increased reinforcement height and area. Also, the dilution of the deposited material in the weld pool is observed to decrease as the welding speed increases. At higher welding speeds, the amount of deposited metal decreases, and hence the bead reinforcement area, as well as the penetration area, is reduced.

4.3.2. Interaction effects of process parameters on bead characteristics

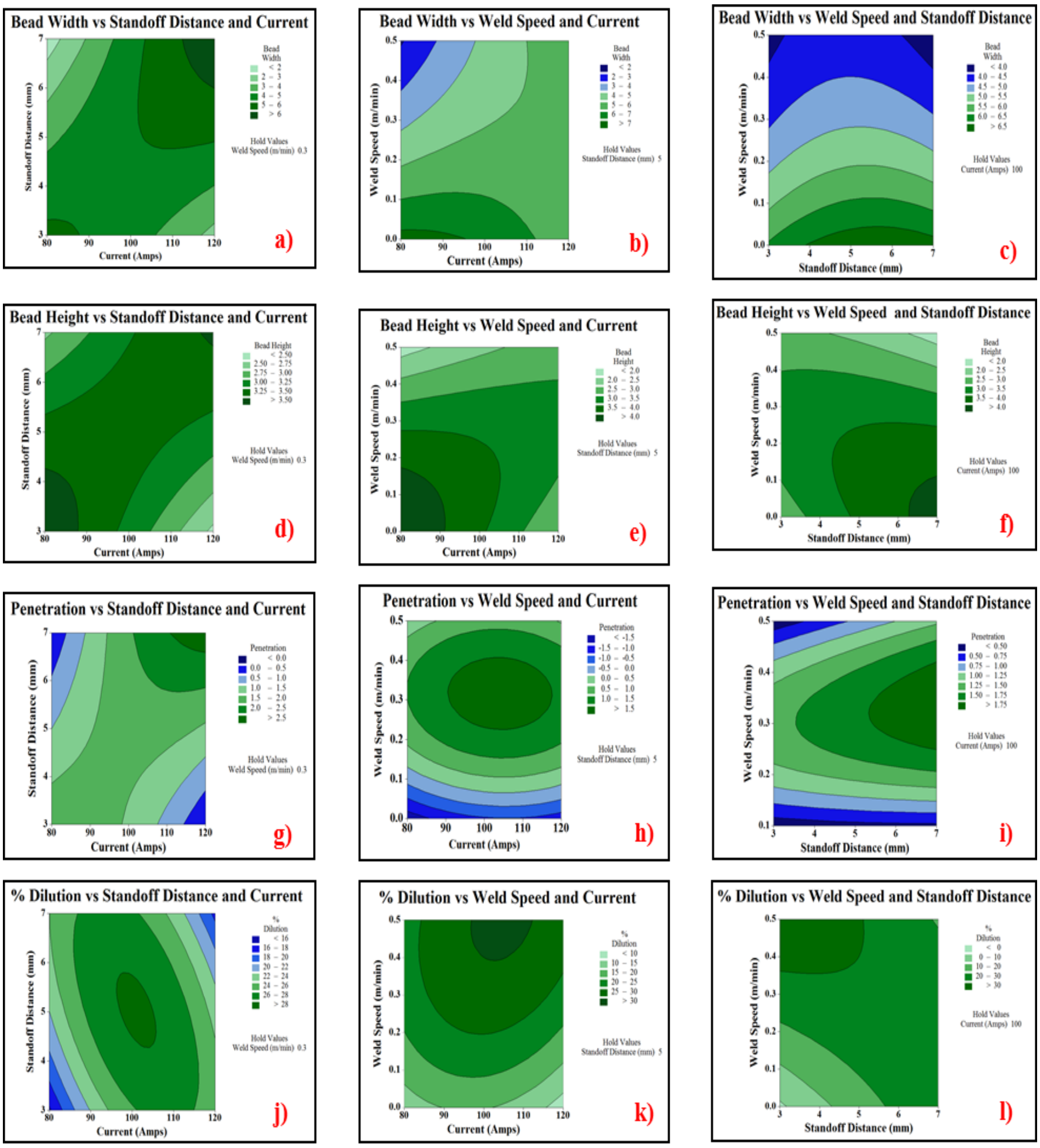

Figure 4.7 2D contour plots of Response vs. Standoff distance and Current, Weld Speed and Current, Weld speed and Standoff distance for Inconel 625 depositions

The interaction effects are considered when the performance characteristics are influenced by two or more parameters at a time. The two-dimensional interactions are depicted in Figure 4.7 and Figure 4.8. The plot its self explains the domains or feasible regions of the effect of the combined parameters on the responses. Interaction effects Figure 4.7a depicts the interaction effect of current and standoff distance at a constant weld speed of 0.3 m/min. From the contour boundaries, it is observed that the region between 4 mm to 5.5 mm of standoff distance and 80 Amps to 120 Amps of current give the maximum bead width, while the width is minimum at a higher standoff distance. Figure 4.7b shows the contour plot of weld speed and current on bead width at a 5 mm standoff distance. It is noticed that the maximum bead width is observed at low current and weld speeds whereas bead width is minimum at low weld speeds and high current as well as high weld speeds and low current regions. Figure 4.7c shows the interaction effect of weld speed and standoff distance at a constant current of 100 Amps. It is clear from the contour regions of Figure 4.7c that the maximum bead width is obtained at the central portion of the contour, i.e. mean values of standoff distance and welds speed.

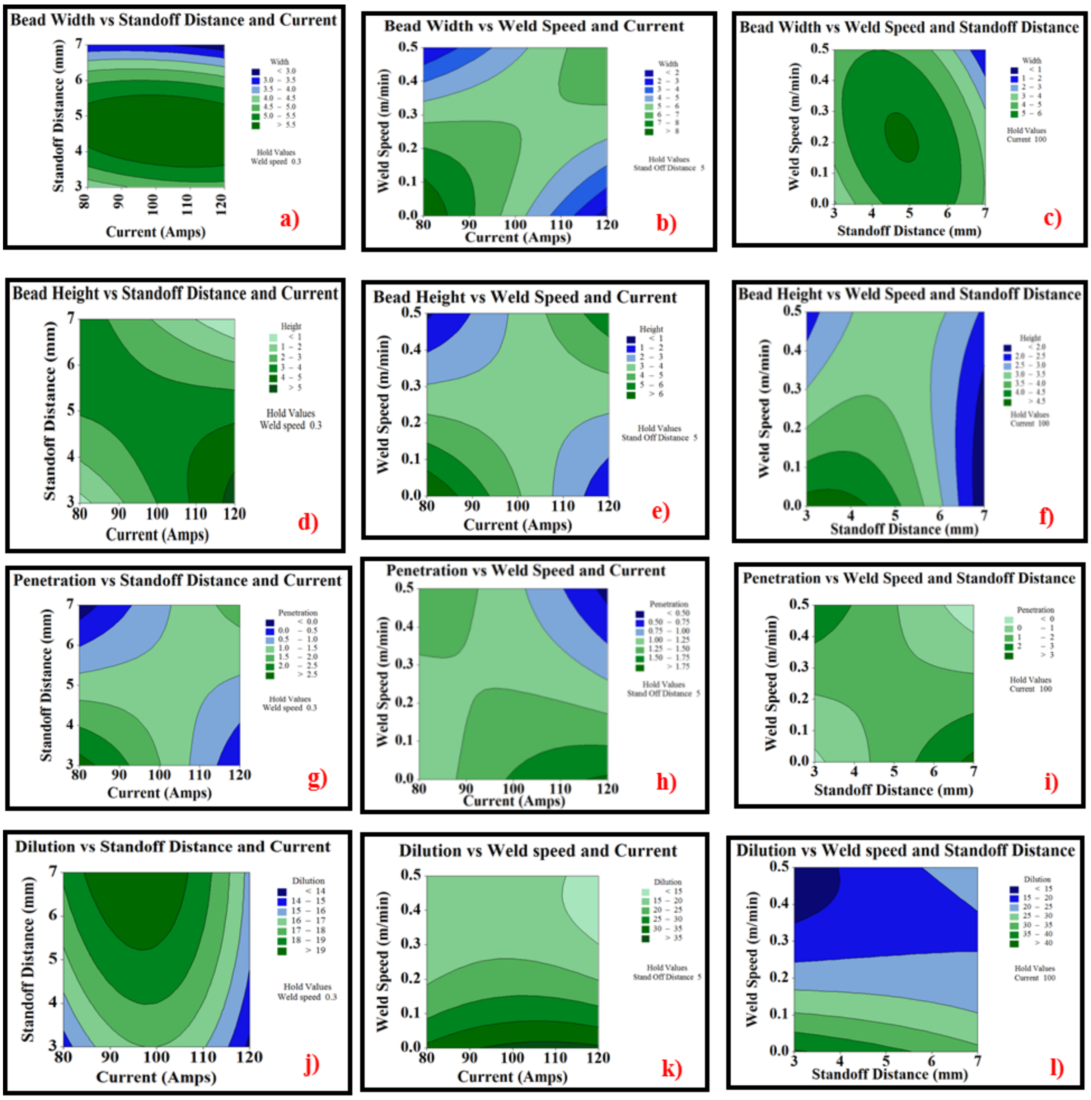

Figure 4.8 2D contour plots of Response vs. Standoff distance and Current, Weld Speed and Current, Weld speed and Standoff distance for stainless steel 304 depositions

Figure 4.7d shows the interaction effect of current and standoff distance on bead height at a constant weld speed of 0.3 m/min. The regions of low standoff distance and high current produce maximum height and vice versa. At a low standoff distance, the height of the bead will be flat and dispersed on the substrate. Figure 4.7e shows the contour plot of weld speed and current on bead height at 5 mm standoff distance. It is observed that maximum bead height is deposited at lower current and lower weld speeds and minimum bead height at high current and lower weld speeds. Figure 4.7f shows the interaction effect of weld speed and standoff distance at a constant current of 100 Amps. It is clear from the contour regions that the maximum bead height was obtained at low standoff distance and weld speed since, at lower weld speeds, the bead is stable.

The interaction effect of current and standoff distance at a constant weld speed of 0.3 m/min is shown in Figure 4.7g. From the contour area, it is evident that at lower current and lower standoff distance, the penetration is maximum, whereas penetration is minimum at higher current and higher standoff distance. Figure 4.7h shows the contour plot of weld speed and current on penetration at a 5 mm standoff distance. It is observed that the maximum penetration was obtained at high current and low weld speed whereas minimum penetration is observed at high current and high weld speeds. Figure 4.7i shows the interaction effect of weld speed and standoff distance at a constant current of 100 Amps. It is noticed from the contour regions of Fig 4i that maximum penetration is obtained at lower weld speed and higher standoff distance and vice versa for minimum penetration.

Figure 4.7j depicts the combined effect of current and standoff distance on percentage dilution at a constant weld speed of 0.3 m/min. From the contour lines, it is observed that at medium current settings and higher standoff distance, the percentage dilution is maximum whereas it is minimum at a lower standoff distance. Also, it is noted that standoff distance contributes more than current for dilution rate. Figure 4.7k depicts the contour plot of weld speed and current at a 5 mm standoff distance. The maximum penetration is obtained at low weld speed for almost all current settings. Hence, the weld speed effect is more than the current in the interaction. Figure 4.7 l shows the interaction effect of weld speed and standoff distance at a constant current of 100 Amps. From the contour regions of Figure 4.7 l, it can be observed that in the regions of low standoff distance and lower weld speeds, maximum dilution is obtained whereas minimum dilution is obtained at higher weld speeds since the bead has less time to dilute into the substrate at higher weld speeds. Similar kinds of observations are drawn for the 2D interaction effects on stainless steel bead characteristics.

Table 4.4 ANOVA analysis of Bead Width for Inconel 625 deposition

Source	DF	Adj SS	Adj MS	F-Value	P-Value
Model	10	7.408	0.741	14.810	0.035
Blocks	1	0.024	0.024	0.470	0.509
Linear	3	4.439	1.480	29.580	0.022
Current	1	1.573	1.573	31.440	0.001
Standoff Distance	1	0.019	0.019	0.370	0.556
Weld Speed	1	2.848	2.848	56.930	0.035
Square	3	0.397	0.132	2.640	0.113
Current*Current	1	0.206	0.206	4.120	0.073
Standoff Distance*Standoff Distance	1	0.147	0.147	2.930	0.121
Weld Speed*Weld Speed	1	0.041	0.041	0.820	0.390
2-Way Interaction	3	2.548	0.849	16.980	0.040
Current*Standoff Distance	1	1.893	1.893	37.850	0.045
Current*Weld Speed	1	0.643	0.643	12.850	0.006
Standoff Distance*Weld Speed	1	0.012	0.012	0.240	0.638
Error	9	0.450	0.050		
Lack-of-Fit	5	0.296	0.059	1.530	0.351
Pure Error	4	0.155	0.039		
Total	19	7.858			

Table 4.5 ANOVA analysis of Bead height for Inconel 625 deposition

Source	DF	Adj SS	Adj MS	F-Value	P-Value
Model	10	3.297	0.330	20.630	0.040
Blocks	1	1.270	1.270	79.440	0.036
Linear	3	1.491	0.497	31.090	0.045
Current	1	0.033	0.033	2.080	0.183
Standoff Distance	1	0.003	0.003	0.160	0.699
Weld Speed	1	1.455	1.455	91.020	0.043
Square	3	0.111	0.037	2.310	0.145
Current*Current	1	0.009	0.009	0.560	0.474
Standoff Distance*Standoff Distance	1	0.019	0.019	1.210	0.299
Weld Speed*Weld Speed	1	0.093	0.093	5.790	0.039
2-Way Interaction	3	0.426	0.142	8.880	0.005
Current*Standoff Distance	1	0.134	0.134	8.380	0.018
Current*Weld Speed	1	0.176	0.176	10.990	0.009
Standoff Distance*Weld Speed	1	0.116	0.116	7.290	0.024
Error	9	0.144	0.016		
Lack-of-Fit	5	0.068	0.014	0.710	0.648
Pure Error	4	0.076	0.019		
Total	19	3.441			

Table 4.6 ANOVA analysis of Penetration for Inconel 625 deposition

Source	DF	Adj SS	Adj MS	F-Value	P-Value
Model	10	2.502	0.250	12.680	0.044
Blocks	1	0.227	0.227	11.480	0.008
Linear	3	0.465	0.155	7.840	0.007
Current	1	0.139	0.139	7.060	0.026
Standoff Distance	1	0.208	0.208	10.560	0.010
Weld Speed	1	0.117	0.117	5.910	0.038
Square	3	1.140	0.380	19.250	0.023
Current*Current	1	0.199	0.199	10.090	0.011
Standoff Distance*Standoff Distance	1	0.001	0.001	0.040	0.854
Weld Speed*Weld Speed	1	0.994	0.994	50.340	0.016
2-Way Interaction	3	0.671	0.224	11.340	0.022
Current*Standoff Distance	1	0.652	0.652	33.000	0.014
Current*Weld Speed	1	0.001	0.001	0.060	0.805
Standoff Distance*Weld Speed	1	0.019	0.019	0.940	0.358
Error	9	0.178	0.020		
Lack-of-Fit	5	0.076	0.015	0.600	0.706
Pure Error	4	0.101	0.025		
Total	19	2.680			

Table 4.7 ANOVA analysis of Dilution for Inconel 625 deposition

Source	DF	Adj SS	Adj MS	F-Value	P-Value
Model	10	314.786	31.479	17.720	0.035
Blocks	1	147.507	147.507	83.040	0.028
Linear	3	79.455	26.485	14.910	0.001
Current	1	1.233	1.233	0.690	0.426
Standoff Distance	1	0.228	0.228	0.130	0.729
Weld Speed	1	77.994	77.994	43.910	0.046
Square	3	32.048	10.683	6.010	0.016
Current*Current	1	26.134	26.134	14.710	0.004
Standoff Distance*Standoff Distance	1	3.925	3.925	2.210	0.171
Weld Speed*Weld Speed	1	5.189	5.189	2.920	0.122
2-Way Interaction	3	55.778	18.593	10.470	0.003
Current*Standoff Distance	1	7.557	7.557	4.250	0.069
Current*Weld Speed	1	1.945	1.945	1.100	0.023
Standoff Distance*Weld Speed	1	46.275	46.275	26.050	0.018
Error	9	15.986	1.776		
Lack-of-Fit	5	13.767	2.753	4.960	0.073
Pure Error	4	2.219	0.555		
Total	19	330.772			

The ANOVA analysis for the Inconel 625 deposition characteristics is shown in Table 4.4,Table 4.5, Table 4.6, and Table 4.7. It is observed that the two way interaction terms have more influence than the main and square terms. The polynomial equations for the Inconel 625 bead deposition characteristics are predicted using Eq 4.5, Eq 4.6, Eq 4.7, and Eq 4.8. The developed models are adequate and are good enough to predict the responses. This can be checked by the regression coefficient. The R^2 values for bead width, bead height, penetration, and dilution are 94.27, 95.82, 93.37, and 95.17 respectively.

$$\text{Bead Width } W = 20.30 - 0.044\, I - 3.66\, D - 34.39\, S - 0.001249\, I^2 - 0.1054\, D^2 + 5.56\, S^2 + 0.04865\, I*D + 0.2835\, I*S - 0.385\, D*S \tag{4.5}$$

$$\text{Bead Height } H = 9.56 - 0.0622\, I - 0.535 D - 7.06\, S - 0.000260\, I^2 - 0.0383\, D^2 - 8.37\, S^2 + 0.01294 I*D + 0.1482\, I*S - 1.207\, D*S \tag{4.6}$$

$$\text{Penetration } P = -0.55 + 0.1169\, I - 2.800\, D + 16.25\, S - 0.001228\, I^2 - 0.0073\, D^2 - 27.43\, S^2 + 0.02854\, I*D - 0.0126\, I*S + 0.481 S*D \tag{4.7}$$

$$\text{Dilution} = -212.6 + 3.182\, I + 22.52\, D + 132.7\, S - 0.01407\, I^2 - 0.545\, D^2 - 62.7\, S^2 - 0.0972\, I*D + 0.493\, I*S - 24.05\, S*D \tag{4.8}$$

Table 4.8 ANOVA analysis of bead width for stainless steel 304 deposition

Source	DF	Adj SS	Adj MS	F-Value	P-Value
Model	10	11.303	1.130	14.860	0.026
Blocks	1	0.681	0.681	8.950	0.015
Linear	3	3.504	1.168	15.350	0.001
Current	1	0.006	0.006	0.080	0.086
Standoff Distance	1	2.192	2.192	28.820	0.016
Weld Speed	1	1.305	1.305	17.160	0.003
Square	3	3.664	1.221	16.050	0.031
Current*Current	1	0.039	0.039	0.520	0.490
Standoff Distance*Standoff Distance	1	3.463	3.463	45.520	0.038
Weld Speed*Weld Speed	1	0.335	0.335	4.400	0.065
2-Way Interaction	3	3.454	1.151	15.140	0.001
Current*Standoff Distance	1	0.039	0.039	0.510	0.495
Current*Weld Speed	1	3.034	3.034	39.890	0.047
Standoff Distance*Weld Speed	1	0.382	0.382	5.010	0.052
Error	9	0.685	0.076		
Lack-of-Fit	5	0.635	0.127	10.180	0.072
Pure Error	4	0.050	0.012		
Total	19	11.987			

Table 4.9 ANOVA analysis of bead height for stainless steel 304 deposition

Source	DF	Adj SS	Adj MS	F-Value	P-Value
Model	10	134.360	13.436	16.970	0.013
Blocks	1	2.197	2.197	2.780	0.130
Linear	3	97.630	32.543	41.110	0.028
Current	1	2.297	2.297	2.900	0.123
Standoff Distance	1	6.337	6.337	8.010	0.020
Weld Speed	1	88.996	88.996	112.440	0.010
Square	3	24.123	8.041	10.160	0.003
Current*Current	1	6.703	6.703	8.470	0.017
Standoff Distance*Standoff Distance	1	0.139	0.139	0.180	0.685
Weld Speed*Weld Speed	1	15.620	15.620	19.730	0.002
2-Way Interaction	3	10.409	3.470	4.380	0.037
Current*Standoff Distance	1	0.098	0.098	0.120	0.733
Current*Weld Speed	1	2.271	2.271	2.870	0.125
Standoff Distance*Weld Speed	1	8.040	8.040	10.160	0.011
Error	9	7.124	0.792		
Lack-of-Fit	5	3.990	0.798	1.020	0.507
Pure Error	4	3.134	0.784		
Total	19	141.484			

Table 4.10 ANOVA analysis of bead penetration for stainless steel 304 deposition

Source	DF	Adj SS	Adj MS	F-Value	P-Value
Model	10	2.529	0.253	15.560	0.022
Blocks	1	0.273	0.273	16.820	0.003
Linear	3	0.534	0.178	10.950	0.002
Current	1	0.089	0.089	5.490	0.047
Standoff Distance	1	0.355	0.355	21.860	0.001
Weld Speed	1	0.089	0.089	5.490	0.044
Square	3	0.017	0.006	0.350	0.793
Current*Current	1	0.015	0.015	0.900	0.368
Standoff Distance*Standoff Distance	1	0.000	0.000	0.000	0.978
Weld Speed*Weld Speed	1	0.001	0.001	0.090	0.769
2-Way Interaction	3	1.705	0.568	34.960	0.043
Current*Standoff Distance	1	0.678	0.678	41.700	0.014
Current*Weld Speed	1	0.067	0.067	4.110	0.073
Standoff Distance*Weld Speed	1	0.960	0.960	59.070	0.034
Error	9	0.146	0.016		
Lack-of-Fit	5	0.100	0.020	1.740	0.307
Pure Error	4	0.046	0.012		
Total	19	2.675			

Table 4.11 ANOVA analysis of Dilution for stainless steel 304 deposition

Source	DF	Adj SS	Adj MS	F-Value	P-Value
Model	10	134.360	13.436	16.970	0.023
Blocks	1	2.197	2.197	2.780	0.030
Linear	3	97.630	32.543	41.110	0.050
Current	1	2.297	2.297	2.900	0.023
Standoff Distance	1	6.337	6.337	8.010	0.020
Weld Speed	1	88.996	88.996	112.440	0.033
Square	3	24.123	8.041	10.160	0.003
Current*Current	1	6.703	6.703	8.470	0.017
Standoff Distance*Standoff Distance	1	0.139	0.139	0.180	0.685
Weld Speed*Weld Speed	1	15.620	15.620	19.730	0.002
2-Way Interaction	3	10.409	3.470	4.380	0.037
Current*Standoff Distance	1	0.098	0.098	0.120	0.733
Current*Weld Speed	1	2.271	2.271	2.870	0.025
Standoff Distance*Weld Speed	1	8.040	8.040	10.160	0.011
Error	9	7.124	0.792		
Lack-of-Fit	5	3.990	0.798	1.020	0.507
Pure Error	4	3.134	0.784		
Total	19	141.484			

The ANOVA analysis for the stainless steel 304 deposition characteristics is tabulated in, Table 4.8, Table 4.9, Table 4.10, and Table 4.11. It is observed that the two way interaction terms have more influence than the main and square terms. The polynomial equations for the Inconel 625 bead deposition characteristic sare can be predicted using Eq 4.9, Eq 4.10, Eq 4.11, and Eq 4.12. The developed models are adequate and are good enough to predict the responses. This can be checked by the regression coefficient. The R2 values for bead width, bead height, penetration, and dilution are 94.29, 97.40, 94.53, and 94.96 respectively.

The polynomial equations for the stainless steel 304 bead deposition characteristics are predicted using the below equations

$$\text{Bead Width } W = 0.71 - 0.039\, I + 6.06\, D - 44.2\, S - 0.000546\, I^2 - 0.5121\, D^2 - 15.92\, S^2 - 0.00694\, I*D + 0.6159\, I*S - 2.184\, D*S \tag{4.9}$$

$$\text{Bead Height}(H) = -9.29 + 0.1161\, I + 6.699\, D - 64.73\, S - 0.000015\, I^2 - 0.2339\, D^2 + 3.63\, S^2 - 0.05144\, I*D + 0.5296\, I*S + 1.651\, D*S \tag{4.10}$$

$$\text{Penetration } P = 6.43 - 0.0598\, I - 2.025\, D + 25.01\, S - 0.000332\, I^2 - 0.0010\, D^2 + 1.06\, S^2 + 0.02911\, I*D - 0.0914\, I*S - 3.464\, D*S \tag{4.11}$$

$$\text{Dilution} = -43.3 + 1.598\, I - 0.19\, D - 87.9\, S - 0.00712\, I^2 - 0.102\, D^2 + 108.8\, S^2 - 0.0111\, I*D - 0.533\, I*S + 10.03\, D*S \tag{4.12}$$

4.3.3. Process parameters optimization using Response Surface Method

The optimum operating parameter conditions for better deposition are acquired using the response surface optimizer module. Figure 4.9 shows the multi-objective optimization plots for bead width, bead height, penetration, and dilution. From the response optimizer analysis, the combined multi-objective response can be attained at 116.330 Amps, 5.115 mm standoff distance, and 0.4633 m/min weld speed.

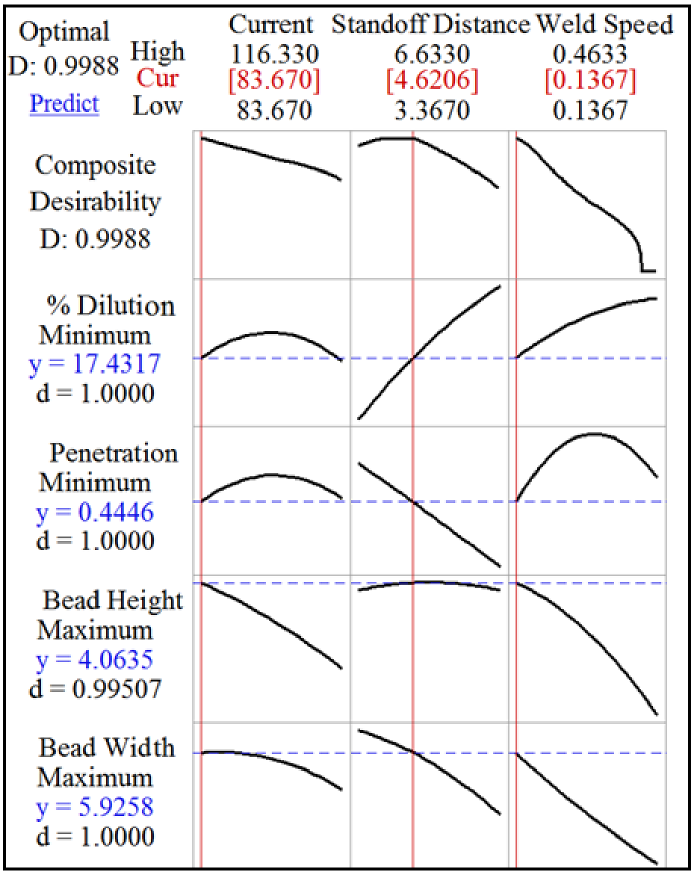

Figure 4.9 Response optimization plots for Inconel 625 deposition characteristics

4.4. Chapter summary

Process parameter's effect on bead characteristics that were deposited by cold metal transfer based additive manufacturing process was studied and the observations are summarized below.

- Single clad beads were successfully deposited using the cold metal transfer deposition process.
- The empirical models developed by regression analysis were able to predict the correlations between process variables and bead characteristics for the range of parameters (such as current: 90–110 A; Standoff distance: 4-6 mm and weld speed: 0.2-0.4 m/min) and material used in the present study.
- The bead characteristics are predominantly influenced by both main and interaction parameters effect and therefore their effects cannot be neglected.

- The optimum process parameters for minimum penetration, minimum dilution, maximum height, and maximum width for multipass multi-track depositions are found to be at current = 116.330 A, standoff distance = 5.115 mm, and weld speed = 0.4633 m/min.

Chapter 5

Multi response optimization of Inconel 625 wire arc deposition for development of additive manufactured components using Grey relational analysis (GRA)

This chapter investigates the multi response optimization of single bead deposition characteristics which affects the additive manufactured structures in later stages of multi layered depositions. Inconel 625 single beads were deposited using the cold metal transfer (CMT) based on Wire Arc Additive Manufacturing (WAAM). The bead width, bead height, penetration depth, and microhardness of the fusion region are considered for the decision criteria model. Grey relational analysis (GRA) is used to solve the multi criteria optimization problem. Analysis of variance has been performed to quantify the effects of the parameters on grey relational grade (GRG).

5.1.Introduction

5.1.1. Grey Relational Analysis

A system is said to be White if in which all relevant information is known, while a system in which all the relevant information is completely unknown is known as the Black system. Any system where available information is limited is known as the Grey system. To get the proposed response with minimum input resources, the grey system theory was developed by Deng (1982) through his research to solve multi-attribute decision-making problems by combining multiple attributes into a single attribute[118]. In GRA, the experimental values of the response were normalized in the range of zero to one. This is called grey relational generation. The grey relational coefficient is further computed. The overall performance of different alternatives was represented by grey relational grades (GRG). The highest GRG represents the optimal set of process parameters to achieve overall performance. The objective of real time situations is multi-objective. Hence it is essential to convert a multi optimization problem into a single objective function through statistical approaches. The procedure followed in GRA is

(1) Normalize the data obtained from experiments from zero to one
(2) Grey relational coefficients has to be evaluated from the normalized data
(3) Obtain overall grey relational grade (GRG)

From the GRG whichever the experimental condition has got Rank 1 is considered to be the optimal setting that satisfies all the objective functions.

The characteristics equations for normalizing the minimization and maximization problems are obtained by using the Eqs. (1) and (2).

$$x_i^*(k) = \frac{\max(x_i^o k) - x_i^o(k)}{\max(x_i^o(k)) - \min(x_i^o(k))} \qquad (5.1)$$

$$x_i^*(k) = \frac{x_i^o(k) - \min(x_i^o k)}{\max(x_i^o(k)) - \min(x_i^o(k))} \tag{5.2}$$

Where $x_i^*(k)$ the sequence data is after normalization $x_i(k)$ is the actual response value, $\max(x_i^o(k))$ its maximum value, and $\min(x_i^o(k))$ is the minimum value of the generated data.
After the normalization matrix obtained from the experimental data, Grey relational coefficients are obtained to estimate the relationship between normalized data and actual data and is calculated using the Eqn (3)

$$\xi(k) = \frac{\Delta_{\min} + \xi\Delta_{\max}}{\Delta o_i(k) + \xi\Delta_{\max}} \tag{5.3}$$

Where $\Delta o_i(k)$ is deviation sequence and is calculated as $|x_i^*(k) - x_i^o(k)|$ ξ is the distinguished coefficient and the value is ranging between 0 to 1. In general, it is taken as 0.5
The next step is to obtain the Grey Relational Grade (GRG) and is defined as

$$\gamma_i = \frac{1}{n}\sum_{k=1}^{n} w_k \xi_i(k) \tag{5.4}$$

Where w_k is the weight factor

The Grey relation evaluation concepts have drawn significant interest among researchers. Some researchers worked to optimize the multi-objective optimization using GRA [119]. Different multi-attribute methods namely AD, TRIZ, Fuzzy, Grey relational analysis, and feasibility approaches are demonstrated by Wu et.al [120]. Design of experiments (Taguchi designs and Response surface Designs) are coupled with GRA has been performed by many researchers for manufacturing methods such as castings, forming, welding, as well as for machining applications like turning, milling, drilling, etc. Tzeng et. al studied turning process optimization using grey relational analysis. L9 Taguchi design was used for the experimentation. The average roughness and roundness of the machined samples are taken into consideration for multi-objective optimization. It was observed that the depth of cut and cutting speed are the most influencing parameters for average roughness and maximum roundness[121]. Prakash utilized the grey relational analysis approach for multi-attribute optimization of turning the Aluminum composite. Results show that cutting feed has a remarkable effect on the multi-attribute response characteristics[122]. Rajeswari et.al studied multi-objective optimization of the milling process using RSM coupled with GRA. Maximum material removal rate and minimum surface roughness, tool wear, cutting force are considered for the study. Box-Behnken Design was used to conduct the experiments on Aluminium 7075 composites with SiC and Alumina s reinforcements. And it was observed that the appropriate optimal setting parameters from GRA produce low cutting forces, less wear with fine surface finish as well as maximum material removal rate[123]. Lu et. al explores the multiple performances of high speed end milling of tool steel using grey relational analysis. Metal removal rates and tool life are considered for the study. The weights for the responses are evaluated by principal component analysis. This method effectively acquires the optimal setting combination of milling characteristics[124].

Xu et al used Taguchi based grey relational analysis on tailor-welded blanks (TWBs) to improve the performance of the joint. The peak crashing force (Fmax), the total weight (Mass), and the total energy absorption (EA) are chosen for multi performance analysis. Results demonstrate that the grey correlation of the structure enhances the crashworthiness of TWBs [125]. Srirangan et al investigate Incoloy 800HT welded with tungsten inert arc welding process and multi-objective optimization of tensile strength, yield strength, and impact strength using grey relational analysis[126]. Chen et al performed a grey relational analysis for CO_2 laser machined polymethyl methacrylate plates. The multiple performance study involves surface roughness and transmission ratio concerning the process parameters. This investigation used an L9 orthogonal array to conduct the experiments. From the results, it was observed that the gas flow rate has more influence on the performance characteristics[127]. Tamrin et.al investigated multiple quality characteristics of a CO_2 laser welded dissimilar material lap joint as a function of welding parameters. A full-factorial experiment is followed for experimentation. Grey relational analysis (GRA) is used to find out the optimal setting parameters for the combined responses. ANOVA is carried out to know the influential parameters and found that weld speed has more percentage of contribution to predict the responses [128]. Shanmugarajan et al. applied GRA to find out the optimum parameter settings for creep strength ferritic steels used for high temperature applications which are process in CO_2 laser welding and were able to closely predict the experimental values [129]. Pan et al studied titanium alloy plates joined with Nd: YAG laser welding and determine the multiple quality characteristics optimization using Taguchi coupled with grey relational analysis. GRA successfully train the optimum parameter which satisfy the multiple performance characteristics. This new approach improves the performance of the welded joints [130]. Prajapathi et al investigated the optimization of performance characteristics of regulated metal deposition (RMD) welding of stainless steel. Bead width, depth of penetration, and heat-affected zone are considered for the study. An integrated fuzzy system with Taguchi design is used along with the grey relational analysis. From the results, it was observed that voltage is the most influencing parameter than other process parameters to evaluate the multi performance of the RMD process[131]. Tarng et al use grey relational analysis to solve multiple performances of the submerged arc welding process (SAW). Results reveal that the Taguchi based GRA effectively determined the combination parameter settings for the multiple performances of the process[132].

5.1.2. Scope of work

In the present study, the cold metal based wire arc deposition process is used to prepare the samples. The single bead depositions which are treated as the building blocks of any additive manufactured components have more influence on the mechanical and metallurgical properties of the additive manufactured components. The depositions should have optimum bead characteristics as well as mechanical strength. Hence, multi-decision criteria optimization is required to establish better processing conditions through which quality tracks or beads are made. The same conditions can be used and good quality additive manufactured components are produced with multi-pass multi-track depositions.

Even though most of the literature is available on multi-objective optimization of conventional manufacturing and machining processes, a few are demonstrated to apply multi decision criteria methods and their effectiveness in the production of additive manufacturing samples and components.

Hence, in the present work, an attempt has been made to investigate multi-objective optimization of Inconel 625 bead characteristics deposited by CMT using the RSM coupled with GRA. Three parameters namely current, weld speed, and standoff distance are selected to run the experiment. GRA is applied to estimate optimum operating conditions. As the bead width is increased, the deposition material flows on the layered surface and it affects the succeeded layers. Less bead height increases more number of layers to deposit, more the number of layers results in low roughness values. The penetration depth directly affects the bonding strength of the layer interface regions. Hence, the optimum responses are chosen as a minimum bead width, minimum bead height, maximum penetration, and maximum microhardness.

5.2. Material data and experimental method

Inconel 625 single bead deposition samples were prepared using the experimental design as mentioned in Table 5.1 on a mild steel substrate. The experiments were randomly conducted to ensure the results are free from experimental bias. The bead characteristics such as bead width, bead height, and penetration were observed from the micrographs through 3d optical microscope (Make: QASMO optical microscope DIC polarizer, Model: QX4RT) at 1000 microns scale as shown in Figure 5.1 and microhardness testing was conducted on a Vickers microhardness tester with a load of 500 grams. Later GRA steps were followed to obtain the combined optimum parameter.

Table 5.1 Central composite response surface design for conducting experiments

Std.Order	Run Order	Current in A	Standoff Distance in mm	Weld Speed in m/min
5	1	90	4	0.4
9	2	100	5	0.3
10	3	100	5	0.3
1	4	90	4	0.2
12	5	100	5	0.3
11	6	100	5	0.3
2	7	110	4	0.2
8	8	110	6	0.4
3	9	90	6	0.2
7	10	90	6	0.4
6	11	110	4	0.4
4	12	110	6	0.2
13	13	83.67	5	0.3
14	14	116.33	5	0.3
18	15	100	5	0.46
15	16	100	3.36	0.3
19	17	100	5	0.3
20	18	100	5	0.3
16	19	100	6.63	0.3
17	20	100	5	0.14

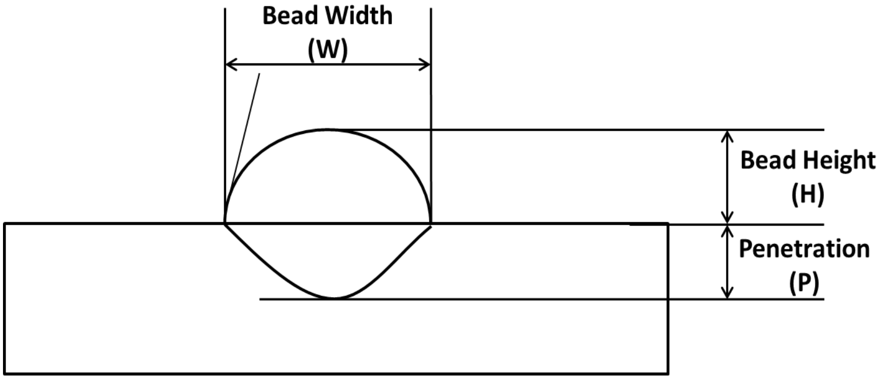

Figure 5.1 Schematic diagram of bead characteristic measurement

5.3. Results and discussions

Inconel 625 single beads were successfully deposited on a mild steel substrate as depicted in Figure 5.2. The samples were cut in the middle of the plate. The micrographs of the samples are presented in Figure 5.3. Since, for additively layered structures smooth, flat, and thin layers are recommended for the deposition of successive layers. Hence, the minimum bead width, minimum bead height, and maximum penetration are the desired objectives for the present study. The observed responses are listed in Table 5.2

Figure 5.2 Inconel 625 deposition clads on mild steel substrate

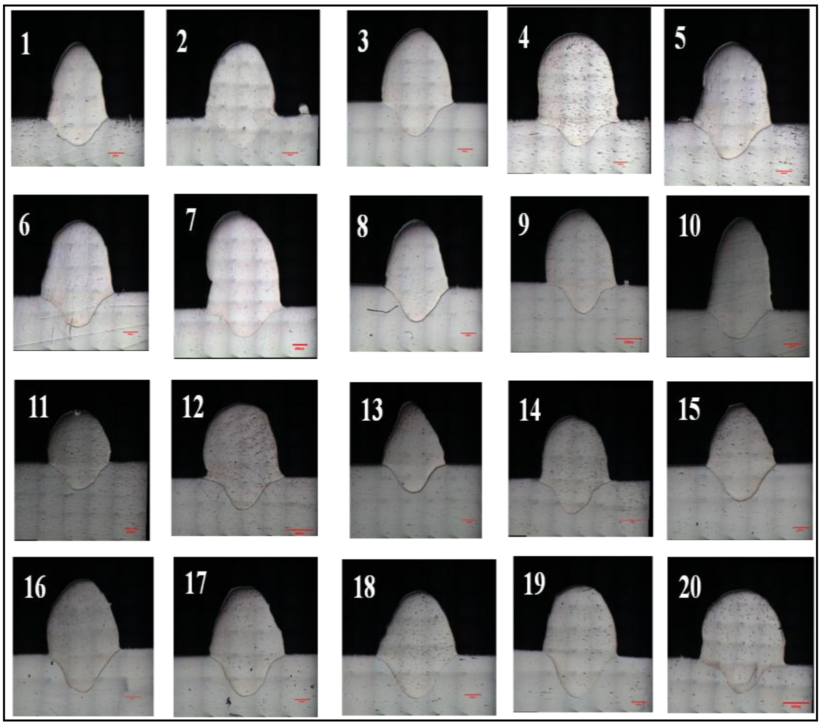

Figure 5.3 Macro graphs of bead profiles

Table 5.2 Responses for multi decision optimization

Sample No	Bead Width (mm)	Bead Height (mm)	Penetration depth (mm)	Microhardness (VHN)
1	3.901	3.217	1.197	225.925
2	4.732	3.732	1.794	231.500
3	5.164	3.734	1.419	216.750
4	5.637	4.072	1.253	222.275
5	5.082	3.179	1.711	163.300
6	4.833	3.531	3.531	215.750
7	2.696	2.371	0.767	215.500
8	4.477	3.123	1.739	207.350
9	2.653	1.935	0.786	221.325
10	3.858	3.68	1.134	226.950
11	2.281	1.592	0.872	206.575
12	5.912	3.868	1.775	229.625
13	4.133	2.778	1.281	219.100
14	5.209	3.194	1.711	205.900
15	4.425	2.351	1.481	216.350
16	4.643	2.951	1.668	241.050
17	4.655	2.896	1.679	218.575
18	4.901	3.397	1.84	218.350
19	4.803	3.062	1.94	208.175
20	3.332	1.898	0.858	230.675

In the present study, all the responses are given equal priority therefore the responses have an equal weightage of 0.25 in the GRA evaluation process. The normalization data calculated from the original responses are presented in Table 5.3 and followed by the deviation matrix in

Table *5.4*.

With an equal weightage of 0.25, the final grey relational grade (GRG) was evaluated and the combined GRG with the four responses are presented inTable 5.5. All the experiments were given ranks based on the GRG grade. From Table 5.5, it is observed that sample no 6 has rank 1 with the highest grade of 0.703. Hence this condition is treated as an optimal parameter setting that satisfies all four responses. Different parameter settings can be obtained with different weightage combinations, which depend on the desired performance and application. The performance measures will depend on the weightage combination. Different weights can be given to the responses based on the priorities and requirements for the specific applications.

Table 5.3 Normalized values

Normalization table				
Sample No	Bead Width (mm)	Bead Height (mm)	Penetration depth (mm)	Microhardness (VHN)
1	0.554	0.345	0.156	0.805
2	0.325	0.137	0.372	0.877
3	0.206	0.136	0.236	0.687
4	0.076	0.000	0.176	0.759
5	0.229	0.360	0.342	0.000
6	0.297	0.218	1.000	0.675
7	0.886	0.686	0.000	0.671
8	0.395	0.383	0.352	0.567
9	0.898	0.862	0.007	0.746
10	0.566	0.158	0.133	0.819
11	1.000	1.000	0.038	0.557
12	0.000	0.082	0.365	0.853
13	0.490	0.522	0.186	0.718
14	0.194	0.354	0.342	0.548
15	0.410	0.694	0.258	0.682
16	0.349	0.452	0.326	1.000
17	0.346	0.474	0.330	0.711
18	0.278	0.272	0.388	0.708
19	0.305	0.407	0.424	0.577
20	0.711	0.877	0.033	0.867

Table 5.4 Deviation sequence matrix

Deviation sequence (Δ_{oi}) table				
Sample No	Bead Width (mm)	Bead Height (mm)	Penetration depth (mm)	Microhardness (VHN)
1	0.446	0.655	0.844	0.195
2	0.675	0.863	0.628	0.123
3	0.794	0.864	0.764	0.313
4	0.924	1.000	0.824	0.241
5	0.771	0.640	0.658	1.000
6	0.703	0.782	0.000	0.325
7	0.114	0.314	1.000	0.329
8	0.605	0.617	0.648	0.433
9	0.102	0.138	0.993	0.254
10	0.434	0.842	0.867	0.181
11	0.000	0.000	0.962	0.443
12	1.000	0.918	0.635	0.147
13	0.510	0.478	0.814	0.282
14	0.806	0.646	0.658	0.452
15	0.590	0.306	0.742	0.318
16	0.651	0.548	0.674	0.000
17	0.654	0.526	0.670	0.289
18	0.722	0.728	0.612	0.292
19	0.695	0.593	0.576	0.423
20	0.289	0.123	0.967	0.133

Table 5.5 Grey relational grading and ranking

			Grey Relation grade			
Sample No	Bead Width (mm)	Bead Height (mm)	Penetration depth (mm)	Microhardness (VHN)	Combined GRA Coefficient	Rank
1	0.528	0.433	0.372	0.720	0.509	9
2	0.426	0.367	0.443	0.803	0.537	6
3	0.386	0.367	0.396	0.615	0.456	18
4	0.351	0.333	0.378	0.674	0.456	17
5	0.393	0.439	0.432	0.333	0.397	20
6	0.416	0.390	1.000	0.606	0.703	1
7	0.814	0.614	0.333	0.603	0.529	7
8	0.453	0.447	0.435	0.536	0.470	16
9	0.830	0.783	0.335	0.663	0.575	5
10	0.535	0.373	0.366	0.734	0.503	11
11	1.000	1.000	0.342	0.530	0.596	3
12	0.333	0.353	0.440	0.773	0.511	8
13	0.495	0.511	0.381	0.639	0.495	13
14	0.383	0.436	0.432	0.525	0.453	19
15	0.459	0.620	0.403	0.611	0.506	10
16	0.435	0.477	0.426	1.000	0.607	2
17	0.433	0.487	0.427	0.634	0.499	12
18	0.409	0.407	0.450	0.631	0.492	14
19	0.419	0.458	0.465	0.542	0.480	15
20	0.633	0.802	0.341	0.789	0.588	4

Table 5.6 ANOVA for grey relational grade

Source	DF	Adj SS	Adj MS	F-Value	P-Value
Regression	9	0.028882	0.003209	7.15	0.002
Current	1	0.00362	0.00362	8.07	0.018
Standoff Distance	1	0.004658	0.004658	10.38	0.009
Weld Speed	1	0.000028	0.000028	0.06	0.809
Current*Current	1	0.001512	0.001512	3.37	0.096
Standoff Distance*Stanndoff Distance	1	0.000816	0.000816	1.82	0.207
Weld Speed*Weld Speed	1	0.003745	0.003745	8.35	0.016
Current*Standoff Distance	1	0.008325	0.008325	18.56	0.002
Current*Weld Speed	1	0.000239	0.000239	0.53	0.482
Standoff Distance*Weld Speed	1	0.006928	0.006928	15.44	0.003
Error	10	0.004486	0.000449		
Lack-of-Fit	5	0.002639	0.000528	1.43	0.352
Pure Error	5	0.001847	0.000369		
Total	19	0.033368			

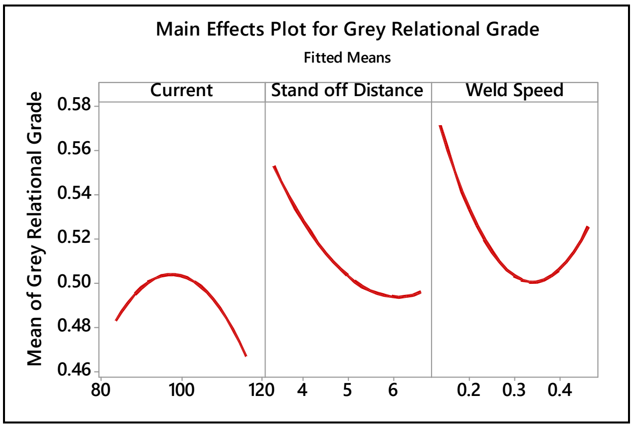

Figure 5.4 Grey relational grade response graph

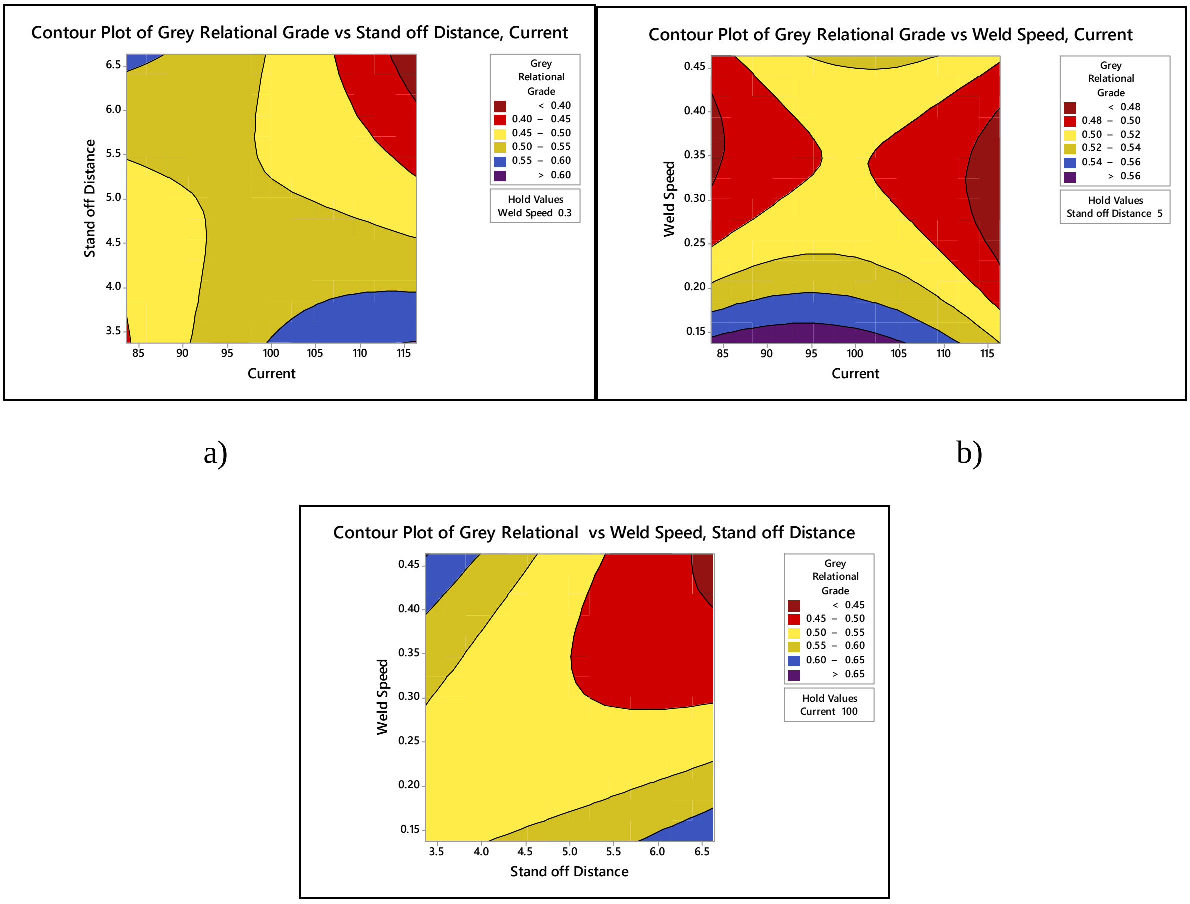

a) b)

c)

Figure 5.5 2D contours graphs a) current and standoff distance vs. GRG, b) current and weld speed vs. GRG, and c) weld speed and standoff distance vs. GRG.

The main effects plots from the GRG have been depicted in Figure 5.4. It was obtained by averaging the GRG values at all the levels for each parameter. The maximum peak from the graph indicates that the level has more influence on the combined multi response characteristics. Likewise, from Figure 5.4 it is obvious that 83.67amps current, standoff distance at 3.367mm, and weld speed of 0.1367 mm/sec have maximum influence on combined response characteristics.

The experimental RSM design with GRG data was analyzed using Minitab software. 2D surface contours have been plotted to analyze the effect of process parameters (current, weld speed, and standoff distance) on calculated GRG from all the responses. Figure 5.5a shows the effect of current and standoff distance on GRG at a constant weld speed of 0.3 mm/sec. It is observed from Figure 5.5a that an increase in current and standoff increases the GRG values thereby performance characteristics also. Figure 5.5b shows the effect of current and weld speed on GRG at a constant standoff distance of 5 mm. the GRG is noted to decrease with the increase of weld speed and current. Figure 5.5c shows the effect of weld speed and standoff distance on GRG at a constant current of 100 amperes. It is evident that increasing standoff distance decrease GRG and increasing weld speed increases GRG. Analysis of variance (ANOVA) has been performed to study the effect of process parameters on multiple response GRG grades. The ANOVA results are tabulated in Table 5.6. The results show that the interaction effects of current and standoff distance and square of weld speed are more significant than the other parameters at a 95% confidence level.

5.4. Chapter summary

In this chapter, Grey relational analysis was applied to response surface design experiments to evaluate the multi-objective performance of bead characteristics deposited by the cold metal transfer process. The deposition characteristics namely bead width, bead height, penetration, and microhardness are considered for the present study. From the GRA analysis, the simultaneous objective of maximum bead width, minimum height, and minimum penetration, maximum microhardness is observed at 100 Amperes current, 5 mm/min weld speed, and 0.3 mm standoff distance. Any specific performance measure can be adjusted so that the other performance metrics satisfy the minimum requirement.

Moreover, for any additive manufacturing process, the deposition and interfacial characteristics of single beads are crucial to building the layers in successive depositions. The bead characteristics greatly affect the layer height, surface roughness, and interfacial characteristics. Hence, the multi-objective criteria have to be followed to develop the AM process from the CMT based wire arc deposition process. Further, the present results give an idea of the combined performance of bead deposition characteristics and mechanical strength which may help the conversion of single bead deposition into a multipass multi-track deposition which tends to be an additive manufacturing process.

Chapter 6

Effect of wire arc deposition parameters on bead geometry and melting characteristics of Inconel superalloy

In this chapter, the effect of the arc deposition process on bead characteristics and melting characteristics of Inconel 625 single pass bead deposition is discussed. The deposition parameters in terms of heat input are discussed thoroughly on melting characteristics. The effect of heat input and process parameters on bead characteristics such as bead width, bead height, penetration, dilution, deposited area, and penetration area. The measurements were observed from the cross-sections of the samples. Dilution and melting efficiencies were calculated from the measured data.

6.1 Introduction

6.1.1. Melting phenomena and characteristics

The useful amount of the total energy required to create the fusion zone is prescribed as melting efficiency. The amount of energy used to melt the base plate is referred to as plate melting efficiency and the energy required to melt feed wire is termed as electrode melting efficiency. Hence, it is desirable to know the effect of process variables on melting efficiencies as it controls the fusion characteristics. Niles and Jackson [56] studied the effect of arc distribution, process parameters in the GTAW process and observed that the melting and thermal efficiencies increased with weld speed. The authors have compared the amount of energy that goes into the base metal and the amount of energy spent on melting the fusion zone. Modenesi [57] developed numerical models to predict the temperature distributions and melting rate of feed wire in the gas metal arc welding process. The efficiency of the model was improved by adding constants related to the melting rate and welding current. The authors correlated the results with the arc characteristics. Liu et. al [58] used a triple wire arc method to increase melting efficiency. A mirror-symmetrical wire arrangement was adopted with the main wire in the center and two symmetrical wires on both the left and right sides of the main wire. The wire polarity of the main wire and the side wires acted as anode and cathode and the arcs developed between these wires superimposed and improved the penetration, the melting area, and the melting efficiency of the base metal. Suban et.al [59] demonstrated the effect of shielding gas and weld current on melting rate and found that the shielding medium has a negligible influence on the melting rate and is depends on the welding current only. The heat supplied in the deposition process and corresponding melting characteristics are studied as follows.

The heat input (HI) supplied is estimated by Eq 6.1

$$\text{Heat input HI (KJ/mm)} = \eta \frac{I * V}{1000 * S} \tag{6.1}$$

The CMT system used for the experimentation is a manual machine hence the efficiency of the system is considered as 85%.

Since most of the phase changes occur between 500˚C to 900˚C [133] these temperature ranges were considered for calculating the cooling rate and are given in Eq (6.2)-(6.4). [41] [134]

$$\textit{Time to cool from 900˚C to 500˚C } \Delta t_{9/5} = \frac{HI}{2\pi\lambda} \cdot \frac{1}{\rho} \tag{6.2}$$

$$\textit{Where } \frac{1}{\rho} = \frac{1}{500 - T_0} - \frac{1}{900 - T_0} \tag{6.3}$$

$$\textit{Colling rate } CR = \frac{300}{\Delta t_{9/5}} \tag{6.4}$$

Where I is current in amps V is Voltage in volts, S is weld speed in m/min, λ is the thermal conductivity in w/m k, and T_0 is initial room temperature.

The electrode wire melting efficiency, plate melting efficiency, and total melting efficiency of the beads can be estimated by Eq (6.5)-(6.7) [135].

$$E_{em} = \frac{1000A}{0.386 \times 1000HI} \tag{6.5}$$

$$E_{pm} = \frac{1000B}{0.386 \times 1000HI} \tag{6.6}$$

$$E_{tm} = \frac{1000A_T}{0.386 \times 1000HI} \tag{6.7}$$

Where A is the deposited area, B is the reinforcement area, A_T is the total area. The constant value of 0.386 depends on fusion rate and working temperature conditions which are explained below

The heat required to melt 1 gr material = $\Delta H_f + \int_{1800}^{2023} \mathrm{CpdT} \int_{1800}^{2023} C_p dT \int_{1800}^{2023} \mathrm{CpdT}$

The maximum temperature observed while experimentation is 1800 ˚C= 2023K

For Inconel ΔH_f = 210 J/gr and Cp = 0.435 J/ gr ˚C [136]

= 210 + 0.435 [2023-1800]

= 305 J/g

1 gr mass of Inconel with 8.44 g/cm^3 density occupies 118 mm^3 of volume

Hence, 1 J of heat will melt = 118/305 = 0.3868 mm^3 volume of Inconel

Abioye [38] made single tracks on Inconel 625 with a wire-laser assisted fabrication method. The authors varied process parameters namely wire dripping, smooth wire transfer, and wire stubbing at different cladding conditions. The geometrical characteristics of the track such as aspect ratio and contact angle were studied to determine the dilution ratio (%) of the tracks. The key parameters that had a predominant effect on the track geometrical characteristics were found to be wire deposition volume per unit length and energy per unit length of the track. Aspect ratio and dilution ratio positively impacted energy per unit length of track whereas the contact angle showed a negative impact. However, material deposition volume per unit length of track improved directly with contact angle and inversely with aspect ratio and dilution ratio. It is also observed that the aspect ratio and dilution have positive dependency while the contact angle has a negative dependency on energy per unit length. Guo et.al [39] deposited clad beads of Inconel 625 on the surface of AISI 4130 plates using hot wire pulsed TIG welding. A two-layer multiple-track weld overlay was deposited. The authors noticed columnar dendrites, and few planar crystals, and cellular dendrites near the fusion zone. Also, equiaxed grains and steering dendrites were found in the upper portion of the weld overlay. Cong et. al [40] studied the effect of heat input on bead geometry and porosity in the weld beads with different CMT arc modes and observed that CMT-PADV arc mode has better bead characteristics and samples are free from porosity. Shen et. al [41] investigated the effect of heat input on weld bead geometry of steel joins in the submerged arc welding process and found that with an increasing heat input, the bead characteristics like bead width reinforcement, and HAZ size increased. Benyounis et.al [42] studied the effect of heat input on the bead characteristics of laser butt welding of medium carbon steel and developed correlations for bead geometry concerning the heat input. The fusion area, ferritic volume fraction, and the austenitic grain size have been increased with an increase in heat input for AISI 316L steel joints made by gas metal arc welding process. Also, 0.5 and 1.5 kJ/mm heat input conditions has lower ferrite content in heat effected zone and melting zone [43]. Resende et.al [44] studied the influence of weld parameters on bead characteristics. Weglowski et. al [45] investigated the effect of current on metal transfer behaviour in the gas metal arc welding process and found that welding current has a significant impact on metal transfer rate. Karadeniz et. al [46] conducted experiments on the robotic MIG welding machine to investigate the effect of the welding process on penetration and observed that with an increase in weld current, the penetration also increased. Zong et.al [47] have studied the arc, droplet, and weld pool behavior of the TIG- MIG hybrid welding process.

6.1.2. Scope of work

To repair or remanufacture the damaged parts, single bead depositions are more prominent, and single bead deposition studies are helpful to understand the mechanism of multi-pass multi-track depositions which in turn are used as additive manufactured objects. There is a necessity to find the optimal process parameters for automation and high productivity. The optimal settings can simplify the process characteristics and are cost effective also. Hence it is necessary to investigate the effect of process parameters on bead characteristics for a single pass cladding process.

However, in the open literature, very little information is available on heat input effects on bead characteristics especially for Inconel 625 made by the cold metal transfer process. Hence, the present study investigates the influence of deposition parameters and cooling rate on bead characteristics and melting efficiencies.

6.2 Experimental procedure

Single bead depositions are made on mild steel substrate as per the conditions shown in Table 6.1 Heat input, cooling rate, and cooling time are calculated using Eq 6.1 to Eq 6.4. The deposition bead characteristics are measured using a 3D microscope.

Table 6.1 Parameters used for the deposition process

S.No	Current (Amps)	Voltage (Volts)	Weld speed (m/min)	Heat Input(KJ/mm)	Cooling Time (Sec)	Cooling rate (°C/sec)
1	85	17.6	0.3	0.250	4.446	89.969
2	100	18.1	0.3	0.308	5.465	73.198
3	115	18.8	0.3	0.372	6.603	60.580
4	100	18.1	0.1367	0.675	11.993	33.35
5	100	18.1	0.3	0.308	5.465	73.198
6	100	18.1	0.4633	0.199	3.539	113.042

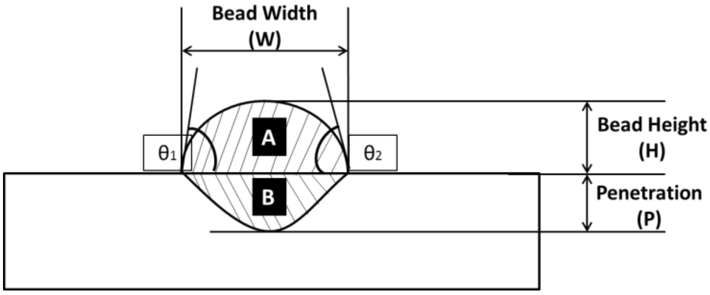

Figure 6.1 Bead geometry measurements

The deposition bead characteristics such as bead width, bead height, penetration were measured on the cross-section surface of the samples. The labeled area, deposition area (A), penetration area (B) as shown in Figure 6.1 are considered for the estimation of % dilution as well as melting efficiencies of the beads. The contact angle is measured concerning the substrate on both sides of the deposition and the average value is considered for analysis. The electrode wire melting efficiency, plate melting efficiency, and total melting efficiency of the beads can be estimated by Eq (6.5)-(6.7) [135].

6.3 Results and discussion

Inconel 625 single-pass beads were successfully deposited on a mild steel substrate plate by the cold metal transfer process. After deposition, 10 x 10 mm samples were extracted from the plate by using wire EDM. Typical 2-D cross-sections of Inconel 625 beads deposited at different process conditions are shown in Figure 6.2. While measuring the bead geometry, it was assumed that the clad geometry is uniform throughout the track. The samples were cut at the middle portion of the track since at the entrance and exit portions of the track bead were irregular and more amount of material was deposited at the entrance.

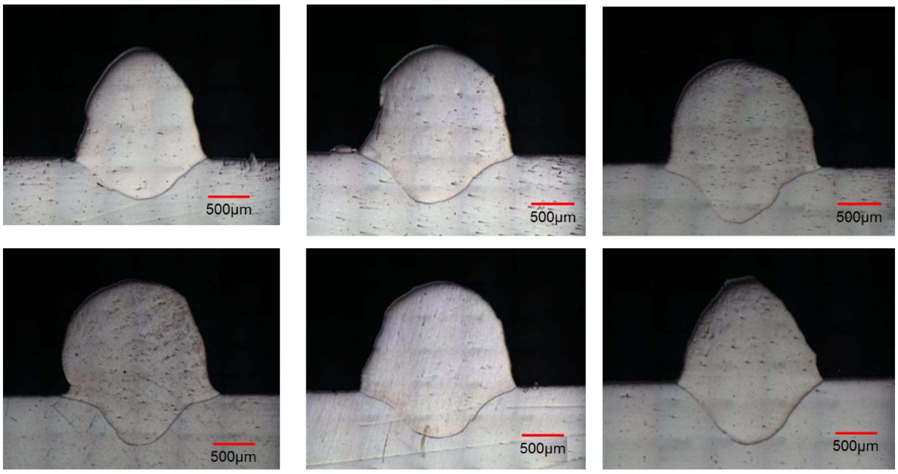

Figure 6.2. Macro graphs of bead profiles

The deposited bead quality depends on the heat flow mechanism during the deposition process. When the material is deposited, heat is transferred to the base material or substrate layer through a heat-affected zone. In the additive manufacturing process, more surface area is available for the deposited layer, and rapid cooling rates have occurred. In the present study, the cooling rate characteristics are considered in between 900˚C to 500˚C. Hence, it is vital to study the heat flow behaviour of the process to investigate the bead characteristics.

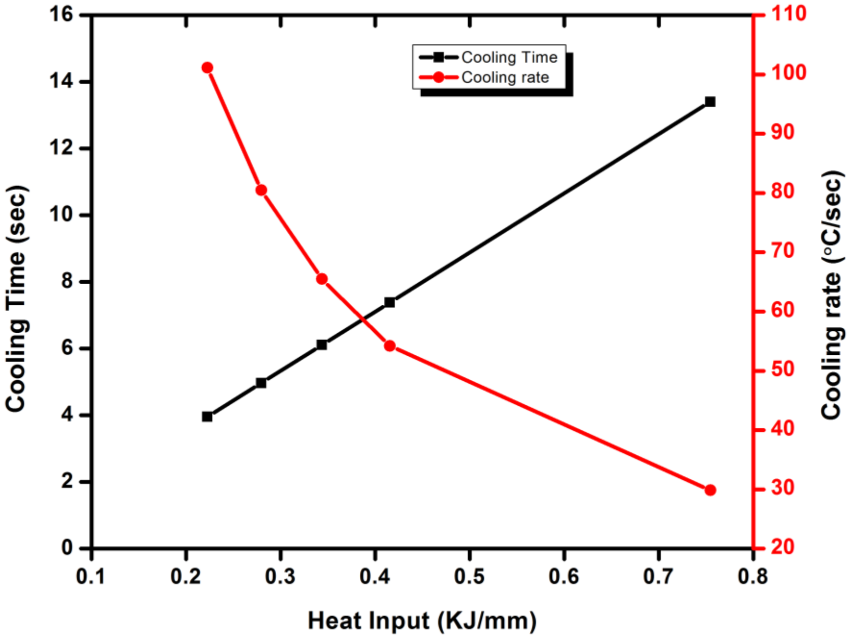

Figure 6.3. Effect of Heat Input on cooling time and cooling rate

Figure 6.3 shows the effect of heat input on cooling time and cooling rate per sec. For Inconel 625 deposited beads, thermal conductivity is 14 W/m K, and the initial temperature is 25˚C. The cooling time and cooling rate were calculated using Equations (2)-(4). From Figure 6.3, it is observed that the cooling time increases with heat input whereas the cooling rate decreased with heat input. Since the bead does not have sufficient time to cool when more heat is accumulated the time required for solidification or cooling is more.

6.3.1. Bead Geometry

The bead geometry such as bead width, bead height, penetration, deposited area, penetration area, and contact angle measured from the bead cross-section micrographs are listed in Table 6.2.

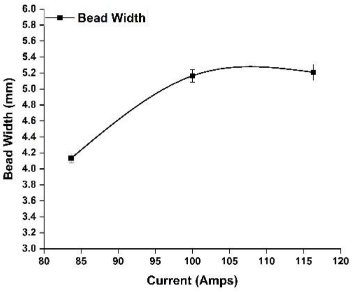

a)

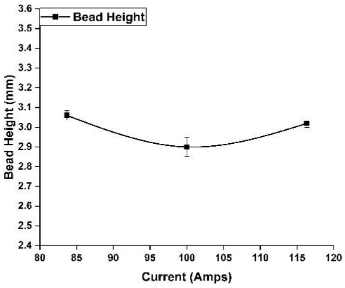

b)

Table 6.2. Effect of process parameters on bead characteristics

S.No	Bead Width (mm)	Bead Height (mm)	Penetration (mm)	Contact Angle (degree)	Dilution (%)	Deposited Area (mm^2)	Penetration Area (mm^2)	Total Area(mm)	Electrode melting efficiency (%)	Plate melting efficiency (%)	Total melting efficiency (%)
1	4.13	3.06	1.28	68.33	28.07	8.75	3.42	12.17	8.105	3.163	11.268
2	5.16	2.90	1.52	68.68	27.85	10.78	4.16	14.94	8.122	3.136	11.258
3	5.21	3.02	1.71	67.79	25.02	13.68	4.57	18.25	8.531	2.847	11.378
4	5.88	3.42	1.83	65.90	24.66	15.69	5.14	20.82	5.386	1.763	7.149
5	4.83	2.90	1.52	68.35	29.90	10.78	4.60	15.38	8.122	3.464	11.587
6	4.43	2.35	1.33	65.76	34.36	8.05	4.21	12.26	9.367	4.903	14.271

6.3.1.1. Effect of deposition parameters on bead geometry

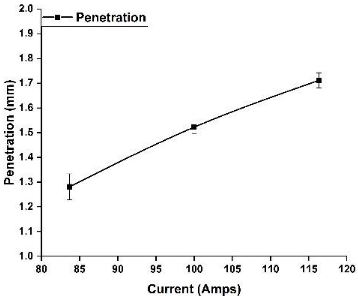

c)

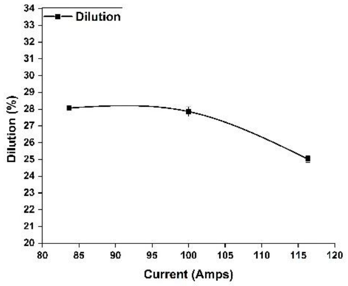

d)

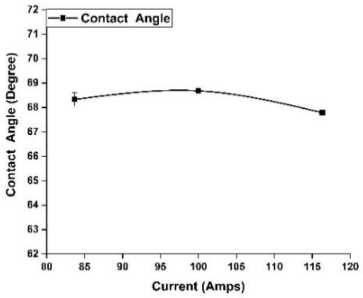

e)

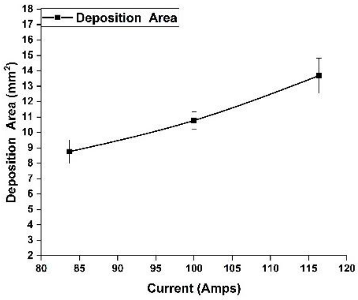

f)

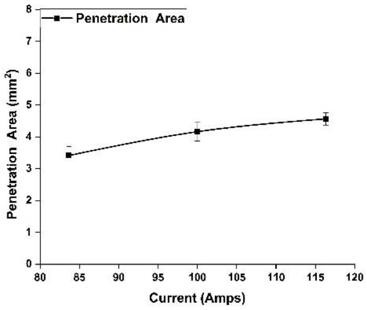

g)

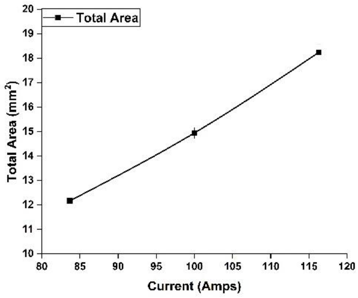

h)

Figure 6.4 (a) - (h) shows the effect of current on Inconel 625 single pass bead geometry. From the plots, it is observed that the bead width, penetration, deposition area, and penetration area increase with current, whereas contact angle and dilution decrease with the current. Bead height even though it shows a reducing trend is almost constant at 3 mm. To investigate the influence of current, the experiments were conducted in the range of 85Amps to 115Amps and weld speed, and standoff distance kept constant at 0.3 m/min and 5mm respectively.

High current implies high electrode or feed wire melting, thereby a large amount of heat is available to fuse the wire which results in changes in bead shape. At higher heat inputs, a large amount of molten material is available for deposition at the fusion zone which causes an increased bead width, penetration, deposition area, and penetration area. A sizeable molten pool at high temperatures will tend to flow on the surface, and hence bead height decreases with heat input [41]. The contact angle of bead height is found to decrease with heat input. From the cooling curves, it is found that when more amount of heat is available, it requires more time for cooling which causes an increase in penetration and penetration area.

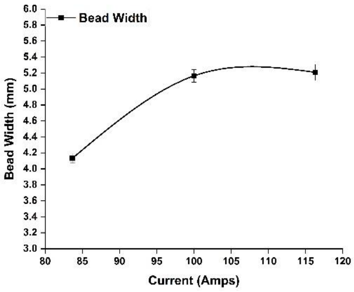

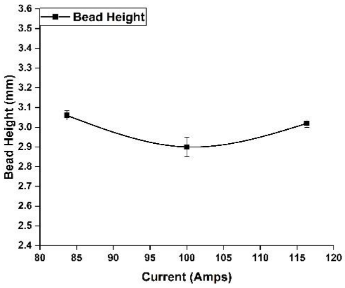

b)

The effect of current on Inconel 625 single pass bead geometry is presented in

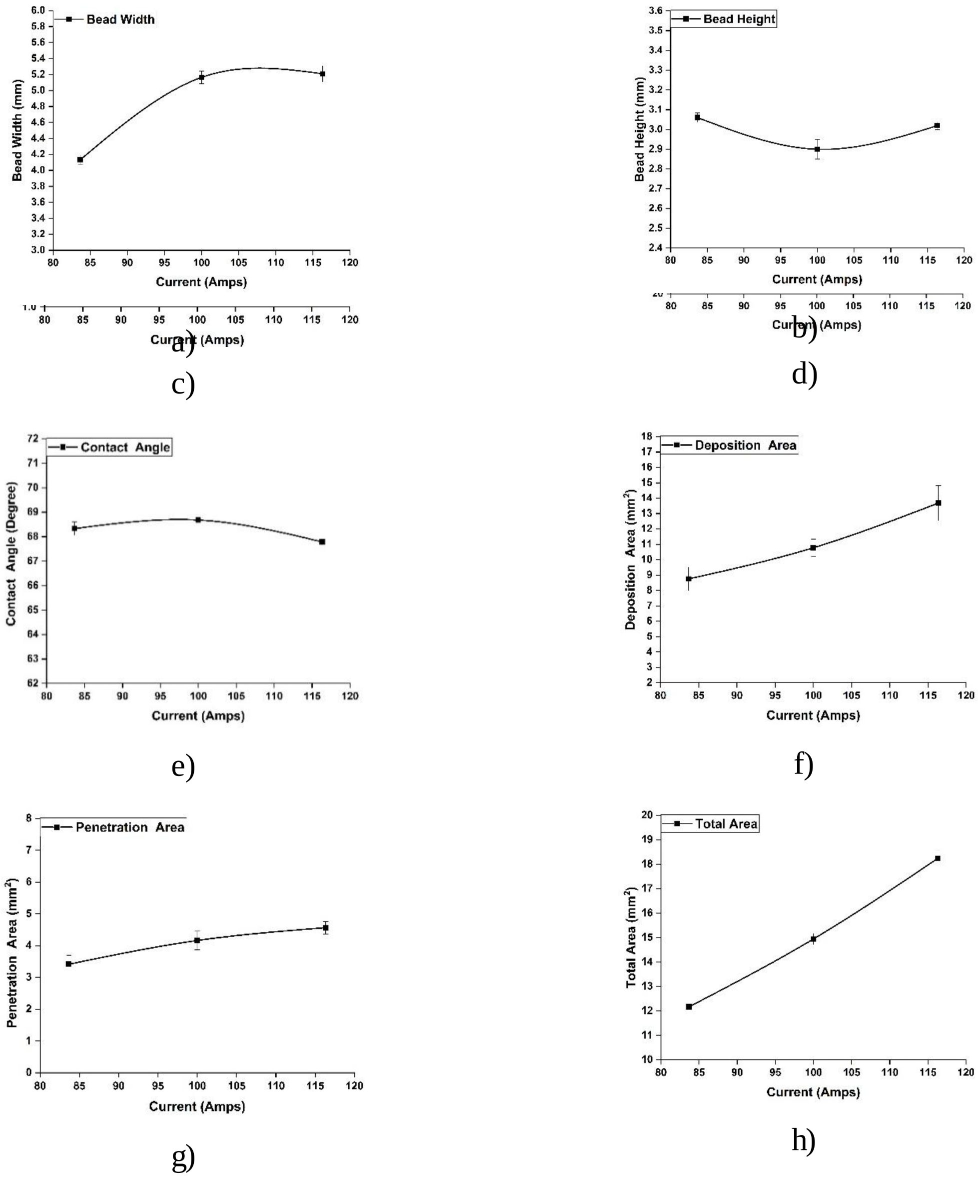

Figure 6.4 (a) - (h). It is evident from the plots that bead width, height, penetration deposition area, and penetration area, the total area decreases with welds peed and, dilution is in increases order. To study the weld speed behaviour, current and standoff distance are kept constant at 100 Amps, 5mm respectively while weld speed varied from 0.15 m/min to 0.45 m/min. The bead shape greatly depends on weld speed since material fusion, the formation of the droplet, and thermal cycle detachment happens in seconds.

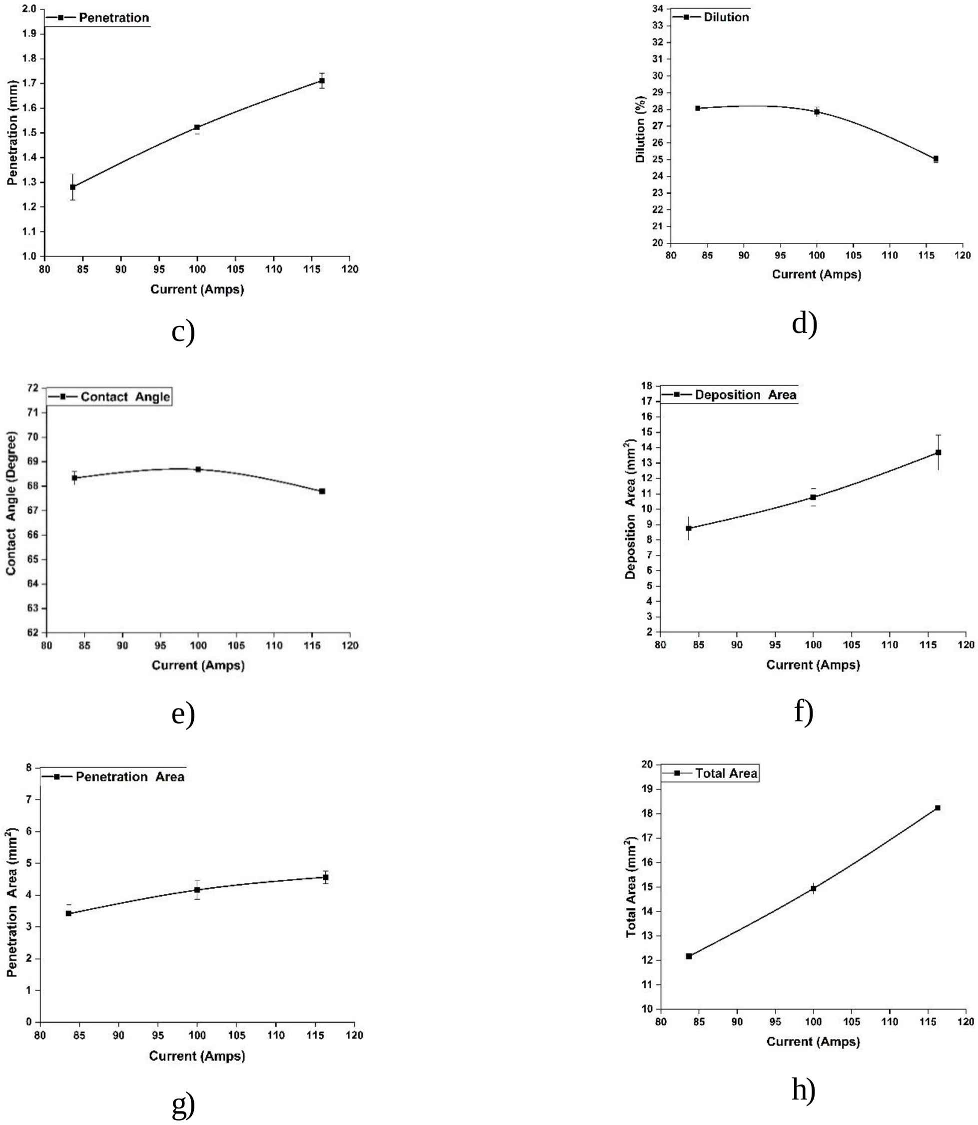

c)

d)

e)

f)

g)

h)

Figure 6.4 Effect of Current on a) Bead width b) Bead height c) Penetration d) Dilution e) Contact angle f) Deposited area g) Penetration area h) Total area

This occurrence depends on weld speed; hence, weld speed is desirable for deposition stability. When weld speed is low, it has more time to melt the material, and deposition whereas at high weld speeds it has less time for deposition as the bed moves fast in the deposition direction. Thus, bead height, penetration, deposition area, penetration area, total fusion area decreases with weld speed. From the results, it was observed that the effect of weld speed on the contact angle is insignificant since there is no variation in contact angle as it is almost constant at 67°.

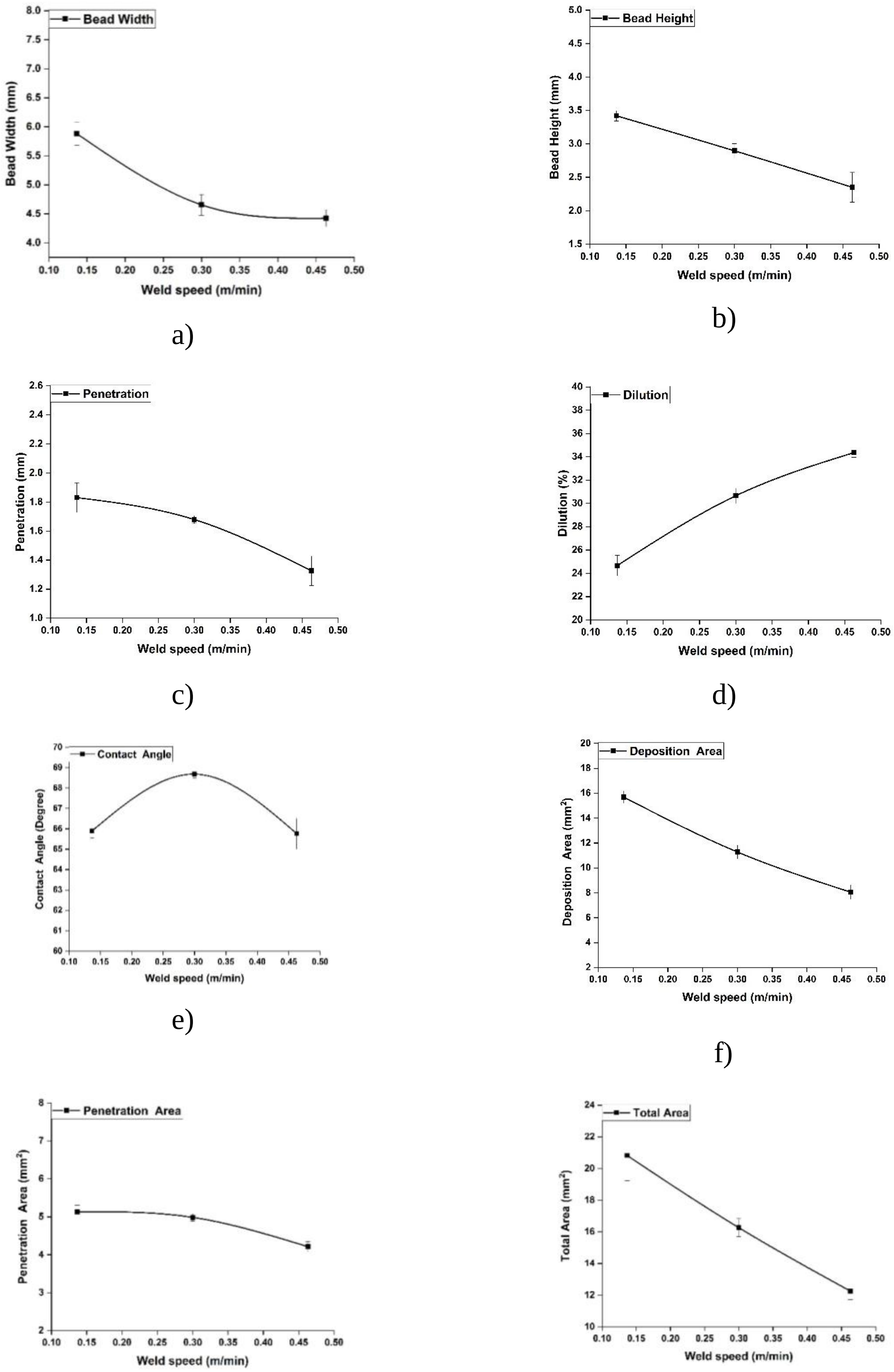

a)

b)

c)

d)

e)

f)

g)

h)

Figure 6.5 Effect of weld speed on a) Bead width b) Bead height c) Penetration d) Dilution e) Contact angle f) Deposited area g) Penetration area h) Total area

Figure 6.5 (a) - (h) shows the effect of weld speed on Inconel 625 single pass bead geometry. It is clear that the bead width, dilution, penetration area, and total area increases with standoff distance and, penetration, deposition area, bead height have either no effect or they are constant at 3mm, 1.6 mm, and 11mm^2 respectively. For the experimental study, current and weld speed is maintained at 100 Amps, and 0.3 m/min whereas standoff distance is varied from 3 mm to 7 mm. Standoff distance is the gap between the deposition surface and the delivery nozzle tip. The torch/nozzle would be away from the deposited surface at a high standoff distance. Hence, the arc force will be diminished and tend to spread out so that the bead width, dilution, deposition, and penetration area increase with standoff distance. The effect of standoff distance on penetration has no significance, and this might be due to the low range of standoff values. Also, as compared to the current and weld speed, the standoff distance has less effect on bead geometry.

6.3.2. Melting characteristics

6.3.2.1. Effect of deposition parameters on melting characteristics

The main intention of the welding process is to provide sufficient energy to soften the material to form the fusion area. Hence the experimentation process needs to adjust the process parameters to maximize the melting efficiency to reduce the HAZ and distortion effects. The electrode melting phenomenon influences bead shape, while plate melting behaviour affects the penetration and bonding related parameters. Hence, it is required to understand the melting and solidification behaviour of the deposition process. The efficiencies were calculated using Equations. (6.5)- (6.7). The welding process requires high melting efficiencies as the welding is a permanent joint, whereas, in the additive manufacturing process, the better bonding strength between the successive layers is expected.

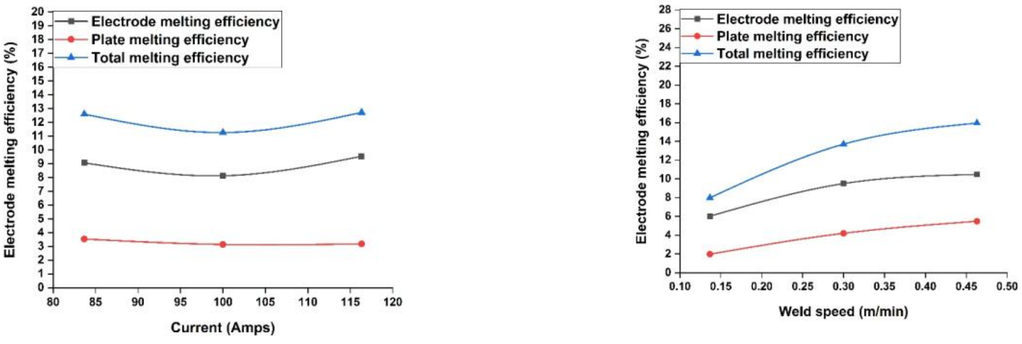

a)

b)

Figure 6.6 Effect of a) current and b) weld speed on melting characteristics

The electrode melting in terms of the melting of feeding wire depends much on the supplied heat input. The current, and weld speed indirectly affects the heat input thereby melting efficiencies also. Figure 6.6a shows the effect of current on plate melting efficiency, electrode melting efficiency, and total melting efficiencies. From the trends of the plots, it is observed that, concerning the current, the overall melting efficiency is 11%. The deposition melting efficiency and plate melting efficiency is stable at 8% and 3%. Since the CMT process uses very little heat input as compared to the conventional MIG process, the melting efficiencies will be below. The effect of weld speed on melting efficiencies is depicted in Figure 6.6 b. From the plot, it is noted that the average total melting efficiency is 12%. The quicker the heat source can move, the less time it takes to push heat away from the locally heated region and more efficiently it will melt [136]. It is clear from the plots that the melting efficiencies are almost stable for standoff distance since the standoff distance does not influence melting phenomena in the deposition process.

6.4 Chapter summary

Inconel 625 single-pass beads were deposited using a wire arc-based deposition process. The effect of process parameters on bead characteristics such as bead width, bead height, penetration, deposition area, and melting efficiencies are extensively investigated concerning heat input and solidification phenomena. The conclusion for the study are drawn below

- From the cooling curve, it is observed that the cooling time has a linear relationship with heat input and the cooling rate.
- Bead width, penetration, dilution, deposition area, penetration area, the total area increased with current whereas bead height and contact angle decreased with the current.
- Bead height, penetration, deposition area, penetration area, total fusion area decreases with weld speed, also observed that there is no considerable change in contact angle with process parameters.
- The welding speed contributes more to melting efficiency as compared to current and standoff stand.
- Standoff distance does not influence melting efficiencies since it has no direct or indirect impact on heat input.

Chapter 7

Effect of Heat Input on Mechanical and Microstructural Properties of Single-Pass Deposition of Inconel 625

In this chapter, the effect of heat input on single beads of Inconel 625 on mechanical and microstructure are studied. Seven heat input conditions were used to study the microstructure and mechanical characteristics. Microstructural characterization was done with optical and scanning electron microscopes while microhardness was measured using the Vickers microhardness testing method. It has been observed that the microstructure of the deposited beads consists of a columnar structure with primary dendrites. Also, intermetallic elements like Niobium (Nb), Molybdenum (Mo), and Laves were formed.

7.1 Introduction

Inconel 625 is a nickel-based superalloy with superior properties at an elevated temperature up to 1500°C with high strength, resistance to corrosion, fatigue strength, and thermal fatigue resistance and hence they are used in aerospace, chemical, petrochemical, marine, and other high-temperature applications.

Apart from high chromium content, superalloys are embedded with other alloying elements such as Molybdenum (Mo), Niobium (Nb), Iron (Fe), etc. and these elements contribute to the solid solution strengthening [100]. Even though many production methods are available for manufacturing Inconel 625, high production costs and complex structures have limited their commercial applications. Additive manufacturing (AM) can be a cost-effective alternate feasible production method for superalloys [74]. Wire arc deposition is an advancement in AM processes. The primary heat source to melt the materials is obtained from an electric arc which is developed due to the potential difference between the wire (feedstock) and the component being formed. In the present study, a cold metal transfer welding based WAAM method is used to deposit a single pass Inconel 625 beads at different heat input conditions.

The single-pass beads are used for repairing and remanufacturing the damaged components with less effort and at a low cost and can also be used for making permanent joints. The type of deposition strategy and heat energy sources influence the microstructure formations and thereby mechanical properties also. Some of the researchers investigated the processing of Inconel in laser assisted deposition [4-17], friction stir based solid state additive manufacturing process and very few were reported on welding based technologies [18-22].

Shuai studied the microstructural changes in selective laser melting (SLM) processed samples and observed elongated, columnar grains as fabricated samples while rectangular and equiaxed grains after heat treatment[61]. Huebner et al have studied the microstructure formations in Inconel 625 - WC metal matrix composite in laser cladding process with a weight percentage of 20 and 30 of WC. The authors observed precipitates of spherical oxide in both samples[62]. Leary et al. fabricated Inconel 625 lattice structures of 2 mm, 3mm, and

4 mm sizes at 2%, 4%, 6% strain rates using the Selective Laser Melting (SLM) process. It was observed that FCC with a 2 mm cell configuration has better specific strength and modulus than the other configuration lattice structures [63]. Marchese et al investigated the laser powder bed fusion processed (LPBF) Inconel 625 for microstructure and mechanical characterization. The samples had very fine dendritic structures with γ'' phases aged at 700 °C for 24 h[64]. Pleass used the SLM process to investigate the effect of powder particle sizes and flowability on process capability and observed that powder particles smaller than 10-µm diameter were responsible for the formation of agglomerations and make the process difficult[65]. Koutiri studied the porosity and fatigue behavior of Inconel 625 deposited by a selective laser melting process[66]. Gonzalez compared the microstructure of Inconel 625 processed through binder jetting process, laser powder bed fusion, and electron beam processes. Columnar grains are formed in EPBF and equiaxed grains are formed in binder jetting and LPBF. [67]. Hu used selective laser melting (SLM) to study the mechanical and microstructural behavior of laser welded Inconel 625 specimens. The tensile strength of the welded joint was found to be higher than the base material. The welded region consists of columnar grains whereas as-received SLM samples have equiaxed grains[68]. Dinda used a direct metal deposition method to fabricate Inconel 625 samples containing columnar dendrites. The columnar dendrites were found to follow the direction of the laser scan while deposition[69]. Abioye deposited Inconel 625 single track beads using a wire-based laser deposition process. The individual effects of process parameters on bead characteristics were investigated. A high quality surface was obtained at a low contact angle (<80◦), and 5% and 13% of dilution ratio[38]. Abioye studied laser cladded Inconel 625 coating to study the corrosion performance and found that the corrosion resistance of laser cladded Inconel is very close to that of the wrought Inconel 625 alloy. The authors observed columnar dendrites at the clad-substrate interface[70]. Marchese investigated heat treated Inconel 625 alloy samples in the laser powder bed fusion process. The anisotropy in the material was eliminated by the heat treatment. Equiaxed grains were formed at heat treatment conditions of 1080˚C and 1150˚C [71]. Zhong compared the solidification behavior of Inconel 718 and Inconel 625 and observed that the Inconel 625 has faster cooling rates than Inconel 718 due to stronger convection in the melt pool[72]. Rivera et al investigate the grain refinement and densification of Inconel 625 processed by the additive friction stir process. The EBSD results showed that fine grains of size 0.27 µm are formed at the interface regions [73].

Wang used the gas tungsten arc welding process to manufacture the Inconel 625 structure as an additive product and observed the microstructure at different locations of the deposited structure. Cellular grains were observed near the substrate, and columnar dendrites to equiaxed grains were observed while moving to the top region[74]. Sandeep et al. conducted experiments in the shielded metal arc welding process (SMAW) to study the fatigue and wear behaviour of Inconel 625 clad beads at 80 Amperes and 105 Amperes of welding currents. It was observed that the fatigue performance is higher for high weld current clads than the specimens with lower weld current processed samples[75]. Fesharaki compared laser cladding and TIG cladding process on microstructure of Ni-based Inconel 625 coatings. The microstructure observed at the coating surface was coaxial, columnar, and cellular dendrites, and with laser coating, a finer microstructure was formed [76]. Feng et al studied the microstructure of laser cladded Inconel 625 coating in shielded metal arc welding (SMAW) process and found that the coatings had a finer microstructure as compared with arc welded samples[77]. Rajani investigated the microstructure of Inconel 625 in explosive forming by varying the process parameters and found that at low impact energies linear interfacial structures are formed whereas at high impact energies wavy interfaces are formed[78]. Yangfan investigated the microstructure of Inconel 625 deposited by the CMT process. Microstructural examinations revealed that cellular grains are formed near to the substrate, columnar dendrite at the middle portion of the structure, and dendrites with secondary arms at the top portion of the deposit[79].

7.1.1. Scope of work

From the reported literature, it is observed that very few studies have been performed on the study of heat input effects on deposition characteristics in the cold metal transfer process. In the present investigation, the microstructures and mechanical properties of single bead deposition of Inconel 625 have been studied at seven heat input conditions by varying the process parameters.

7.2 Experimental Methods

Experiments were conducted on Fronius made manual CMT machine attached with a 3 axis manual controlled workstation. The deposition torch was held stationary in a vertical position through which filler wire feeding was done at a fixed angle. The table bed can be moved in three axes. Shielding gas has an equal proportion of Argon and CO2 gas to reduce atmospheric effects.

Inconel 625 filler wire of 1.2 mm diameter which is commercially available in industrial markets is used for deposition. The Inconel beads are deposition on a mild steel plate of size 250 x 250 x 10 mm size. Before cladding, mild steel plates were sandblasted over the surface and cleaned to avoid contamination. During the experiments, different combinations of heat inputs can be set by varying the current, voltage, and weld speed. CMT controller has inbuilt synergic characteristics which can provide automatic control of voltage whenever the current cycle changes. Hence, to obtain different heat input conditions, current and weld speed were varied in the specified ranges. Considering 85% of machine efficiency, the heat input can be calculated by using

$$HI = \frac{60 * A * V}{1000 * S} * 0.85 \qquad (7.1)$$

The cladding process is carefully controlled and deposited on the substrate such that deposited beads have good geometry without pores, blowholes, and other processing defects. The details of the deposition parameters are given in Table 7.1. The grain formation and related characteristics are observed from the fusion region perpendicular to the deposition direction. The machined samples were polished with 800 to 2000 grit size emery papers and later with velvet cloth and aluminum oxide slurry for a mirror finish. To reveal the microstructure, the samples were etched with 10 ml of HNO_3, 15 ml of HCl, and 10 ml of Acetic acid. The microstructure formations were observed using a QX 4RT DIC polarizer optical microscope (OM), and Tescan Vega 3 LMU scanning electron microscope (SEM) with inbuilt Energy Dispersive X-Ray analysis (EDAX). Micro-hardness was measured using a Schimadzu HMV Vickers micro-hardness testing machine at a load of 500 grams.

Table 7.1 Heat inputs conditions

Sample No	Current (A, Amps)	Voltage (V, Volts)	Weld speed (S, mm/s)	Heat Input (J/mm)
1	100.00	18.10	0.46	199.24
2	090.00	17.80	0.40	204.26
3	110.00	18.50	0.40	259.46
4	100.00	18.10	0.30	307.70
5	090.00	17.80	0.20	408.51
6	110.00	18.50	0.20	518.93
7	100.00	18.10	0.14	675.27

7.3 Results and Discussions

Inconel 625 single bead clads were successfully deposited on a mild steel substrate plate as per the heat input conditions using a cold metal transfer deposition process as shown in

Figure 7.1. As the starting and end portions of the clad were irregular and not uniform, only the middle portion of the bead was considered for analysis and characterization.

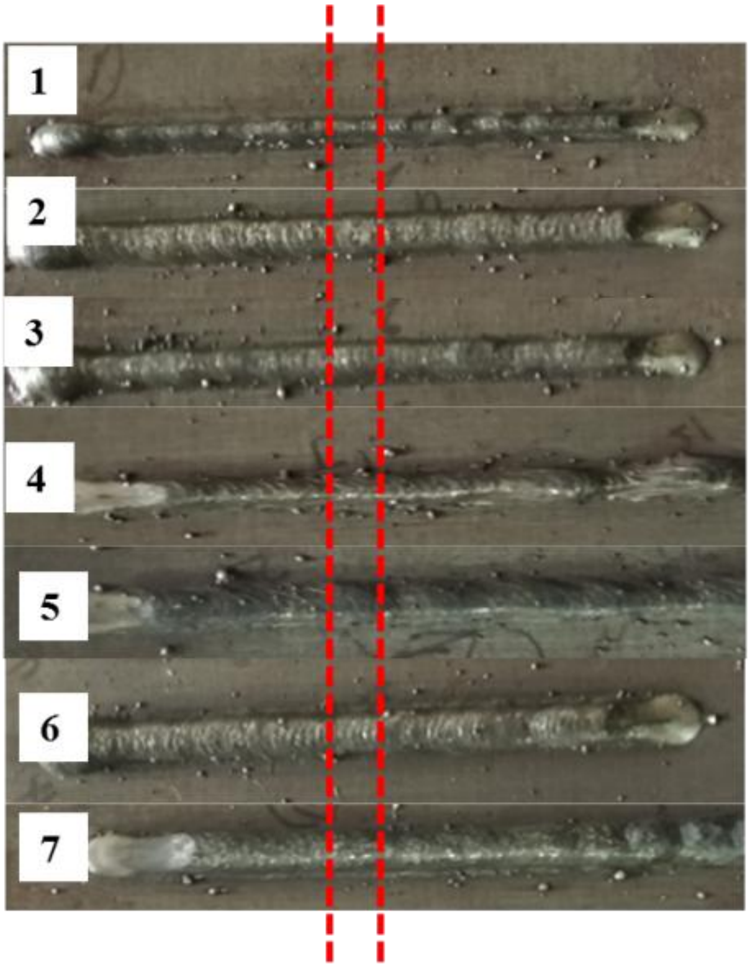

Figure 7.1 Inconel 625 beads deposited on the mild steel substrate plate

7.3.1. Microstructure characterization

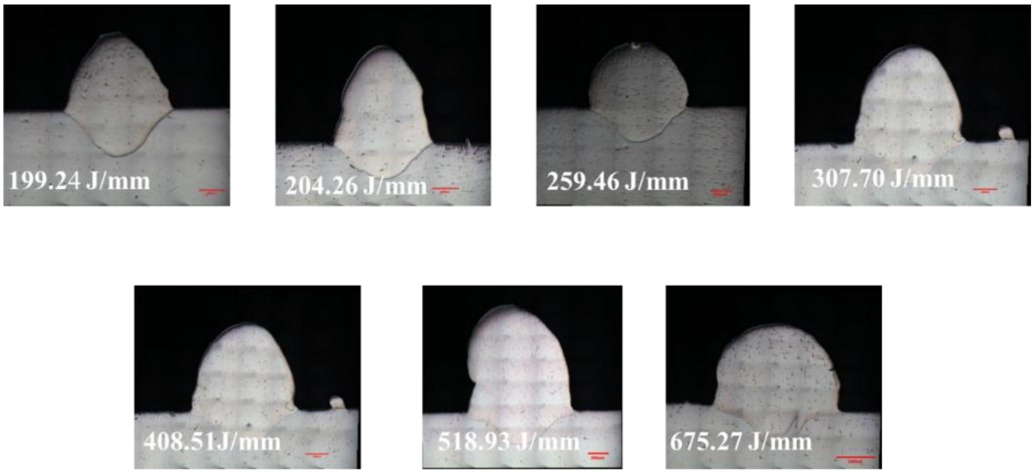

Figure 7.2 Macrographs of deposition beads at different heat input conditions

The macrographs of Inconel 625 deposition beads at different heat input conditions are shown in Figure 7.2. The macro images are observed in a 3D microscope on a 1000 micron scale. It is observed from the visual inspection that all the bead surfaces are free from manufacturing defects like pores, inclusions, voids, cracks, etc. The deposited beads were found to be well diluted in the mild steel substrate. At the interfacial layer between mild steel and Inconel, no delamination effects were witnessed on the surface.

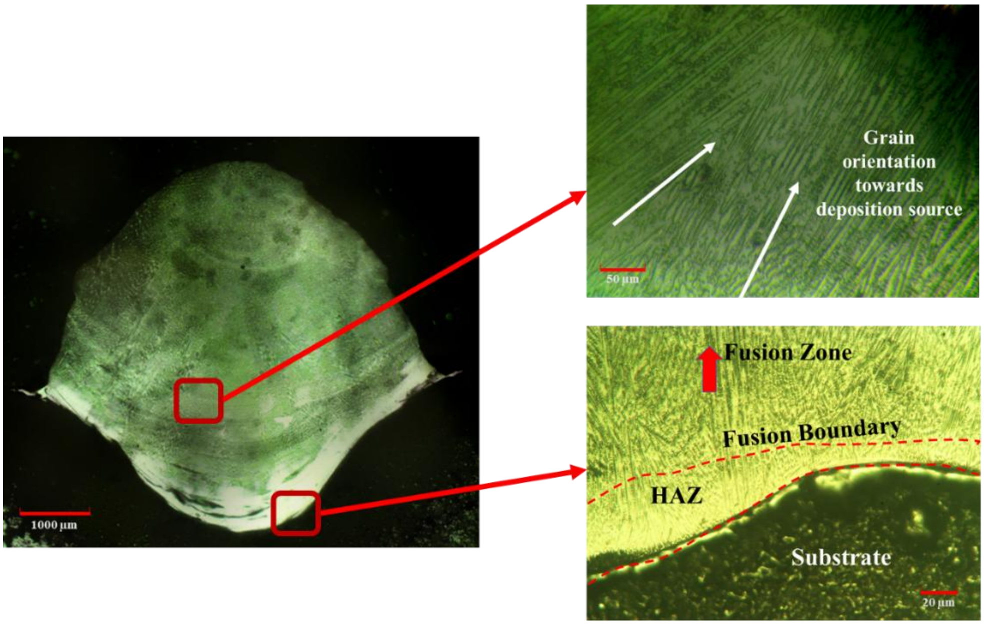

Figure 7.3 Microscopic image of CMT deposited single bead with cross-sectional microstructure (Sample 7)

Figure 7.3 depicts the microscopic image of the CMT deposited single bead structure for sample number 7. The substrate on which deposition occurs is dark in color. Since the substrate is mild steel and deposited material is Inconel 625, while etching with Glycergia solution, the mild steel substrate was over etched whereas for Inconel etching was slow with the solution. By the time Inconel was etched, mild steel becomes black because of over etching. Hence, the boundary is visible as an interfacial boundary between the substrate and deposition bead. Above the interfacial boundary, heat affected zone was formed in which all the grains are overlapped and formed a solid like structure. Above the HAZ, a boundary called fusion line or fusion boundary was observed from which a noticeable microstructure is observed. On the top of the fusion boundary, the fusion zone can be observed. In the fusion zone, the deposited material is completely melted and forms a visible microstructure concerning the temperature gradients. It is also observed from the deposition microstructure that, all the grains are oriented towards the nozzle direction because heat dissipation happened in the direction of deposition.

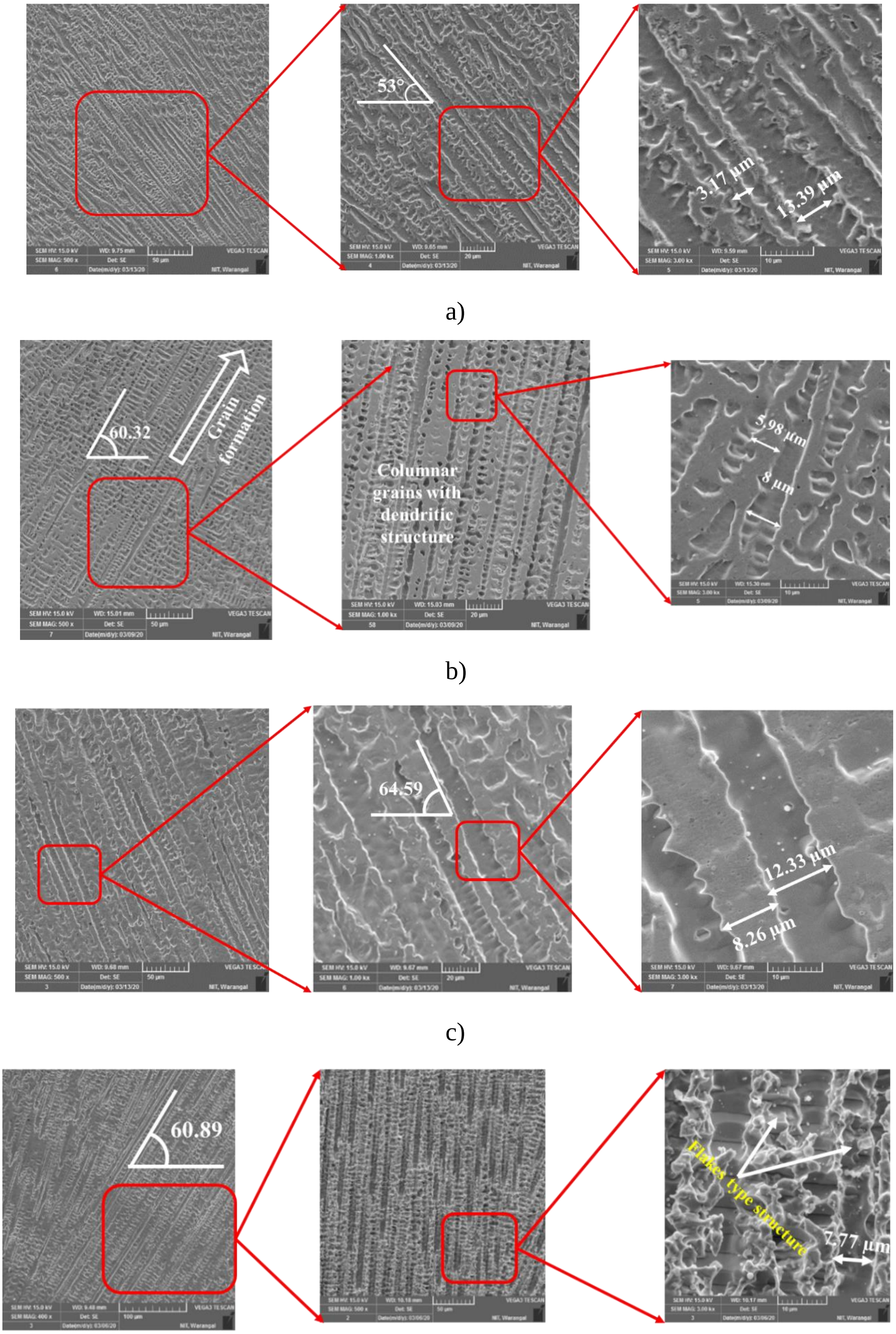
53°
3.17 µm
13.39 µm
60.32
Grain formation
Columnar grains with dendritic structure
5.98 µm
8 µm
64.59
12.33 µm
8.26 µm
60.89
Flakes type structure
7.77 µm

a)

b)

c)

d)

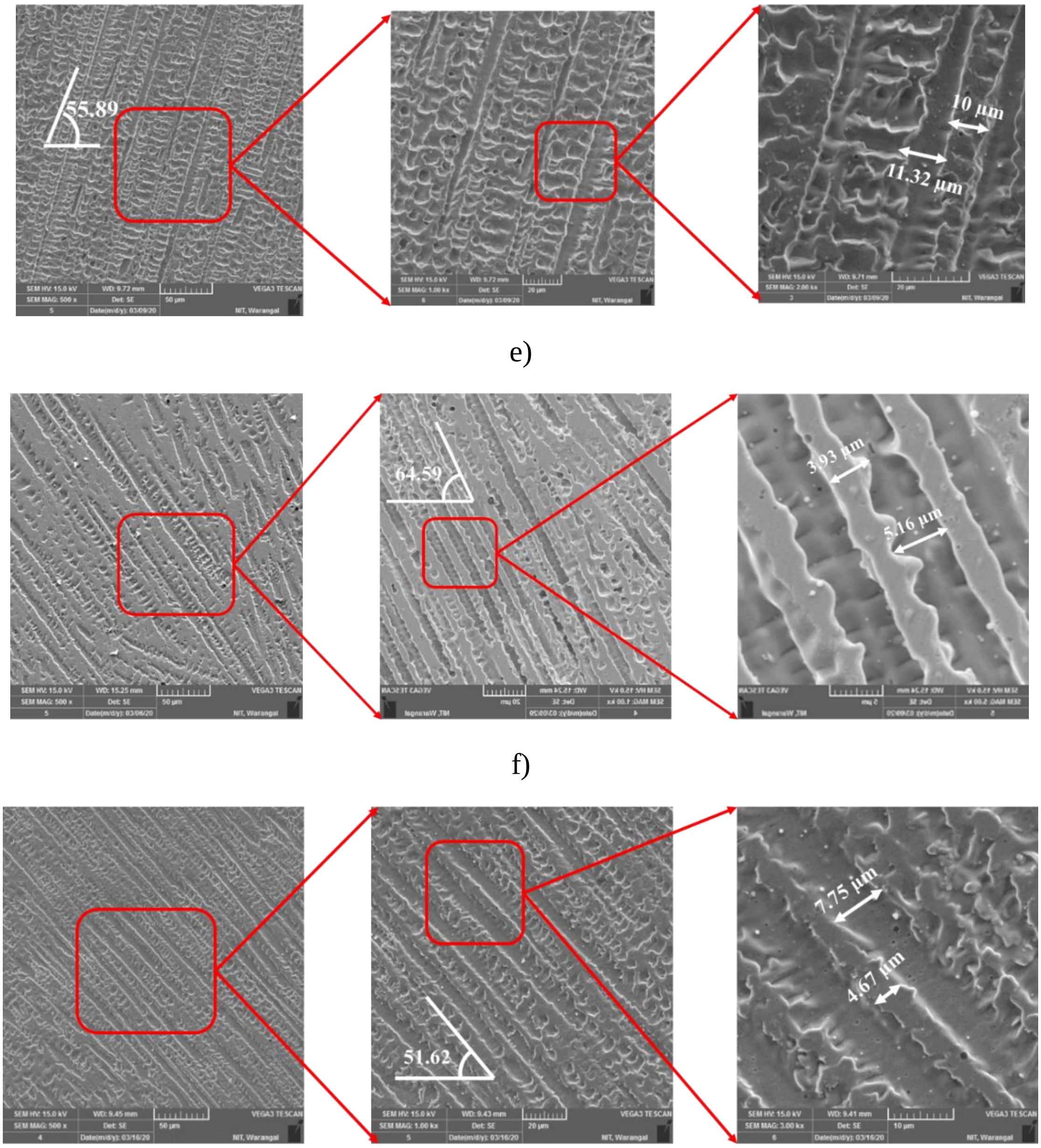

e)

f)

g)

Figure 7.4 SEM images of Inconel 625 deposition beads at a) Sample 1 b) Sample 2 c) Sample3 d) Sample 4 e) Sample 5 f) Sample 6 g) Sample 7

Figure 7.4 a) to g) shows the SEM images of Inconel 625 deposition beads at seven heat input conditions. Columnar grains with the primary dendritic structure are observed. All the columnar grains are pointed towards the direction of material deposition. The angle of grain formation concerning the deposition axis varies from 51° to 64°. Some portions of the deposition structure have a flaky structure which is shown in Figure 7.4 d. The columnar grains are evolved with a size of 3-10 µm. The space between the grains called interdendritic space has a distance of 5-13 µm. The heat flux direction mainly determines the grain growth direction which depends on the way heat flux is distributed in the solid-liquid interface. It has been observed in Figure 7.4 that the grains are grown randomly and have an oblique angle with the substrate and not in an exact perpendicular direction. During solidification, the grain formation and orientation follow the maximum temperature gradient which is random. That is why the grains are not perpendicular to the substrate. The structural growth is perpendicular only when the deposited material is cooled entirely through the substrate.[138]. The rate of cooling and accumulated heat transfer during the deposition significantly affects the microstructural variations[139].

However, heat propagates more through the substrate regions where more heat is absorbed and it travels faster through the surroundings where contact surfaces and atmosphere are found. This cooling effect has brought out a fine, cellular structure in these regions. The lack of equiaxed crystals may be due to faster cooling rates. In the rapid cooling process, the atoms have less time to distribute and solidify instantly thereby forming a columnar grain structure[140]. However, compared with that of the cast part, a wire arc additively manufactured component is relatively fine and thereby exhibiting better properties [26 -27]. Contradictory to the single deposition process, in a multi-deposition process, the cooling process takes place through the substrate into already deposited layers. Since each layer is deposited perpendicular to the successive layers, the occurrence of cooling is random in all directions. Therefore, the grain growth is strongly inclined in the perpendicular direction. Table 7.2 shows the microstructure of Inconel 625 processed in different conditions.

Table 7.2 Mechanical properties of various Ni-based superalloys using different WAAM processes[111].

Author	**Materials**	**Process Condition**	**Microstructure**	**YS [MPa]**	**UTS [MPa]**	**EL [%]**
Baufeld.	IN 718	GMAW	Nb precipitates + dendritic structure	473 ± 6	828 ± 8	28 ± 2
ASM	IN 625	Cast		350	710	48
ASM	IN 625	Wrought		490	855	50
Xu et al.	IN 625	Pulsed plasma arc deposition	Laves phase + columnar dendritestructure	438± 38	721 ± 32	48.6
Xu et al.	IN 625	Pulsed plasma arc deposition	Laves phase + MC carbides +δ-Ni3Nb	449	726	43
Wang et al.	IN 625	GTAW	Coarser Laves particles + Nb precipitates	469	802	42
D.T. Sarathchandra et al	IN625	CMT (Present work)	Columnar structure with primary dendrites, Nb and Mo precipitates	-	-	-

7.3.2. Elemental composition analysis

Energy Dispersive X-Ray analysis (EDAX) has been done to reveal the elementary contributions of the precipitates. The microstructural characteristics like grain structure and shape (equi axis, columnar or dendritic formations), solid solution strengthening elements present in the alloying element, and intermetallics or precipitation phases prominently influence the material properties. The phases and intermetallic compounds are identified using EDAX analysis. The solidification of nickel-based alloys predominantly results in directionally crystallized dendritic structure. Moreover, chemical segregation occurs during solidification and the chemical composition of the dendritic cells varies from the interdendritic spaces, and hence interdendritic and other phases may evolve[141]. The Nickel-based alloys are strengthened by carbide precipitation such as MC, M_6C, etc which are formed due to precipitation of Ni, Nb, and Mo, and $M_{23}C_6$ due to the presence of chromium. During phase transformation, elements such as Mo, Nb, C, and Si are likely to segregate. During the solidification process, the molten metal gets enriched with the alloying constituents. After the solidification process, the elements remain in the interdendritic spaces and their concentration increases than the base alloy. Hence, in the interdendritic spacing, intermetallic phases can form. The alloys comprising of Molybdenum, Niobium, and Carbon will have intermetallic formations. Hence, in the interdendritic spaces, NbC, or other carbides as well as the Ni_3Nb phase can be formed [29]. The main elements considered for the study are Nickel (Ni), Chromium (Cr), Iron (Fe), Niobium (Nb), Molybdenum (Mo), and Titanium (Ti).

Figure 7.5 shows the elemental composition analysis performed at different heat input conditions. For all the samples, Ni has a rich composition followed by Fe, Cr, Mo, Nb, and Ti.

HI 1

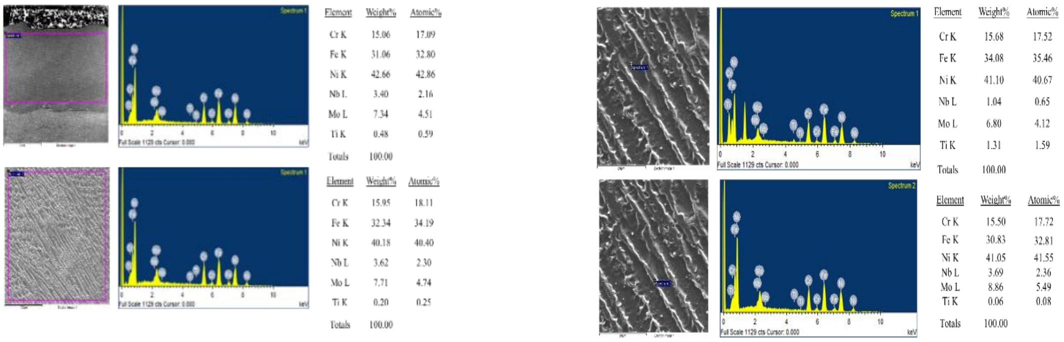

Element	Weight%	Atomic%
Cr K	15.06	17.09
Fe K	31.06	32.80
Ni K	42.66	42.86
Nb L	3.40	2.16
Mo L	7.34	4.51
Ti K	0.48	0.59
Totals	100.00	

Element	Weight%	Atomic%
Cr K	15.95	18.11
Fe K	32.34	34.19
Ni K	40.18	40.40
Nb L	3.62	2.30
Mo L	7.71	4.74
Ti K	0.20	0.25
Totals	100.00	

Element	Weight%	Atomic%
Cr K	15.68	17.52
Fe K	34.08	35.46
Ni K	41.10	40.67
Nb L	1.04	0.65
Mo L	6.80	4.12
Ti K	1.31	1.59
Totals	100.00	

Element	Weight%	Atomic%
Cr K	15.50	17.72
Fe K	30.83	32.81
Ni K	41.05	41.55
Nb L	3.69	2.36
Mo L	8.86	5.49
Ti K	0.06	0.08
Totals	100.00	

HI 2

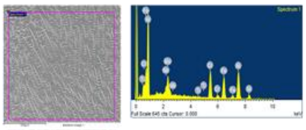

Element	Weight%	Atomic%
Cr K	17.56	20.13
Fe K	21.47	22.92
Ni K	48.47	49.21
Nb L	4.01	2.57
Mo L	8.65	5.37
Ti K	-0.17	-0.21
Totals	100.00	

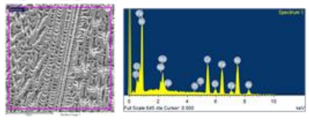

Element	Weight%	Atomic%
Cr K	17.58	20.07
Fe K	22.73	24.16
Ni K	47.81	48.32
Nb L	4.24	2.71
Mo L	7.61	4.70
Ti K	0.03	0.03
Totals	100.00	

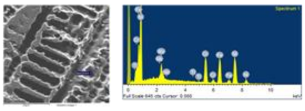

Element	Weight%	Atomic%
Cr K	17.00	19.23
Fe K	25.68	27.04
Ni K	47.60	47.68
Nb L	2.01	1.27
Mo L	7.62	4.67
Ti K	0.08	0.10
Totals	100.00	

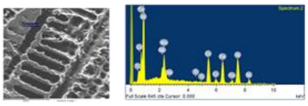

Element	Weight%	Atomic%
Cr K	17.02	19.78
Fe K	21.63	23.41
Ni K	45.03	46.35
Nb L	5.68	3.69
Mo L	10.53	6.63
Ti K	0.12	0.15
Totals	100.00	

HI 3

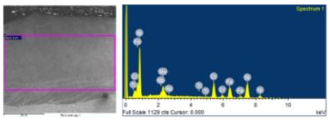

Element	Weight%	Atomic%
Cr K	17.38	19.83
Fe K	20.70	22.00
Ni K	49.89	50.43
Nb L	3.32	2.12
Mo L	8.33	5.15
Ti K	0.38	0.47
Totals	100.00	

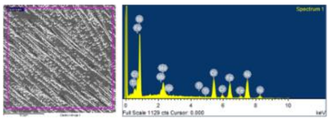

Element	Weight%	Atomic%
Cr K	18.78	21.56
Fe K	19.63	20.99
Ni K	47.61	48.42
Nb L	4.10	2.64
Mo L	9.49	5.91
Ti K	0.40	0.49
Totals	100.00	

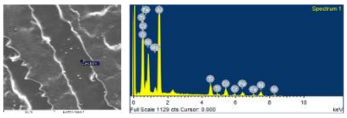

Element	Weight%	Atomic%
Cr K	5.90	2.63
Fe K	5.35	2.22
Ni K	9.48	3.74
Ti K	7.26	3.51
Totals	100.00	

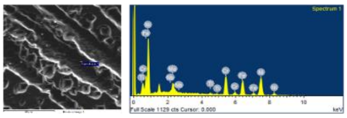

Element	Weight%	Atomic%
Cr K	18.51	20.91
Fe K	21.84	22.96
Ni K	49.35	49.35
Nb L	1.96	1.24
Mo L	7.62	4.66
Ti K	0.72	0.88
Totals	100.00	

HI 4

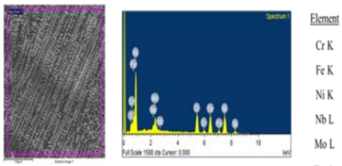

Element	Weight%	Atomic%
Cr K	16.99	18.49
Fe K	25.18	25.52
Ni K	44.49	42.89
Nb L	3.64	2.22
Mo L	7.95	4.69
Totals	100.00	

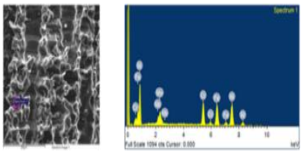

Element	Weight%	Atomic%
Cr K	17.89	20.17
Fe K	25.91	27.19
Ni K	47.11	47.02
Nb L	3.49	2.20
Mo L	5.59	3.41
Totals	100.00	

HI 5

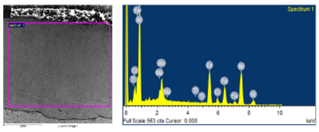

Element	Weight%	Atomic%
Cr K	19.38	22.37
Fe K	14.57	15.66
Ni K	51.75	52.90
Nb L	4.73	3.06
Mo L	9.51	5.95
Ti K	0.05	0.06
Totals	100.00	

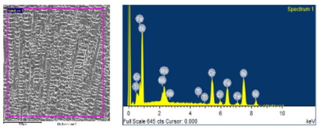

Element	Weight%	Atomic%
Cr K	18.45	21.13
Fe K	17.95	19.13
Ni K	51.19	51.90
Nb L	4.26	2.73
Mo L	8.08	5.01
Ti K	0.08	0.10
Totals	100.00	

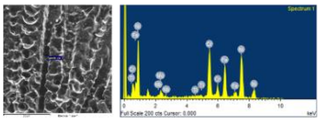

Element	Weight%	Atomic%
Cr K	21.23	23.33
Fe K	22.44	22.96
Ni K	53.31	51.90
Nb L	0.84	0.51
Mo L	2.20	1.31
Totals	100.00	

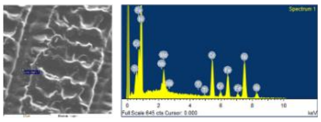

Element	Weight%	Atomic%
Cr K	18.32	20.92
Fe K	17.65	18.77
Ni K	52.04	52.64
Nb L	3.33	2.13
Mo L	8.35	5.17
Ti K	0.31	0.38
Totals	100.00	

HI 6

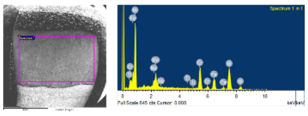

Element	Weight%	Atomic%
Cr K	19.11	21.99
Fe K	14.92	15.98
Ni K	51.98	52.96
Nb L	5.07	3.26
Mo L	8.55	5.33
Ti K	0.38	0.48
Totals	100.00	

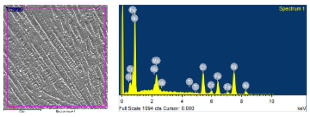

Element	Weight%	Atomic%
Cr K	18.33	21.09
Fe K	15.99	17.12
Ni K	52.25	53.23
Nb L	3.77	2.43
Mo L	9.48	5.91
Ti K	0.18	0.23
Totals	100.00	

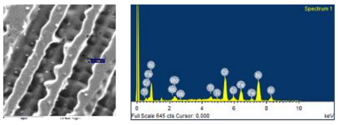

Element	Weight%	Atomic%
Cr K	22.38	24.62
Fe K	15.72	16.10
Ni K	56.67	55.21
Nb L	0.85	0.52
Mo L	2.83	1.69
Ti K	1.56	1.86
Totals	100.00	

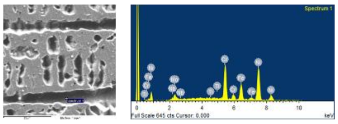

Element	Weight%	Atomic%
Cr K	22.92	25.25
Fe K	15.49	15.88
Ni K	58.56	57.12
Nb L	0.82	0.50
Mo L	2.34	1.39
Totals	100.00	

HI 7

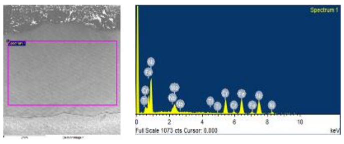

Element	Weight%	Atomic%
Cr K	16.09	18.37
Fe K	27.41	29.14
Ni K	44.13	44.62
Nb L	4.66	2.98
Mo L	7.52	4.65
Ti K	0.20	0.24
Totals	100.00	

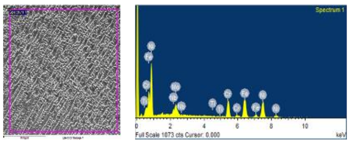

Element	Weight%	Atomic%
Cr K	16.28	18.52
Fe K	30.02	31.81
Ni K	42.17	42.50
Nb L	4.08	2.60
Mo L	7.49	4.62
Totals	100.00	

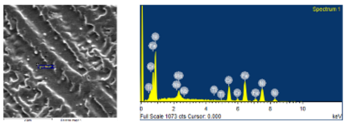

Element	Weight%	Atomic%
Cr K	15.97	17.84
Fe K	34.82	36.22
Ni K	41.73	41.29
Nb L	0.99	0.62
Mo L	6.30	3.82
Ti K	0.18	0.21
Totals	100.00	

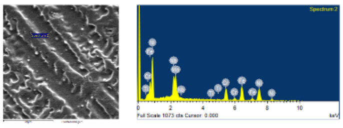

Element	Weight%	Atomic%
Cr K	13.03	15.94
Fe K	24.49	27.91
Ni K	34.03	36.88
Nb L	16.66	11.41
Mo L	11.73	7.78
Ti K	0.06	0.08
Totals	100.00	

Figure 7.5 EDAX analysis report

Table 7.3 Summary of composition analysis

Heat Input(J/mm)	Ni K	Cr K	Fe K	Nb L	Mo L	Ti K
199.24	41.42	15.505	31.7	3.51	7.525	0.34
240.30	48.14	17.57	22.1	4.125	8.13	0.015
259.46	48.75	18.08	20.165	3.71	8.91	0.39
362.00	45.8	17.44	25.545	3.565	6.77	0.38
408.51	51.47	18.915	16.26	4.495	8.795	0.065
518.93	52.115	18.72	15.455	4.42	9.015	0.28
675.27	43.15	16.185	28.715	4.37	7.505	0.1

Figure 7.5 a shows the elemental analysis of the longitudinal cross-section area of the fabricated samples, and

Figure 7.5 b shows the elemental analysis of the precipitation region at higher magnification in which Laves phases and intermetallics are observed. Table 7.3 shows the summary of the composition analysis for the elements considered for the study. Average values were considered for the study. Since Inconel is a nickel based alloy, all the samples have Ni as the primary element in the composition analysis. It is also observed that the percentage of Nb and Mo increased with an increase in heat input. From

Figure 7.5 b, it is evident that Nb and Mo are present as precipitates and form intermetallic Laves phases of Nb, Mo which enhances the brittleness to the base material. This happens because, in the process of precipitation Nb, Mo gets consumed and segregates into the base material[142]. Hence, after solidification large dimple structures are formed due to coarse grains and the segregation of the alloying elements[63]. The same has been observed in

Figure 7.5 b.

7.3.3. Microhardness analysis

The micro-hardness of any processed sample significantly influences the mechanical properties of the entire sample. Hence, the microhardness values are measured with Schimadzu HMV Vickers micro-hardness tester with 500 grams load. The observed points are at a distance of 1 mm from the substrate. Likewise, 4 readings were considered and the average of all the readings is reported in Table 7.4.

Figure 7.6 a shows the microhardness plots of single bead deposition samples. It is clear from the plot that the fusion zone has the maximum hardness. Since the region near the outer surface will be exposed to the external atmosphere, the hardness increases due to carbide formation. Figure 7.6 b shows the average microhardness values of all heat input conditions. From the plot, it is evident that the microhardness increase with heat input. The maximum hardness of 234.7 HV was observed for heat input condition 7. At high heat inputs, the grains are fine and hence the hardness is high.

Table 7.4 Summary of microhardness data of Inconel 625 deposition beads (in HV)

Distance from the substrate, mm	Sample 1	Sample 2	Sample 3	Sample 4	Sample 5	Sample 6	Sample 7
-2	184	184	184	184	184	184	184
-1	185	185	185	185	185	185	185
1	206.60	209	218.00	228.50	222.20	229.90	231.00
2	208.00	211	215.50	225.70	222.20	232.90	242.80
3	201.90	212	216.00	216.10	233.60	228.50	229.20
4	202.30	210	219.00	218.80	228.90	231.40	235.90
Average	204.70	210.50	217.13	222.28	226.73	230.68	234.73

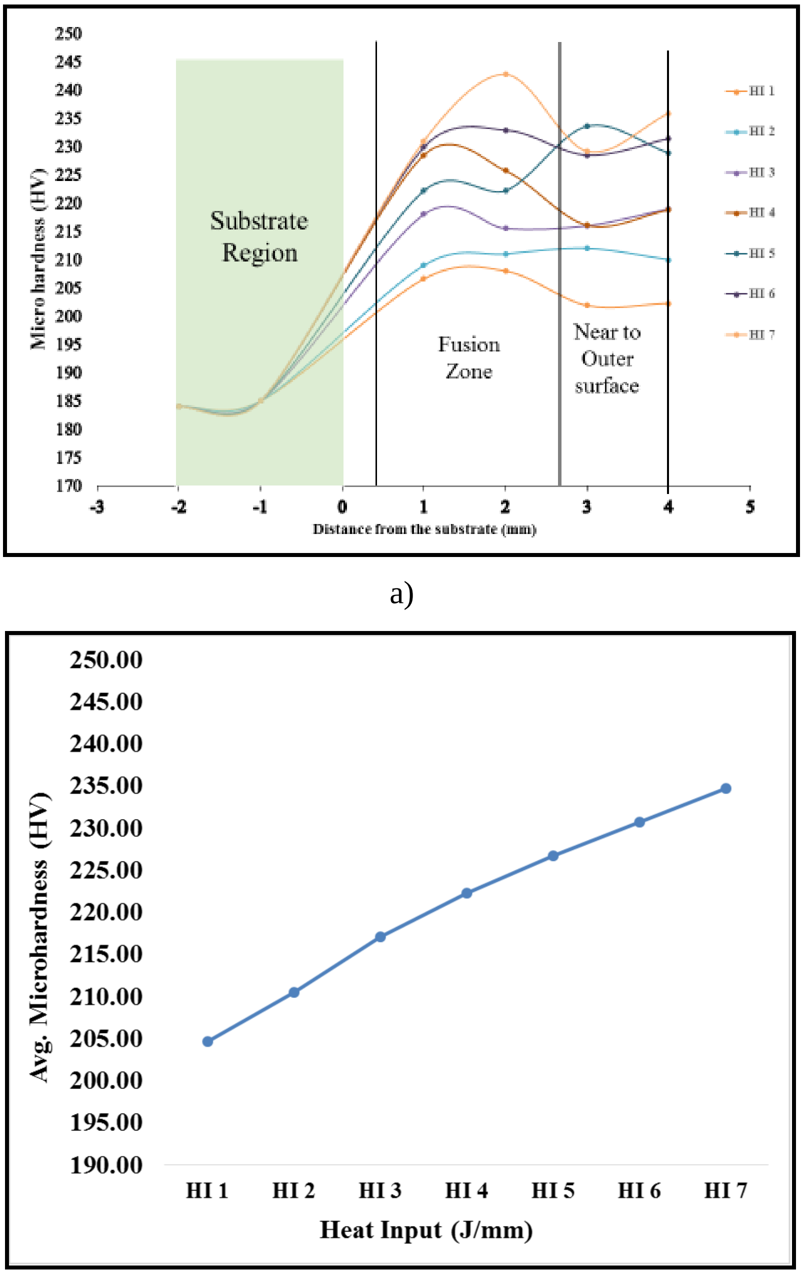

a)

b)

Figure 7.6 Microhardness profiles a) at all heat input conditions b) Average microhardness

7.4 Chapter summary

In the present study, single beads of Inconel 625 were deposited at different heat input conditions on the mild steel substrate using a wire arc based cold metal transfer process. The mechanical and metallurgical characteristics of the deposits were evaluated. The key findings are given below:

- Inconel 625 single beads were successfully deposited with varying heat input conditions. The heat input is attained by changing the travel speed of the torch during the deposition process. The deposited tracks were found to be free of crack and porosity and had good metallurgical bonding with the substrate.

- The obtained microstructure in all the samples was found to exhibit columnar dendritic structure and sometimes with primary dendrites. The columnar dendrite growth direction is mostly perpendicular to the substrate. The grains were sloping in the range of 51° to 64°. The columnar grains have a size of 3-10 µm. The interdendritic space has a distance of 5-13 µm. Also, fine grains are observed with an increase in heat input.
- During the solidification, the samples were enriched in Ni followed by Fe, Cr, Mo, Nb, and Ti. The elemental composition of Nb and Mo increases with heat input. Nb and Mo precipitates were formed in the form of the Laves phase.
- The fusion zone was found to have maximum hardness compared to other regions of the samples. Also, it was observed that the microhardness increases with an increase in the heat input. A maximum hardness of 234.7 HV was observed for heat input condition 7.

Chapter 8

Compression, wear, corrosion, and microstructure studies of dissimilar deposition of Inconel 625 on SS 304 processed wire additive manufacturing

This chapter presents the mechanical, wear, and corrosion properties of the Inconel 625 deposition and dissimilar deposition of Inconel 625 on Stainless steel 304. From the data obtained from the optimized parameters in the previous chapters, a block of 150 mm x 75mm x 75 mm is made with a multipass multi-track deposition strategy. Wear, compression, and corrosion samples were extracted from the blocks, and samples were prepared as per ASTM standards to test the wear and corrosion resistance of Inconel 625, and dissimilar deposition of SS 304 and Inconel 625.

8.1. Introduction

Wire-based additive manufacturing is an intriguing option for broadening the range of applications. For this objective, highly developed welding techniques can be employed. There are several materials to choose from, and the majority of them have been defined and described for use in conventional welding procedures. Synergy effects can be used, e.g. in quality control. Arc-, laser-, and electron-beam additive manufacturing are the three major types of wire-based additive manufacturing. The basic concept is to create near net form parts in a cost-effective manner, with just a few subtractive manufacturing stages required to obtain the final geometry[143]. The metallic deposition is important for improving the surface characteristics and repairing metallic components that function in corrosive, fatigue-prone, wear-leading, and high-temperature environments. Such an unfavorable working environment frequently leads to component failure. [95]. For producing completely dense metal structures, laser metal-wire deposition (LMWD) is a promising and prospective approach. LMWD features lower dilution, a quicker forming rate, and better material usage than laser metal-powder deposition (LMPD). Furthermore, the structures deposited by LMwD have exceptional internal stability and mechanical performance, which satisfies the demands of industrial industries for high quality and efficiency. Process factors such as laser power, scanning speed, wire feeding speed, overlapping rate, and height increment should all be properly controlled during laser depositing to provide a stable and reproducible process. [94]. Multiple layers can be used to obtain the desired deposition thickness, as well as to add additional features to improve the component's functioning. The laser is used to create a molten pool consisting of both the melted feedstock and a tiny amount of the substrate material during the deposition of each layer. As the laser passes through the component, the molten material rapidly solidifies and cools, creating significant temperature gradients in the part that can lead to the creation of high amounts of residual stress and deformation. The component deformation that occurs during cladding is quite similar to that which occurs during welding. Welding-induced distortion is difficult to understand since it is caused by three in-plane and three out-of-plane distortion types. Welding distortion and residual stress generation have been widely explored utilizing finite element modeling and experimental investigations because of their complexity. Cladding is comparable to welding, but it differs because of the high number of passes, the amount of material deposited, and the absence of a unique joint shape [144].

Wen et al worked on numerical modeling of multitrack direct laser deposition processes by employing the physical models of mass addition, fluid motion, and solidification phenomena. The numerical models have predicted the deposition characteristics such as melt pool behaviour, heat-affected zones, etc. The same has been confirmed with the experimental analysis[145]. Mazzucato et al. studied the effect of building parameters and scanning strategy to obtain the optimum melt pool shape and better mechanical properties of the deposited samples [146]. Criales et al. offer an integrated physics-based and statistical modeling technique for predicting temperature field and melt pool shape in multi-track processing of nickel 625 alloys in laser powder bed fusion (L-PBF). Statistics based prediction models for relative density, melt pool shape, peak temperature, and duration above melting point are constructed using response surface regression, and multi-objective optimization studies are carried out utilizing genetic algorithms and swarm intelligence[147]. Ghorbel et al studied the longitudinal shrinkage and angular distortion caused by the multipass welding process. Tensile and bending tests were then done to ensure the welded plate's reliability. The mechanical tensile strength of the welded junction is greater than that of the parent metal[148]. Zareh et al investigated the variable overlap bead deposition characteristics in the direct energy deposition process. One-bead, two-bead, and four-bead configurations are evaluated. For the multi-bead samples, the percent overlap ranged from 30 to 47 percent. The hardness and melt pool depth is affected by the percentage overlap. The number of beads impacts both of these features as well as the distortion. The distortion is influenced by the sample length[149]. Kim et al. conducted a comparison study of NAB (Ni-Al-Bronze) processed in casting and wire arc additive manufacturing. The WAAM deposited NAB performs better than the casted NAB in tensile, hardness, wear and impact tests. Also, observed that WAAM deposited NAB has anisotropy and has high tensile strength in the welding direction[150]. Chandramohan et al. investigated the effect of heat treatment of laser-sintered Ti–6Al–4V on wear and corrosion resistance. Rotary wear test was conducted at varying loads of 5N,15N, and 25 N at 25 m/s. The electrochemical corrosion behaviour of 1 M H_2SO_4, 1 M HCl, and 3.5 percent NaCl solutions was investigated. In all three media, heat-treated specimens outperform sintered specimens in corrosion resistance[151]. Wu et. al investigated morphology, microstructure, and mechanical properties of single and double arc additive manufacturing processes. The double-arc process deposition rate was 1.25 times greater than the single-arc method. Furthermore, the Vickers hardness and tensile strength of the double-arc sample were 0.6 percent and 3.5 percent greater than the single-arc samples, respectively[152]. Artaza et al compared the feasibility study of GMAW (gas metal arc welding) and PAW (plasma arc welding) on Mn_4Ni_2CrMo steel. When compared to the corresponding forging standard for the tested material, with values in the PAW process being 23% higher for UTS and 56% higher for elongation in the vertical direction when compared to GMAW [153].

Comez et al studied the corrosion behavior of dissimilar aluminum joints at different heat inputs using CMT. The dominant corrosion is in the form of pitting on the corrosion surfaces was observed. Corrosion resistance tended to rise as heat input increased. The corrosion resistance was optimum in the heat input values between 95 and 110 J/mm [154]. Sasahara et al. studied the dissimilar deposition of stainless steel and Ni alloy on a wire arc deposition welding station. As a consequence, the mechanical characteristics of the produced alloy were found to be equivalent to those of the bulk material. Also, recommended that the arc deposition process can be used to produce highly functional shapes made of different materials [87]. Nam et al. developed stainless steel and Fe functionally graded material using the direct energy deposition (DED) process. The authors observed that the prepared FGMs have pores at the interfaces[88].

Shen et al investigated the wire-arc additive manufacturing (WAAM) process to produce a functionally graded iron-aluminum with a composition ranging from 0% to 50%. The results of the experiments demonstrate that the WAAM technique used to produce iron aluminide functionally graded material with full density, appropriate composition, and adequate mechanical characteristics[89]. Unel et al investigated dissimilar joining of aluminum and steel using a robotic controlled cold metal transfer (CMT) welding process. The study explores the microstructure-strength connection while accounting for the heat input-intermetallic compound (IMC) layer formed between aluminum and steel after establishing the optimal process parameters based on the peak load for mechanically sound welds. Fe_2Al_5 and $FeAl_3$ phases were observed in the microstructure investigations[90]. Tian et al studied dissimilar material deposition of Al alloy on Ti alloy using a cold metal transfer based wire arc deposition process. The interface layer between the Ti and Al alloys was observed to have a continuous layer and a discontinuous layer. The modulus of elasticity and hardness between Al and Ti alloys were studied. The fracture is observed in the interfacial layer [91]. Wang et al. studied the influence of arc current on the microstructure, phase formation, microhardness transition, and dry-wear characteristics of NiTi and Ti6Al4V using the wire arc additive manufacturing (WAAM). Crack-free and dense coatings were produced and $NiTi_2$ phase with fine α Ti dendrites. This work demonstrates that the use of in-situ dual wire arc additive manufacturing of surface coatings for better wear resistance[92]. Zhu et al. investigate the laser cladding process factors that influence the microstructure growth of single pass and multi-pass cladding layers of Invar alloys. The top layer is made up of equiaxed crystals, whereas the bottom is made up of columnar crystals. The hardness of the cladding layer gradually decreases from top to bottom[93]. Yan et al. investigate the laser-wire deposition of 316 L stainless steel. Process optimization has been done to deposit multi-layer single-pass and single-layer multi-pass depositions. The deposited samples have epitaxial column growth also ferrite formations in the grain boundaries in their microstructure. Also found that the successive layers have cellular and columnar grains. The laser depositing products have plastic and ductile behaviour [94]. Sawant et al studied the deposition characteristics of single-track and multi-track deposition of Stellite 6 using the micro-plasma transferred arc powder deposition process. The most significant parameter that impacts energy and deposition material usage was found to be micro-plasma power. The dendritic microstructure of single-track deposition is finer than that of multi-track deposition[95]. Deshmukh et al investigate the multitrack deposition CO-Cr alloy using the Plasma Tungsten Arc Welding process. Process parameters were optimized to attain the minimum distortion and minimum surface residual stresses. Also, observed that there is a strong metallurgical bonding between the multi-tracks with no defects on the surface [96].

8.1.1. Scope of work

Many studies have suggested the morphology, microstructure, and mechanical performance of the wire arc deposition samples to achieve functional requirements. Most of the mechanical performance studies are tensile strength and hardness tests. Very few were attempted to study the compression characteristics, wear, and corrosion studies on the WAAM structures. In the present study, compression, corrosion, and wear studies are investigated on Inconel 625 and dissimilar deposition of SS and Inconel 625 samples.

8.2. Experimental method

In chapters 4 and 5, single track depositions are made using response surface experimental design methodology and process parameters are optimized. Later, trial and error experiments were conducted to study the multi-pass and overlapping effect on deposition quality and distortions. Trail experiments were conducted on the same Fronius made cold metal transfer welding machine as described in the previous chapters. Based on the optimized process parameters and trail experiments, multi-pass multi-track depositions are made to attain high quality and fully densified additive products. The process parameters used for the multipass multitrack depositions are 116 Amps current, 0.3 m/min weld speed and 5 mm standoff distance. From the literature, the bead overlapping is considered as 35%. The test samples were extracted from the deposited blocks using a wire cut EDM machine. The samples were prepared as per the ASTM standards as shown in Figure 8.1

All the samples were shaped and polished with emery papers to have a smooth surface finish. CH Instrument software was used to study the open circuit potential and Potentiodynamic polarization corrosion resistance experiments as shown in Figure 8.2a. The Tafel extrapolation is performed to estimate the corrosion resistance of the samples. The counter electrode was made platinum, while the reference electrode is silver chloride (AgCl) and the testing samples are working electrodes. The environmental conditions are 3.5% NaCl at 28 ± 2 °C r0om temperature. Before TAFEL exploration, an open circuit polarization test was conducted to estimate the stable potential. The polarization test was conducted in the range of 0.25 to 0.7 V, with a scan rate of 2 mV/s. Tribological studies were carried out on a dry abrasive wear test using a pin-on-disk machine shown in Figure 8.2b with varying loads of 20,30 and 40 N with a sliding velocity of 0.5 m/s and 500 m sliding distance. A universal tensile testing machine (Figure 8.2c) is used to conduct the compression test. A maximum of 80KN load is applied in the compression test.

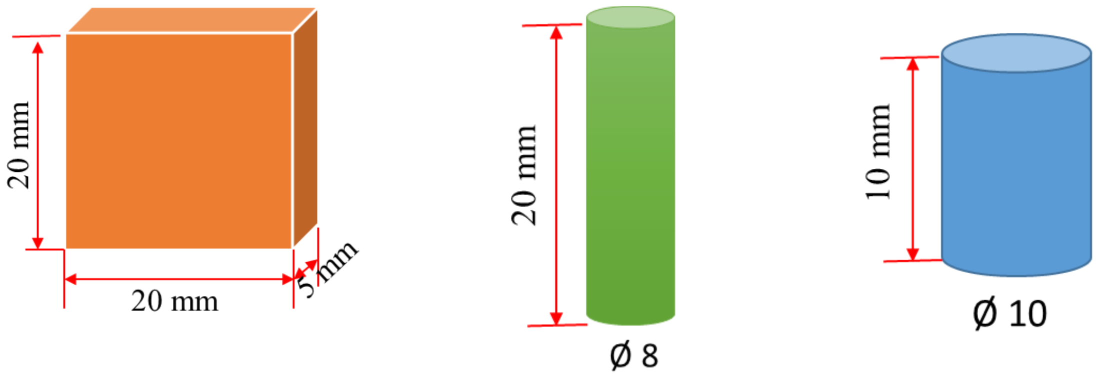

a) Corrosion test (ASTM: G59)

b) Wear test (ASTM: G99)

Compression test (ASTM: E99)

Figure 8.1 ASTM standards for testing a) Corrosion b) Abrasion Wear c) Compression

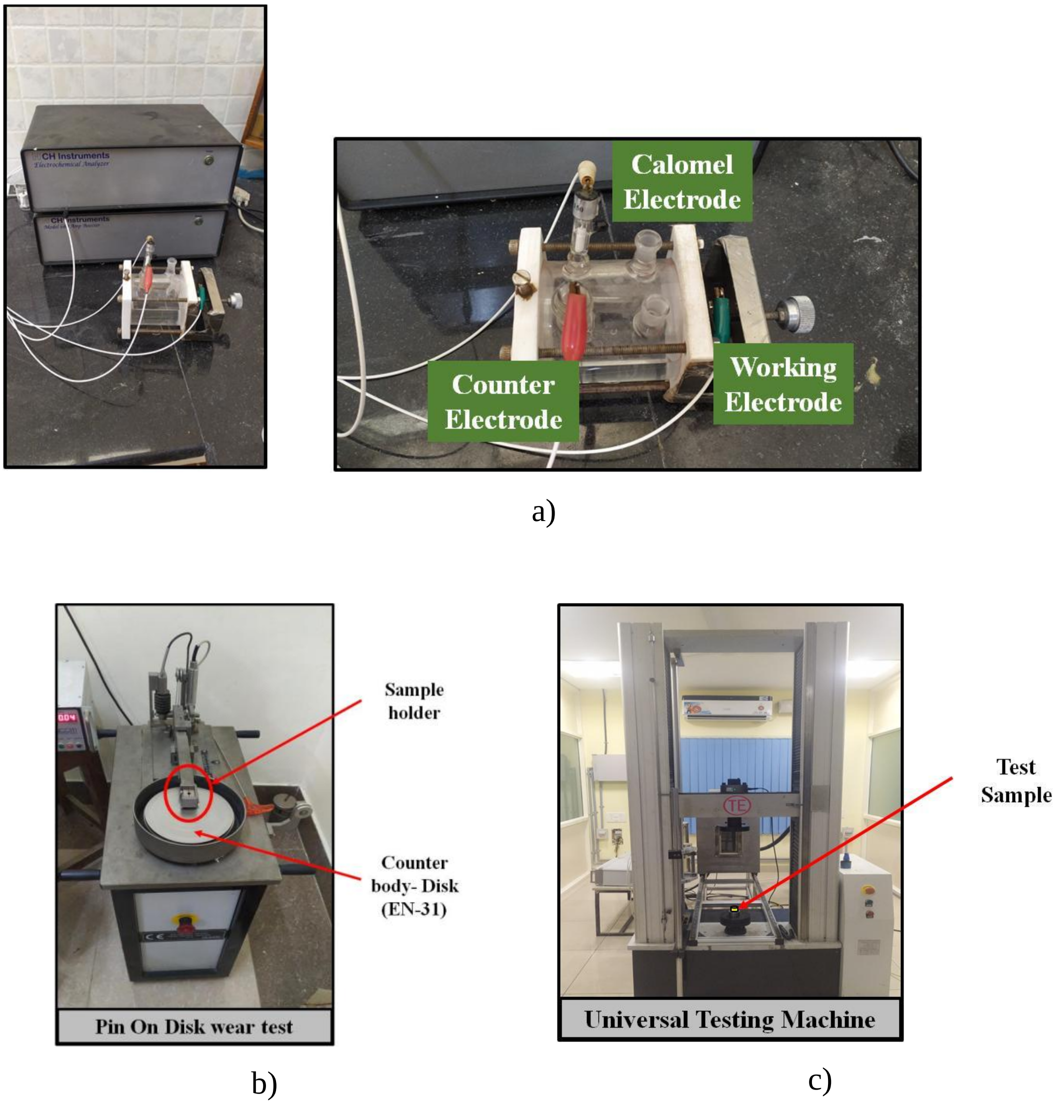

Figure 8.2 Test setup for a) Corrosion, b) Wear, and c) Compression

8.3. Results and discussion

A block of 150 X 50 X 75 mm^3 was successfully fabricated using a cold metal transfer welding machine. From the visual inspection, it is observed that the outer surface of the deposited blocks are irregular and too rough to use hence a final finishing process is required for functional requirements. Also, the bottom surfaces of the plates are distorted due to self weight as well as continuous heat supply through the preceding layers.

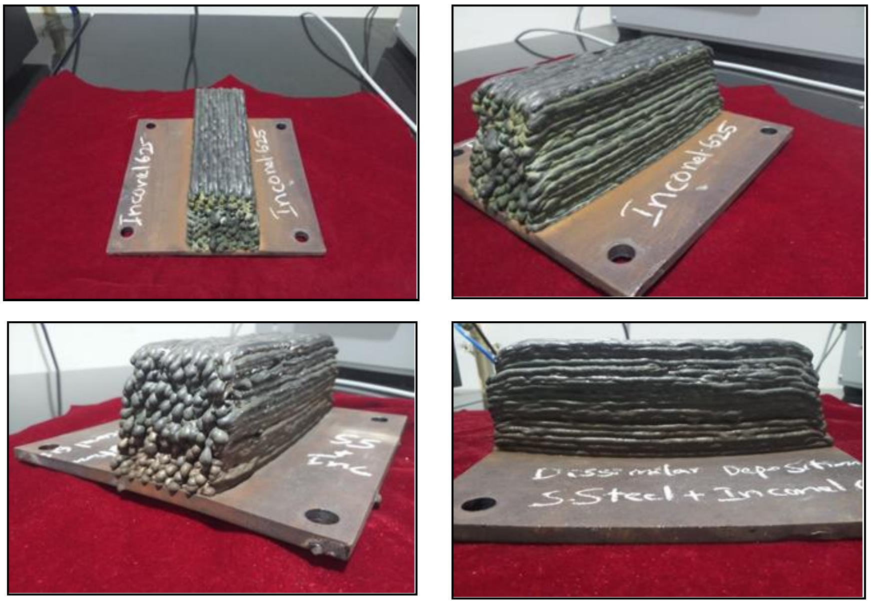

Figure 8.3 Multi track multi pass deposition block

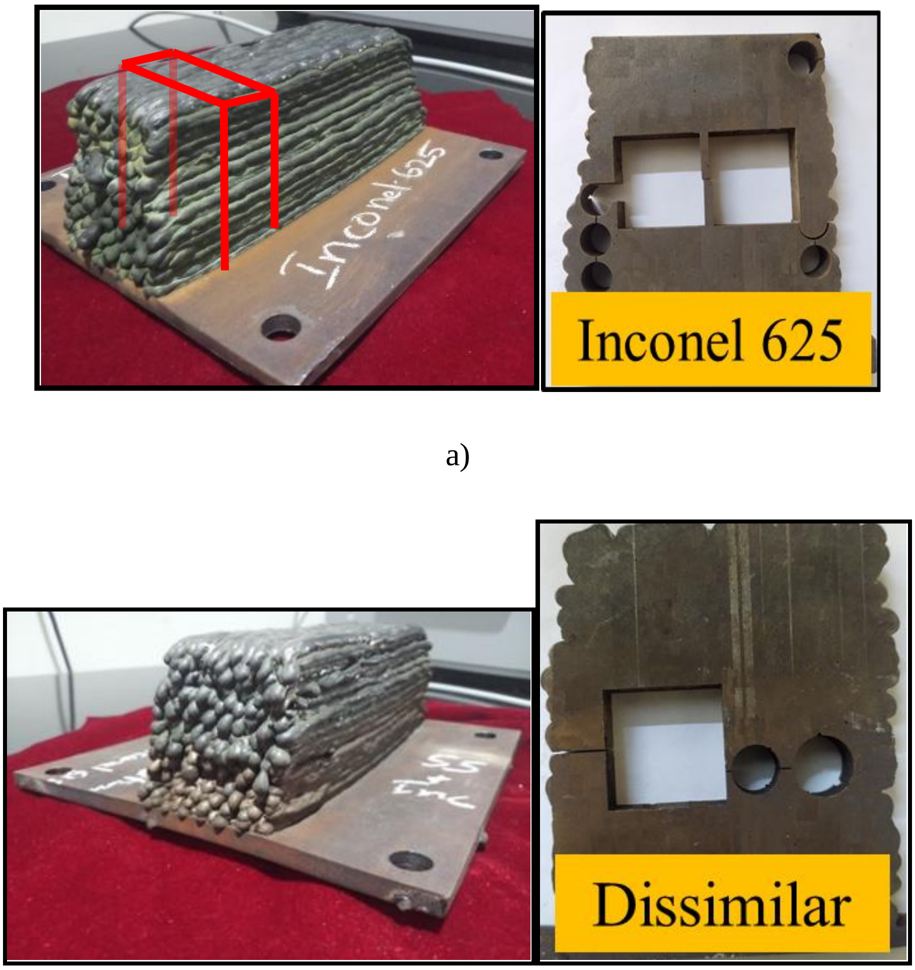

a)

b)

Figure 8.4 Extracted block for testing a) Inconel 625 b) Dissimilar deposition of Inconel 625 on SS 304

a) b) c)

Figure 8.5 Test samples a) corrosion b) wear c) compression

8.3.1. Corrosion studies

The open circuit potential (OCP) curves vs. time of immersion in 3.5% NaCl solutions of Inconel 625 and dissimilar deposition of Inconel 625 on SS 304 are shown in Figure 8.6. The OCP test was conducted in the range of -0.25 to +0.25 Volts. Open circuit potential was recorded in 3.5% NaCl. The stable OCP was observed after 1600 secs for Inconel 625 sample and 1700 secs for the dissimilar deposition sample. The increasing trend in the OCP curve indicates the resistance against chemical reactions. From this OCP tests estimate the potential at which the corrosion reactions are stable. And it is observed that the OCP for Inconel 625 sample is 0.305V and 0. 345V for dissimilar deposition samples.

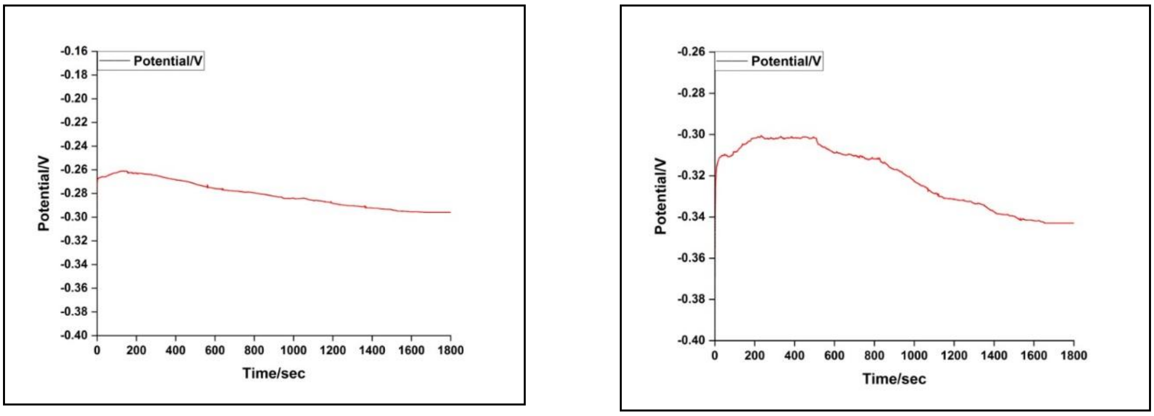

a) b)

Figure 8.6 Open circuit potential test for a) Inconel 625 and b) Dissimilar deposition

The OCP increases to more noble values without much fluctuation and a steady curve was recorded after 400 s. This indicates the formation of an early stable passive film on its surface. the OCP slopes down which indicate that passive film formation did not occur throughout immersion in the solutions. There are a lot of oscillations conveying a very weak form of a stable oxide layer on its surface, although, a small increase in potential is noticed in both specimens immersed in 3.5% NaCl. The Potentiodynamic polarization characteristics are observed using the TAFEL plot. The polarization curves were drawn at the scan rate of 2 mV/s in 3.5% NaCl solutions. The Potentiodynamic polarization curves immersed in 3.5% NaCl solutions are shown in Figure 8.7. All the specimens displayed an active-passive region with a steady passive region in 3.5% NaCl and fluctuating passive regions are observed. The corrosion rate (in mpy) was subsequently calculated using the following expression

$$\text{Corrosion rate (mpy)} = \frac{0.13 \times i_{corr} \times W_{eq}}{A\rho} \qquad (6.1)$$

Where ‘W_e’ is Equivalent weight (g), ‘ρ’ is density (g/cc), and ‘A’ is Area (cm^2).

For SS 304 - equivalent weight is 25.50 g/eq and density of 8.3 g/cm

For Inconel 625 - equivalent weight is 25.573 g/eq and density of 8.443 g/cm

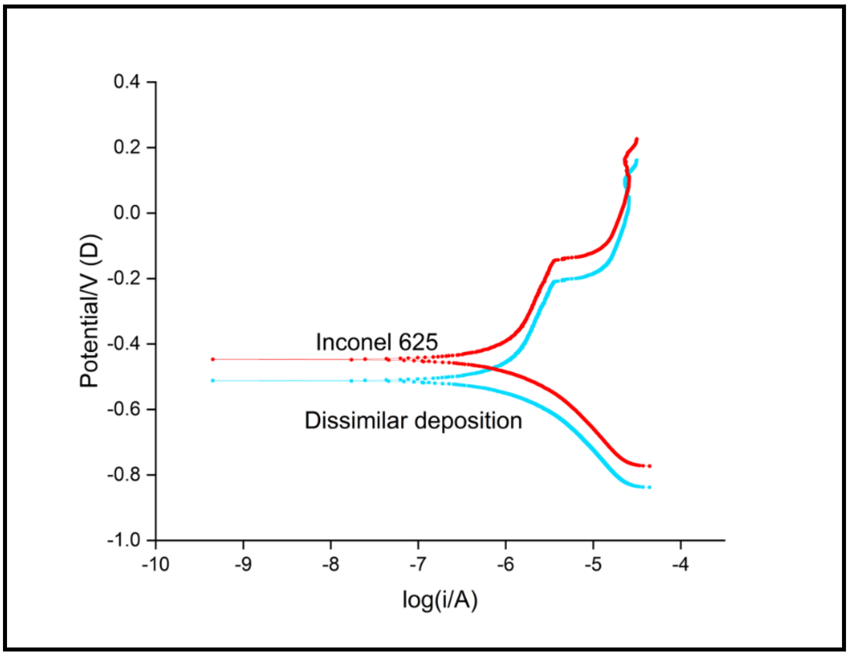

Figure 8.7 TAFEL Exploration curves for Inconel 625 and dissimilar deposition sample

Table 8.1 Potentio dynamic polarization characteristics in 3.5% NaCl solution

Details	**Inconel 625**	**Dissimilar deposition**
E_{corr} (V vs Ag-AgCl)	-1.425	-1.326
i_{corr} ($\mu A/cm^2$)	13.687	5.822
β_a (mV/decade)	660.07	183.722
β_c (mV/decade)	147.155	65.556
Corrosion rate (mm/y)	0.539	1.065

For Inconel 625 sample, the active-passive region was recorded at a higher potential (0.4 V) and followed by a fluctuating active region, while that of dissimilar deposition has a higher potential of 0.5 V and also having fluctuating active curves. From Table 8.1 using the Tafel extrapolation method, the corrosion current density, Icorr, for the samples immersed in 3.5% NaCl solution and found that the corrosion rate is minimum for Inconel 625 sample.

8.3.2. Wear studies

Figure 8.8 and Figure 8.9 show the wear performance as a function of material volume loss and specific wear rate at 20 N, 30 N and 40 N applied loads. The wear rate of the sample is calculated as below

$$\text{Wear Rate}\left(\frac{\text{mm}^3}{\text{m}}\right)=\frac{\text{Mass Loss/Density}}{\text{Sliding distance}}$$

From Table 8.2 It can be observed that wear volume loss is high in dissimilar deposition samples as compared Inconel 625 sample. The maximum volume loss was observed at 30 N of load. Generally, the wear volume loss of dissimilar deposition is more than Inconel 625 sample because of more grain refinement in the Inconel sample. The same can be applied to the hardness also. The maximum specific wear rate of 0.00000915 mm/Nm for the Inconel sample at 30 N whereas 0.00001358mm/Nm was observed for dissimilar deposition samples at 30 N.

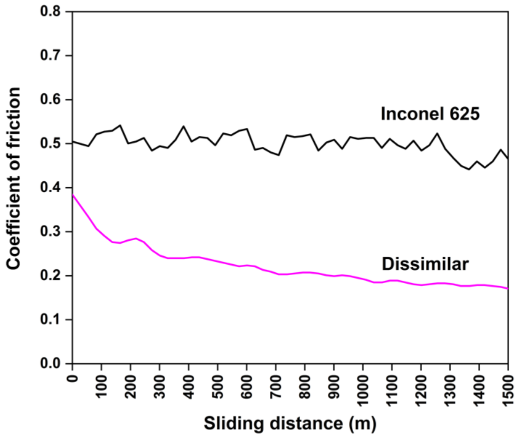

Figure 8.8 Coefficient of friction measurement

Table 8.2 Pin on disk wear test results

Sample	Load (N)	Weight (mm)		Material Loss (mm)	Specific Wear Rate (mm/Nm)
		Before	After		
Sample 1	20	3.43305	3.42928	0.00377	0.00000643
Sample 2	30	3.38427	3.37891	0.00536	0.00000915
Sample 3	40	3.43665	3.43305	0.0036	0.00000614
Dissimilar	30	3.47629	3.39668	0.07961	0.00001358

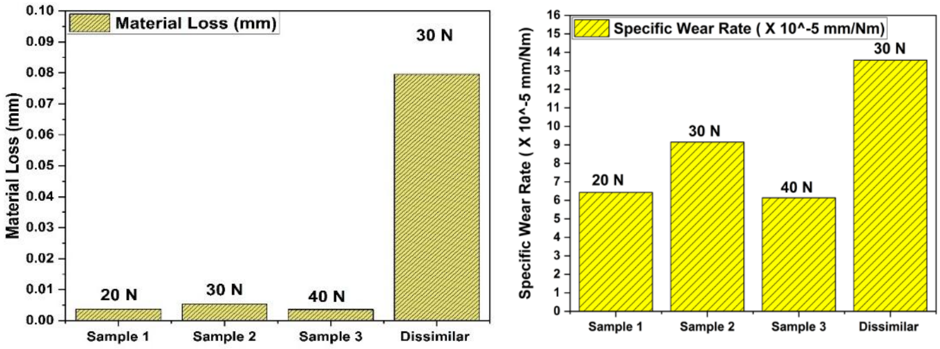

Figure 8.9 Wear in terms of a) material loss and b) specific wear rate

An increase in volume loss was observed as the load increases from 20 N to 30 N which suggests a gradual transformation from mild wear to severe wear.

8.3.3. Compression test results

Materials with high tensile strength appear to have poor compressive strength. Similarly, materials with strong compressive strength have low tensile strength. Compression testing is also used on porous materials like metals, polymers, ceramics, composites, concrete, and corrugated materials like cardboard. These materials are frequently employed in load-bearing applications, where their ability to withstand compressive stresses is critical. To measure the joint's mechanical reliability for structural performance, it's critical to look at the interfacial bond strength of bimetallic systems. Several test methods, including tensile, compressive, and shear loading, can be used in general. Compressive strength at the interface of bimetallic joints has rarely been tested. A compression test was conducted on a universal tensile testing machine. The stress strain curves plotted from the compression test data are shown in Figure 8.10.

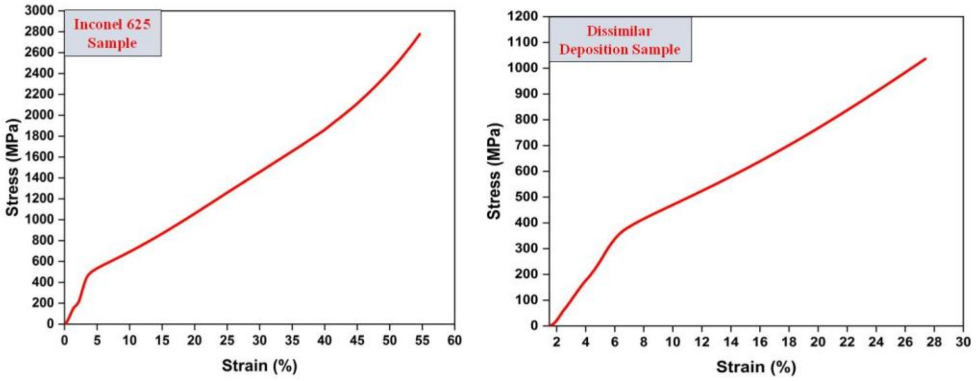

Figure 8.10 True stress and true strain response in compression of a) Inconel 625 b) Dissimilar deposition

Table 8.3 Compression test results

Parameter	Inconel 625	Dissimilar deposition
Yield stress	510 MPa	385 MPa
Young's Modulus	129.27 MPa	75.80 MPa
Elongation	54%	27%

Table 8.3 shows the compression test results of Inconel 625 and dissimilar deposition samples. The maximum yield strength of 570 MPa was found for Inconel 625 depositions whereas it is 385 Mpa for dissimilar deposition. Dissimilar deposition samples Inconel shares the interfacial region with stainless steel. The coefficient of thermal expansion is different for both the material there may be a chance of formation of crack or irregularities in the deposition surface layers.

8.3.4. Microstructure characterization

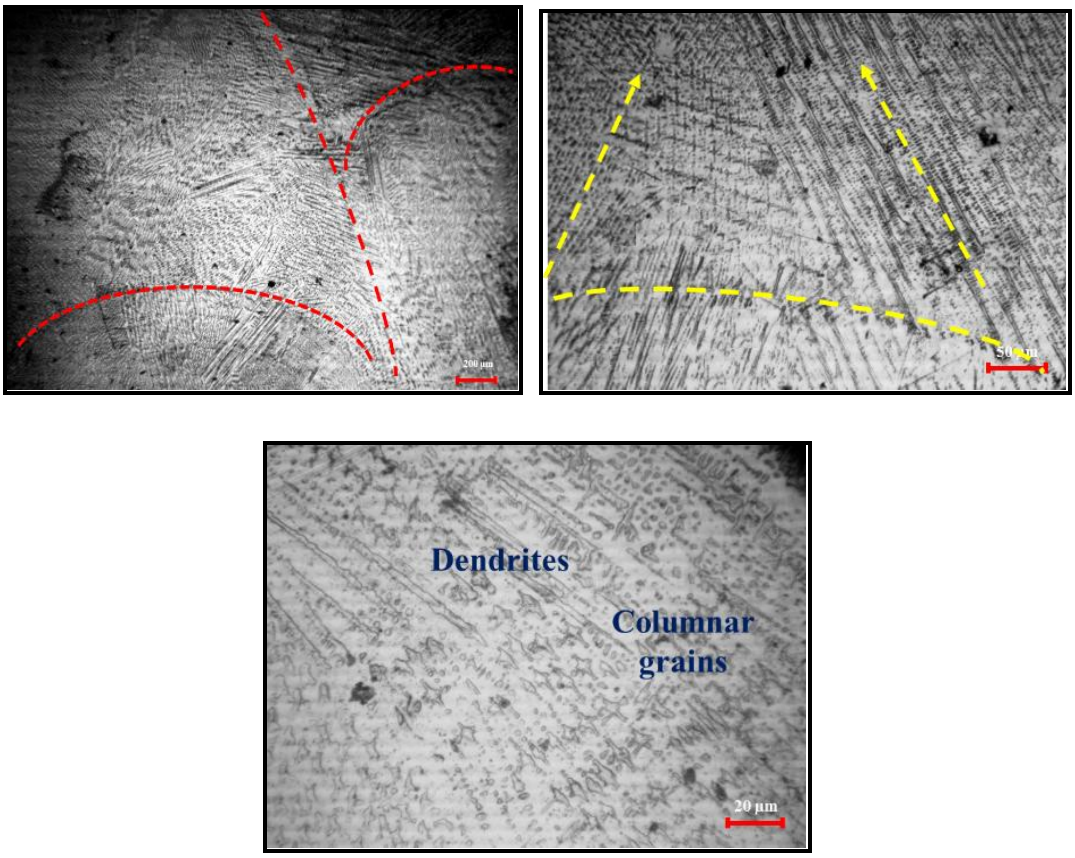

Figure 8.11 Microstructure of Inconel deposition

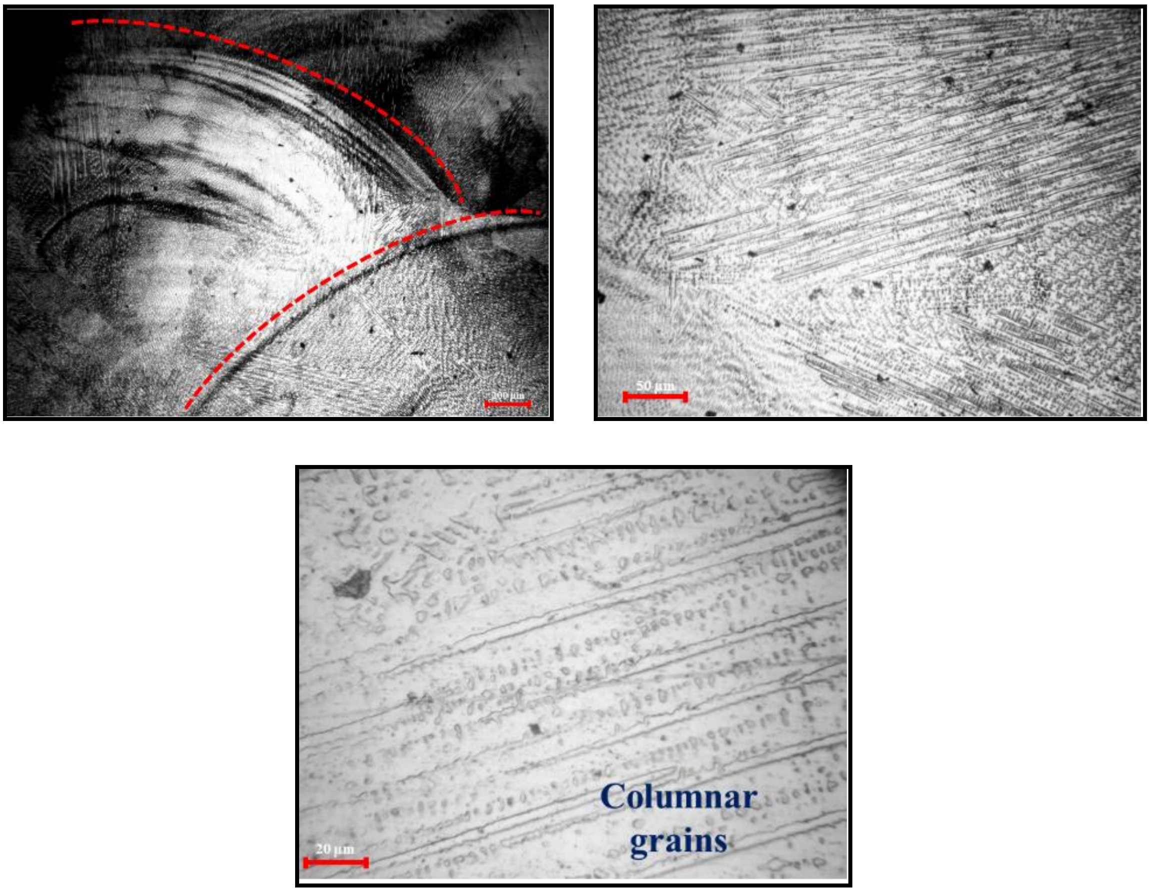

Figure 8.12 Microstructure of dissimilar deposition

The optical micrographs of the multi-pass multi-track deposition samples are shown in Figure 8.11 and Figure 8.12. The optical microscope study reveals the columnar grain structure in the microscope. The layered appearance has been identified on both the samples but is in an irregular direction. From the visual inspection, the samples were free from pores and cracks. While deposition, the deposition strategy has been changed to the opposite direction for each successive layer. Hence the direction of growth of grains is random. The substrate and previously deposited layers are the primary sources of cooling throughout the CMT additive manufacturing process, and each layer's deposit direction is vertical to that of the previously deposited layer, resulting in two neighboring layers with different travel directions. As a result, grain growth is somewhat skewed to the vertical direction. The material is remelted when a fresh layer is placed over the preceding layer, and new grains develop at the layer boundary.

As WAAM matures as a commercial manufacturing process, the development of a commercially available WAAM system for metal components is an interdisciplinary challenge, which integrates physical welding process development, materials science, and thermo-mechanical engineering, and mechatronics and control system design.

Selection of the most suitable welding WAAM process for the deposition material can ensure manufacturing process stability and contribute to the reduction of defects. For example, if the CMT-PADV process is used for producing aluminum parts, porosity defects can be dramatically reduced when compared to other GMAW modes. Moreover, integrated and reliable process monitoring and control systems are needed to maintain the stability of the process and ensure the quality of production. Usually, the bead geometry, interpass temperature, arc characteristics, and metal transfer behaviour are included in-process monitoring and control. Controlling the interpass temperature within a reasonable range is beneficial to microstructural evolution and the resulting mechanical properties. Further, regulating the arc characteristics and metal transfer behaviour in real time is helpful to process stability and avoidance of defects. Based on the process monitoring data that has been collected during deposition, one (or more) of several post-process treatments can be selected to mitigate defects and improve mechanical performance.

Considering the material characteristics, microstructural evolution and mechanical properties can also be optimized through a new feedstock composition design. the desired deposition microstructures can be obtained via adding specific alloying elements in the feedstock and subsequent mechanical properties improved. Moreover, the availability of wire mixing provides a potential possibility for building large functionally graded products for special applications. For example, twin-wire GTAW-based WAAM has been successfully developed to produce intermetallic graded materials. The development of new powder-cored wires will offer exciting opportunities for fabricating target components with accurate metal composition. In summary, using new welding consumables brings a cost-effective solution, which supports high deposition quality through obtaining the desired microstructures, lowering manufacturing costs by reducing or eliminating pre-weld cleaning and re-work, and providing safer working environments by reducing weld fumes[111].

8.4. Summery

Inconel 625 deposition and dissimilar deposition of Inconel 625 on SS 304 blocks are made using the optimized results from the single bead characteristics. Corrosion, compression, and wear samples were extracted from the deposition bed as per the ASTM testing standards. The findings of the test results are

- The corrosion characteristics are estimated by using TAFEL curves. The maximum corrosion rate of 1.065 mm/yr was observed for the Dissimilar deposition sample whereas it is 0.54 mm/yr for Inconel 625 sample

- The wear test was conducted for 20 N, 30N, and 40N load keeping sliding distance and sliding velocity constant at 500m and 0.5 m/s
- The maximum specific wear rate of 9.15x10^-5 mm/Nm has observed at 30N load and for dissimilar deposition, it was 13.58x10^-5 mm/Nm
- From the compression test, it is observed that dissimilar deposition sample has low young's modulus and yield strength than Inconel 625 sample.

Chapter 9

Conclusions

9.1. Global Inference

The difficult to manufacture and difficult to machine Inconel 625 alloy has been developed in the cold metal transfer based wire arc additive manufacturing process. Inconel 625 single bead deposition characteristics have been investigated extensively. The effect of process parameters on deposition characteristics and microstructural investigations are conducted on single bead deposition. Finally, with the optimized results an additive block of Inconel 625 and dissimilar deposition of Inconel 625 on Stainless steel was fabricated. The mechanical and metallurgical characteristics, wear, and corrosion strength was evaluated as per the ASTM standards. The key findings are given below:

- A fully dense single clad beads were successfully deposited using the cold metal transfer deposition process without any cracks and defects.
- The empirical models developed by regression analysis were able to predict the correlations between process variables and bead characteristics for the range of parameters (such as current: 90–110 A; Standoff distance: 4-6 mm and weld speed: 0.2-0.4 m/min) and material used in the present study.
- The bead characteristics are predominantly influenced by both main and interaction parameters effect and therefore their effects cannot be neglected.
- The optimum process parameters for minimum penetration, minimum dilution, maximum height, and maximum width for multipass multi-track depositions are found to be at current = 116.330 A, standoff distance = 5.115 mm, and weld speed = 0.4633 m/min.
- Grey relational analysis was applied to response surface design experiments to evaluate the multi-objective performance of bead characteristics. The deposition characteristics namely bead width, bead height, penetration, and microhardness are considered for the present study. From the GRA analysis, the simultaneous objective of maximum bead width, minimum height, and minimum penetration is observed at 100 Amperes current, 5 mm/min weld speed, and 0.3 mm standoff distance.
- From the cooling curve, it is observed that the cooling time has a linear relationship with heat input and the cooling rate.
- Bead width, penetration, dilution, deposition area, penetration area, the total area increased with current whereas bead height and contact angle decreased with the current.
- Bead height, penetration, deposition area, penetration area, total fusion area decreases with weld speed, also observed that there is no considerable change in contact angle with process parameters.

- The welding speed contributes more to melting efficiency as compared to current and standoff stand.
- Standoff distance does not influence melting efficiencies since it has no direct or indirect impact on heat input.
- Inconel 625 single beads were successfully deposited with varying heat input conditions. The heat input is attained by changing the travel speed of the torch during the deposition process. The deposited tracks were found to be free of crack and porosity and had good metallurgical bonding with the substrate.
- The obtained microstructure in all the samples was found to exhibit columnar dendritic structure and sometimes with primary dendrites. The columnar dendrite growth direction is mostly perpendicular to the substrate. The grains were sloping in the range of 51° to 64°. The columnar grains have a size of 3-10 µm. The interdendritic space has a distance of 5-13 µm. Also, fine grains are observed with an increase in heat input.
- During the solidification, the samples were enriched in Ni followed by Fe, Cr, Mo, Nb, and Ti. The elemental composition of Nb and Mo increases with heat input. Nb and Mo precipitates were formed in the form of the Laves phase.
- The fusion zone was found to have maximum hardness compared to other regions of the samples. Also, it was observed that the microhardness increases with an increase in the heat input. A maximum hardness of 234.7 HV was observed for heat input675.27 J/mm.
- Corrosion, compression, and wear samples were extracted from the deposition bed as per the ASTM testing standards The corrosion characteristics are estimated by using TAFEL curves. The maximum corrosion rate of 1.065 mm/yr was observed for the Dissimilar deposition sample whereas it is 0.54 mm/yr for Inconel 625 sample
- The wear test was conducted for 20 N, 30N, and 40N load keeping sliding distance and sliding velocity constant at 500m and 0.5 m/s. The maximum specific wear rate of 9.15x10^-5 mm/Nm has observed at 30N load and for dissimilar deposition, it was 13.58x10^-5 mm/Nm
- From the compression test, it is observed that dissimilar deposition sample has low Young's modulus and yield strength than Inconel 625 sample.

9.2. Recommendations for future work

Based on the present research work, observations, analysis, and conclusions the following may be recommended for future work.

There is a large scope of work in wire arc additive manufacturing systems in the view of materials development as well as fabrication facilities development. A few were noted below

- In the wire arc deposition process, the availability of raw material is a big problem for the fabrication process. Hence, there should be globally authorized methods and machines which will develop different types of wires.
- The effect of the deposition location on microstructure and mechanical properties can be studied.
- The experimental investigations further stretched to other materials like Titanium and its alloys. The inclusion of several materials in the investigation would lead to a generalized model with much wider applicability.
- The combined performance of deposited material characteristics can be studied with other multi-decision criteria models such as VIKOR, AHP, and TOPSIS.
- The material specific results can be used to produce customized and complex structures in the wire arc additive manufacturing process.
- Corrosion performance can be investigated with different parameters and corrosion environments (HNO_3, KOH, H_2SO_4, Biocompatible fluids, etc.). Wear studies can be enhanced with different machine specific parameters and counter body materials.

References

[1] *ISO/ASTM 52900(en) Additive manufacturing — General principles*. 2015.

[2] D. W. R. I. Gibson, B. Stucker, *Additive Manufacturing Technologies*. 2019.

[3] “Role of Additive Manufacturing in the Era of Industry 4.0,” 2019. [Online]. Available: https://amtechexpo.in/2019/05/20/role-of-additive-manufacturing-in-the-era-of-industry-4-0/.

[4] P. Friendly, “SmarTech Analysis Issues Latest Report on Metal Additive Manufacturing Market,” 2019. .

[5] A. S. Ivan Tabernero, Amagoia Paskual, Pedro Alvarez, “Study on Arc Welding Processes for High Deposition Rate Additive Manufacturing,” in *19th CIRP conference on Electro Physical and Chemical Machining*, 2018, pp. 358–362.

[6] J. P. Kruth, G. Levy, F. Klocke, and T. H. C. Childs, “Consolidation phenomena in laser and powder-bed based layered manufacturing,” *CIRP Ann. - Manuf. Technol.*, vol. 56, no. 2, pp. 730–759, 2007.

[7] Renishaw PLC, “Exchanging metal 3D printing solutions with HiETA,” 2017.

[8] B. L. Cherdo, “Metal 3D printers in 2020 : a comprehensive guide What is the best metal 3D,” 2020. [Online]. Available: https://www.aniwaa.com/buyers-guide/3d-printers/best-metal-3d-printer/.

[9] H. Qi, M. Azer, and P. Singh, “Adaptive toolpath deposition method for laser net shape manufacturing and repair of turbine compressor airfoils,” *Int. J. Adv. Manuf. Technol.*, vol. 48, no. 1–4, pp. 121–131, 2010.

[10] J. Li and H. M. Wang, “Microstructure and mechanical properties of rapid directionally solidified Ni-base superalloy Rene’41 by laser melting deposition manufacturing,” *Mater. Sci. Eng. A*, vol. 527, no. 18–19, pp. 4823–4829, 2010.

[11] J. Mazumder, A. Schifferer, and J. Choi, “Direct materials deposition: designed macro and microstructure,” *Mater. Res. Soc. Symp. - Proc.*, vol. 542, pp. 51–63, 1999.

[12] J. Mazumder, J. Choi, K. Nagarathnam, J. Koch, and D. Hetzner, “The direct metal deposition of H13 tool steel for 3-D components,” *Jom*, vol. 49, no. 5, pp. 55–60, 1997.

[13] M. Khan and P. Dickens, “Selective Laser Melting (SLM) of pure gold,” *Gold Bull.*, vol. 43, no. 2, pp. 114–121, 2010.

[14] C. P. Paul, P. Ganesh, S. K. Mishra, P. Bhargava, J. Negi, and A. K. Nath, “Investigating laser rapid manufacturing for Inconel-625 components,” *Opt. Laser Technol.*, vol. 39, no. 4, pp. 800–805, 2007.

[15] P. Ganesh *et al.*, “Fatigue and fracture toughness characteristics of laser rapid manufactured Inconel 625 structures,” *Mater. Sci. Eng. A*, vol. 527, no. 29–30, pp.

7490–7497, 2010.

[16] M. Agarwala, D. Bourell, J. Beaman, H. Marcus, and J. Barlow, "Direct selective laser sintering of metals," *Rapid Prototyp. J.*, vol. 1, no. 1, pp. 26–36, 1995.

[17] L. E. Criales, Y. M. Arısoy, B. Lane, S. Moylan, A. Donmez, and T. Özel, "Laser powder bed fusion of nickel alloy 625: Experimental investigations of effects of process parameters on melt pool size and shape with spatter analysis," *Int. J. Mach. Tools Manuf.*, vol. 121, no. March, pp. 22–36, 2017.

[18] A. Heralić, A. K. Christiansson, M. Ottosson, and B. Lennartson, "Increased stability in laser metal wire deposition through feedback from optical measurements," *Opt. Lasers Eng.*, vol. 48, no. 4, pp. 478–485, 2010.

[19] M. S. Domack, K. M. B. Taminger, and M. Begley, "Metallurgical mechanisms controlling mechanical properties of aluminum alloy 2219 produced by electron beam freeform fabrication," *Mater. Sci. Forum*, vol. 519–521, no. PART 2, pp. 1291–1296, 2006.

[20] P. M. Cordero, J. Mireles, S. Ridwan, and R. B. Wicker, "Evaluation of monitoring methods for electron beam melting powder bed fusion additive manufacturing technology," *Prog. Addit. Manuf.*, vol. 2, no. 1–2, pp. 1–10, 2017.

[21] J. Lin *et al.*, "Microstructural evolution and mechanical property of Ti-6Al-4V wall deposited by continuous plasma arc additive manufacturing without post heat treatment," *J. Mech. Behav. Biomed. Mater.*, vol. 69, no. June 2016, pp. 19–29, 2017.

[22] Y. Ma, D. Cuiuri, H. Li, Z. Pan, and C. Shen, "The effect of postproduction heat treatment on γ-TiAl alloys produced by the GTAW-based additive manufacturing process," *Mater. Sci. Eng. A*, vol. 657, pp. 86–95, 2016.

[23] J. Xiong, R. Li, Y. Lei, and H. Chen, "Heat propagation of circular thin-walled parts fabricated in additive manufacturing using gas metal arc welding," *J. Mater. Process. Technol.*, vol. 251, no. August 2017, pp. 12–19, 2018.

[24] J. Ge, J. Lin, Y. Lei, and H. Fu, "Location-related thermal history, microstructure, and mechanical properties of arc additively manufactured 2Cr13 steel using cold metal transfer welding," *Mater. Sci. Eng. A*, vol. 715, no. August 2017, pp. 144–153, 2018.

[25] M. J. M. Hermans and G. Den Ouden, "Process behavior and stability in short circuit gas metal arc welding," *Weld. J. (Miami, Fla)*, vol. 78, no. 4, pp. 137–141, 1999.

[26] T. A. V. Kumaran *et al.*, "Development of Pulsed Cold Metal Transfer and Gas Metal Arc Welding Techniques on High-Strength Aerospace-Grade AA7475-T761," *J. Mater. Eng. Perform.*, vol. 29, no. 11, pp. 7270–7290, 2020.

[27] B. Cong, J. Ding, and S. Williams, "Effect of arc mode in cold metal transfer process

on porosity of additively manufactured Al-6.3%Cu alloy," *Int. J. Adv. Manuf. Technol.*, vol. 76, no. 9–12, pp. 1593–1606, 2015.

[28] A. N. Jinoop, C. P. Paul, and K. S. Bindra, "Laser-assisted directed energy deposition of nickel super alloys: A review," *Proc. Inst. Mech. Eng. Part L J. Mater. Des. Appl.*, vol. 233, no. 11, pp. 2376–2400, 2019.

[29] J. Xu, J. Chen, Y. Duan, C. Yu, J. Chen, and H. Lu, "Comparison of residual stress induced by TIG and LBW in girth weld of AISI 304 stainless steel pipes," *J. Mater. Process. Technol.*, vol. 248, no. May, pp. 178–184, 2017.

[30] L. Ji, J. Lu, C. Liu, C. Jing, H. Fan, and S. Ma, "Microstructure and mechanical properties of 304L steel fabricated by arc additive manufacturing," *MATEC Web Conf.*, vol. 128, 2017.

[31] Q. Pham and J. Adler-nissen, "Response surface Related papers.".

[32] D. Ba and I. H. Boyaci, "Modeling and optimization i: Usability of response surface methodology," *J. Food Eng.*, vol. 78, no. 3, pp. 836–845, 2007.

[33] T. O. Educator, "Central Composite Design of RSM," pp. 1–6, 2021.

[34] S. Suryakumar, K. P. Karunakaran, A. Bernard, U. Chandrasekhar, N. Raghavender, and D. Sharma, "Weld bead modeling and process optimization in Hybrid Layered Manufacturing," *CAD Comput. Aided Des.*, vol. 43, no. 4, pp. 331–344, 2011.

[35] Y. Javid, "Multi-response optimization in laser cladding process of WC powder on Inconel 718," *CIRP J. Manuf. Sci. Technol.*, vol. 31, no. 2019, pp. 406–417, 2020.

[36] H. P. Van Thao Le, Dinh Si Mai, Tat Khoa Doan, "Wire and arc additive manufacturing of 308L stainless steel components_ .pdf," *Eng. Sci. Technol. , an Int. J.*, vol. 24, pp. 1015–1026, 2021.

[37] R. M. Kindermann, M. J. Roy, R. Morana, and P. B. Prangnell, "Process response of Inconel 718 to wire + arc additive manufacturing with cold metal transfer," *Mater. Des.*, vol. 195, p. 109031, 2020.

[38] T. E. Abioye, J. Folkes, and A. T. Clare, "A parametric study of Inconel 625 wire laser deposition," *J. Mater. Process. Technol.*, vol. 213, no. 12, pp. 2145–2151, 2013.

[39] L. Guo, H. Zheng, S. Liu, Y. Li, X. Xu, and C. Feng, "Formation quality optimization and corrosion performance of Inconel 625 weld overlay using hot wire pulsed TIG," *Xiyou Jinshu Cailiao Yu Gongcheng/Rare Met. Mater. Eng.*, vol. 45, no. 9, pp. 2219–2226, 2016.

[40] B. Cong, R. Ouyang, B. Qi, and J. Ding, "Influence of cold metal transfer process and its heat input on weld bead geometry and porosity of aluminum-copper alloy welds," *Xiyou Jinshu Cailiao Yu Gongcheng/Rare Met. Mater. Eng.*, vol. 45, no. 3, pp. 606–

611, 2016.

[41] S. Shen, I. N. A. Oguocha, and S. Yannacopoulos, “Effect of heat input on weld bead geometry of submerged arc welded ASTM A709 Grade 50 steel joints,” *J. Mater. Process. Technol.*, vol. 212, no. 1, pp. 286–294, 2012.

[42] K. Y. Benyounis, A. G. Olabi, and M. S. J. Hashmi, “Effect of laser welding parameters on the heat input and weld-bead profile,” *J. Mater. Process. Technol.*, vol. 164–165, pp. 978–985, 2005.

[43] R. Demarque, E. P. dos Santos, R. S. Silva, and J. A. de Castro, “Evaluation of the effect of the thermal cycle on the characteristics of welded joints through the variation of the heat input of the austhenitic AISI 316L steels by the GMAW process,” *Sci. Technol. Mater.*, vol. 30, pp. 51–59, 2018.

[44] A. A. de Resende, V. A. Ferraresi, A. Scotti, and J. C. Dutra, “Influence of welding current in plasma-MIG weld process on the bead weld geometry and wire fusion rate,” *Weld. Int.*, vol. 25, no. 12, pp. 910–916, 2011.

[45] M. Weglowski, “Effect of welding current on metal transfer in GMAW,” *Arch. Mater. ...*, vol. 33, no. 1, pp. 49–56, 2008.

[46] E. Karadeniz, U. Ozsarac, and C. Yildiz, “The effect of process parameters on penetration in gas metal arc welding processes,” *Mater. Des.*, vol. 28, no. 2, pp. 649–656, 2007.

[47] R. Zong, J. Chen, and C. Wu, “A comparison of TIG-MIG hybrid welding with conventional MIG welding in the behaviors of arc, droplet and weld pool,” *J. Mater. Process. Technol.*, vol. 270, no. February, pp. 345–355, 2019.

[48] Q. Wu, J. Lu, C. Liu, X. Shi, Q. Ma, and S. Tang, “Obtaining uniform deposition with variable wire feeding direction during wire-feed additive manufacturing Obtaining uniform deposition with variable wire feeding direction during wire-feed additive manufacturing,” vol. 6914, no. August, 2017.

[49] W. Wu, J. Xue, Z. Zhang, and P. Yao, “Comparative study of 316L depositions by two welding current processes,” *Mater. Manuf. Process.*, vol. 0, no. 0, pp. 1–7, 2019.

[50] G. P. Rajeev, M. Kamaraj, and S. R. Bakshi, “Effect of correction parameters on deposition characteristics in cold metal transfer welding,” *Mater. Manuf. Process.*, vol. 0, no. 0, pp. 1–12, 2019.

[51] H. Lee, C. Ji, and J. Yu, “Effects of welding current and torch position parameters on bead geometry in cold metal transfer welding,” *J. Mech. Sci. Technol.*, vol. 32, no. 9, pp. 4335–4343, 2018.

[52] N. Pavan Kumar, P. K. Devarajan, S. Arungalai Vendan, and N. Shanmugam,

"Prediction of bead geometry in cold metal transfer welding using back propagation neural network," *Int. J. Adv. Manuf. Technol.*, vol. 93, no. 1–4, pp. 385–392, 2017.

[53] S. S. Sravanthi, S. G. Acharyya, K. V. P. Prabhakar, and J. Joardar, "Effect of varying weld speed on corrosion resistance and mechanical behavior of Aluminium - steel welds fabricated by cold metal transfer technique," *Mater. Manuf. Process.*, vol. 0, no. 0, pp. 1–11, 2019.

[54] P. S. Sivasakthivel and R. Sudhakaran, "Modelling and optimisation of welding parameters for multiple objectives in pre-heated gas metal arc welding process using nature instigated algorithms," *Aust. J. Mech. Eng.*, vol. 4846, no. May, pp. 1–12, 2018.

[55] P. Shukla, B. Dash, D. V. Kiran, and S. Bukkapatnam, "Arc behavior in wire arc additive manufacturing process," *Procedia Manuf.*, vol. 48, no. 2019, pp. 725–729, 2020.

[56] R. W. Niles and C. E. Jackson, "Weld Thermal Efficiency of the Gtaw Process.," *Weld. J. (Miami, Fla)*, vol. 54, no. 1, pp. 25–32, 1975.

[57] P. J. Modenesi and R. I. Reis, "A model for melting rate phenomena in GMA welding," *J. Mater. Process. Technol.*, vol. 189, no. 1–3, pp. 199–205, 2007.

[58] L. Liu, C. Hu, S. Yu, and G. Song, "A triple-wire indirect arc welding method with high melting efficiency of base metal," *J. Manuf. Process.*, vol. 44, no. April, pp. 252–260, 2019.

[59] M. Suban and J. Tušek, "Dependence of melting rate in MIG/MAG welding on the type of shielding gas used," *J. Mater. Process. Technol.*, vol. 119, no. 1–3, pp. 185–192, 2001.

[60] R. Li *et al.*, "Optimization of the geometry for the end lateral extension path strategy to fabricate intersections using laser and cold metal transfer hybrid additive manufacturing," *Addit. Manuf.*, vol. 36, no. August, p. 101546, 2020.

[61] S. Li, Q. Wei, Y. Shi, C. K. Chua, Z. Zhu, and D. Zhang, "Microstructure Characteristics of Inconel 625 Superalloy Manufactured by Selective Laser Melting," *J. Mater. Sci. Technol.*, vol. 31, no. 9, pp. 946–952, 2015.

[62] J. Huebner, D. Kata, J. Kusiński, P. Rutkowski, and J. Lis, "Microstructure of laser cladded carbide reinforced Inconel 625 alloy for turbine blade application," *Ceram. Int.*, vol. 43, no. 12, pp. 8677–8684, 2017.

[63] M. Leary *et al.*, "Inconel 625 lattice structures manufactured by selective laser melting (SLM): Mechanical properties, deformation and failure modes," *Mater. Des.*, vol. 157, no. 2017, pp. 179–199, 2018.

[64] G. Marchese *et al.*, "Influence of heat treatments on microstructure evolution and

mechanical properties of Inconel 625 processed by laser powder bed fusion," *Mater. Sci. Eng. A*, vol. 729, no. May, pp. 64–75, 2018.

[65] C. Pleass and S. Jothi, "Influence of powder characteristics and additive manufacturing process parameters on the microstructure and mechanical behaviour of Inconel 625 fabricated by Selective Laser Melting," *Addit. Manuf.*, vol. 24, no. September, pp. 419–431, 2018.

[66] I. Koutiri, E. Pessard, P. Peyre, O. Amlou, and T. De Terris, "Influence of SLM process parameters on the surface finish, porosity rate and fatigue behavior of as-built Inconel 625 parts," *J. Mater. Process. Technol.*, vol. 255, no. December 2017, pp. 536–546, 2018.

[67] J. A. Gonzalez, J. Mireles, S. W. Stafford, M. A. Perez, C. A. Terrazas, and R. B. Wicker, "Characterization of Inconel 625 fabricated using powder-bed-based additive manufacturing technologies," *J. Mater. Process. Technol.*, vol. 264, no. August 2018, pp. 200–210, 2019.

[68] X. A. Hu, Z. Y. Xue, G. Le Zhao, J. Yun, D. Shi, and X. G. Yang, "Laser welding of a selective laser melted Ni-base superalloy: Microstructure and high temperature mechanical property," *Mater. Sci. Eng. A*, vol. 745, no. December 2018, pp. 335–345, 2019.

[69] G. P. Dinda, A. K. Dasgupta, and J. Mazumder, "Laser aided direct metal deposition of Inconel 625 superalloy: Microstructural evolution and thermal stability," *Mater. Sci. Eng. A*, vol. 509, no. 1–2, pp. 98–104, 2009.

[70] T. E. Abioye, D. G. McCartney, and A. T. Clare, "Laser cladding of Inconel 625 wire for corrosion protection," *J. Mater. Process. Technol.*, vol. 217, pp. 232–240, 2015.

[71] G. Marchese *et al.*, "The role of texturing and microstructure evolution on the tensile behavior of heat-treated Inconel 625 produced via laser powder bed fusion," *Mater. Sci. Eng. A*, vol. 769, no. October 2019, p. 138500, 2019.

[72] J. P. Oliveira, T. G. Santos, and R. M. Miranda, "Revisiting fundamental welding concepts to improve additive manufacturing: From theory to practice," *Prog. Mater. Sci.*, vol. 107, no. June 2019, p. 100590, 2019.

[73] O. G. Rivera *et al.*, "Microstructures and mechanical behavior of Inconel 625 fabricated by solid-state additive manufacturing," *Mater. Sci. Eng. A*, vol. 694, no. October 2016, pp. 1–9, 2017.

[74] J. F. Wang, Q. J. Sun, H. Wang, J. P. Liu, and J. C. Feng, "Effect of location on microstructure and mechanical properties of additive layer manufactured Inconel 625 using gas tungsten arc welding," *Mater. Sci. Eng. A*, vol. 676, pp. 395–405, 2016.

[75] S. S. Sandhu and A. S. Shahi, “Metallurgical, wear and fatigue performance of Inconel 625 weld claddings,” *J. Mater. Process. Technol.*, vol. 233, pp. 1–8, 2016.

[76] M. Naghiyan Fesharaki, R. Shoja-Razavi, H. A. Mansouri, and H. Jamali, “Microstructure investigation of Inconel 625 coating obtained by laser cladding and TIG cladding methods,” *Surf. Coatings Technol.*, vol. 353, no. April, pp. 25–31, 2018.

[77] K. Feng *et al.*, “Improved high-temperature hardness and wear resistance of Inconel 625 coatings fabricated by laser cladding,” *J. Mater. Process. Technol.*, vol. 243, pp. 82–91, 2017.

[78] H. R. Zareie Rajani and S. A. A. Akbari Mousavi, “The effect of explosive welding parameters on metallurgical and mechanical interfacial features of Inconel 625/plain carbon steel bimetal plate,” *Mater. Sci. Eng. A*, vol. 556, pp. 454–464, 2012.

[79] W. Yangfan, C. Xizhang, and S. Chuanchu, “Microstructure and mechanical properties of Inconel 625 fabricated by wire-arc additive manufacturing,” *Surf. Coatings Technol.*, vol. 374, no. October 2018, pp. 116–123, 2019.

[80] J. Wang, Z. Pan, G. Yang, J. Han, X. Chen, and H. Li, “Location dependence of microstructure, phase transformation temperature and mechanical properties on Ni-rich NiTi alloy fabricated by wire arc additive manufacturing,” *Mater. Sci. Eng. A*, vol. 749, no. February, pp. 218–222, 2019.

[81] X. Xu, J. Ding, S. Ganguly, and S. Williams, “Investigation of process factors affecting mechanical properties of INCONEL 718 superalloy in wire + arc additive manufacture process,” *J. Mater. Process. Technol.*, vol. 265, pp. 201–209, 2019.

[82] C. Gao, X. Chen, C. Su, and X. Chen, “Location dependence of microstructure and mechanical properties on wire arc additively manufactured nuclear grade steel,” *Vacuum*, vol. 168, no. July, p. 108818, 2019.

[83] K. Li, M. A. Klecka, S. Chen, and W. Xiong, “Wire-arc additive manufacturing and post-heat treatment optimization on microstructure and mechanical properties of Grade 91 steel,” *Addit. Manuf.*, vol. 37, no. November, p. 101734, 2021.

[84] T. A. Rodrigues *et al.*, “In-situ strengthening of a high strength low alloy steel during Wire and Arc Additive Manufacturing (WAAM),” *Addit. Manuf.*, vol. 34, no. January, p. 101200, 2020.

[85] C. E. Seow, H. E. Coules, G. Wu, R. H. U. Khan, X. Xu, and S. Williams, “Wire + Arc Additively Manufactured Inconel 718: Effect of post-deposition heat treatments on microstructure and tensile properties,” *Mater. Des.*, vol. 183, p. 108157, 2019.

[86] X. Xu, S. Ganguly, J. Ding, S. Guo, S. Williams, and F. Martina, “Microstructural evolution and mechanical properties of maraging steel produced by wire + arc additive

manufacture process," *Mater. Charact.*, vol. 143, no. November, pp. 152–162, 2018.

[87] T. Abe and H. Sasahara, "Dissimilar metal deposition with a stainless steel and nickel-based alloy using wire and arc-based additive manufacturing," *Precis. Eng.*, vol. 45, pp. 387–395, 2016.

[88] S. Nam, H. Cho, C. Kim, and Y. M. Kim, "Effect of process parameters on deposition properties of functionally graded STS 316/Fe manufactured by laser direct metal deposition," *Metals (Basel).*, vol. 8, no. 8, 2018.

[89] C. Shen, Z. Pan, D. Cuiuri, J. Roberts, and H. Li, "Fabrication of Fe-FeAl Functionally Graded Material Using the Wire-Arc Additive Manufacturing Process," *Metall. Mater. Trans. B Process Metall. Mater. Process. Sci.*, vol. 47, no. 1, pp. 763–772, 2016.

[90] E. Ünel and E. Taban, "Properties and optimization of dissimilar aluminum steel CMT welds," *Weld. World*, vol. 61, no. 1, pp. 1–9, 2017.

[91] Y. Tian, J. Shen, S. Hu, Z. Wang, and J. Gou, "Microstructure and mechanical properties of wire and arc additive manufactured Ti-6Al-4V and AlSi5 dissimilar alloys using cold metal transfer welding," *J. Manuf. Process.*, vol. 46, no. December 2018, pp. 337–344, 2019.

[92] J. Wang *et al.*, "In-situ dual wire arc additive manufacturing of NiTi-coating on Ti6Al4V alloys: Microstructure characterization and mechanical properties," *Surf. Coatings Technol.*, vol. 386, no. February, p. 125439, 2020.

[93] S. Zhu, C. Yu, Z. Chang, X. Zhan, and C. Zeng, "Microstructure Evolution Mechanism of Single and Multi-pass in Laser Cladding Based on Heat Accumulation Effect for Invar Alloy 1 Introduction."

[94] F. Yan, Y. Luo, and C. Wang, "A study of multi-layer multi-pass laser depositing with 316L stainless steel wire," *J. Mech. Sci. Technol.*, vol. 35, no. 4, pp. 1681–1687, 2021.

[95] M. S. Sawant and N. K. Jain, "Characteristics of Single-Track and Multi-track Depositions of Stellite by Micro-plasma Transferred Arc Powder Deposition Process," *J. Mater. Eng. Perform.*, vol. 26, no. 8, pp. 4029–4039, 2017.

[96] D. D. Deshmukh and V. D. Kalyankar, "Deposition Characteristics of Multitrack Overlayby Plasma Transferred Arc Welding on SS316Lwith Co-Cr Based Alloy-Influence ofProcess Parameters," *High Temp. Mater. Process.*, vol. 38, no. 2019, pp. 248–263, 2019.

[97] H. T. Lee and S. L. Jeng, "Characteristics of dissimilar welding of alloy 690 to 304L stainless steel," *Sci. Technol. Weld. Join.*, vol. 6, no. 4, pp. 225–234, 2001.

[98] J. H. Baek, Y. P. Kim, W. S. Kim, and Y. T. Kho, "Fracture toughness and fatigue crack growth properties of the base metal and weld metal of a type 304 stainless steel

pipeline for LNG transmission," *Int. J. Press. Vessel. Pip.*, vol. 78, no. 5, pp. 351–357, 2001.

[99] J. C. Lippold and D. J. Kotecki, "Welding metallurgy and weldability of stainless steels," *Choice Rev. Online*, vol. 43, no. 04, pp. 43-2230-43–2230, 2005.

[100] C. Yeni and M. Koçak, "Fracture analysis of laser beam welded superalloys Inconel 718 and 625 using the FITNET procedure," *Int. J. Press. Vessel. Pip.*, vol. 85, no. 8, pp. 532–539, 2008.

[101] E. Zumelzu, J. Sepúlveda, and M. Ibarra, "Influence of microstructure on the mechanical behaviour of welded 316 L SS joints," *J. Mater. Process. Technol.*, vol. 94, no. 1, pp. 36–40, 1999.

[102] J. Yan, M. Gao, and X. Zeng, "Study on microstructure and mechanical properties of 304 stainless steel joints by TIG, laser and laser-TIG hybrid welding," *Opt. Lasers Eng.*, vol. 48, no. 4, pp. 512–517, 2010.

[103] A. Durgutlu, "Experimental investigation of the effect of hydrogen in argon as a shielding gas on TIG welding of austenitic stainless steel," *Mater. Des.*, vol. 25, no. 1, pp. 19–23, 2004.

[104] R. Jones and V. Randle, "Sensitisation behaviour of grain boundary engineered austenitic stainless steel," *Mater. Sci. Eng. A*, vol. 527, no. 16–17, pp. 4275–4280, 2010.

[105] S. Lu, H. Fujii, and K. Nogi, "Arc ignitability, bead protection and weld shape variations for He-Ar-O2 shielded GTA welding on SUS304 stainless steel," *J. Mater. Process. Technol.*, vol. 209, no. 3, pp. 1231–1239, 2009.

[106] R. Unnikrishnan *et al.*, "Effect of heat input on the microstructure, residual stresses and corrosion resistance of 304l austenitic stainless steel weldments," *Mater. Charact.*, vol. 93, pp. 10–23, 2014.

[107] P. K. Palani and N. Murugan, "Development of mathematical models for prediction of weld bead geometry in cladding by flux cored arc welding," *Int. J. Adv. Manuf. Technol.*, vol. 30, no. 7–8, pp. 669–676, 2006.

[108] R. Aliyev, "A strategy for selection of the optimal machining sequence in high speed milling process," *Int. J. Comput. Appl. Technol.*, vol. 27, no. 1, pp. 72–82, 2006.

[109] W. Jin, C. Zhang, S. Jin, Y. Tian, D. Wellmann, and W. Liu, "Wire arc additive manufacturing of stainless steels: A review," *Appl. Sci.*, vol. 10, no. 5, pp. 1–28, 2020.

[110] J. V. Gordon and D. Gary Harlow, "Statistical Modeling of Wire and Arc Additive Manufactured Stainless Steel 304: Microstructure and Fatigue," *Int. J. Reliab. Qual. Saf. Eng.*, vol. 26, no. 4, pp. 2019–2020, 2019.

[111] B. Wu *et al.*, “A review of the wire arc additive manufacturing of metals: properties, defects and quality improvement,” *Journal of Manufacturing Processes*, vol. 35. pp. 127–139, 2018.

[112] Y. Tian, B. Ouyang, A. Gontcharov, R. Gauvin, P. Lowden, and M. Brochu, “Microstructure evolution of Inconel 625 with 0.4 wt% boron modification during gas tungsten arc deposition,” *J. Alloys Compd.*, vol. 694, pp. 429–438, 2017.

[113] B. Dong, Z. Pan, C. Shen, Y. Ma, and H. Li, “Fabrication of Copper-Rich Cu-Al Alloy Using the Wire-Arc Additive Manufacturing Process,” *Metall. Mater. Trans. B Process Metall. Mater. Process. Sci.*, vol. 48, no. 6, pp. 3143–3151, 2017.

[114] A. Dass and A. Moridi, “State of the art in directed energy deposition: From additive manufacturing to materials design,” *Coatings*, vol. 9, no. 7, pp. 1–26, 2019.

[115] A. V. Balan, T. Kannan, and N. Shivasankaran, “Effect of FCAW process parameters on bead geometry in super duplex stainless steel claddings,” *Int. J. Appl. Eng. Res.*, vol. 9, no. 24, pp. 27331–27346, 2014.

[116] T. Kannan and J. Yoganandh, “Effect of process parameters on clad bead geometry and its shape relationships of stainless steel claddings deposited by GMAW,” *Int. J. Adv. Manuf. Technol.*, vol. 47, no. 9–12, pp. 1083–1095, 2010.

[117] P. K. Palani and N. Murugan, “Optimization of weld bead geometry for stainless steel claddings deposited by FCAW,” *J. Mater. Process. Technol.*, vol. 190, no. 1–3, pp. 291–299, 2007.

[118] L. Tang and Y. F. Guo, “Electrical discharge precision machining parameters optimization investigation on S-03 special stainless steel,” *Int. J. Adv. Manuf. Technol.*, vol. 70, no. 5–8, pp. 1369–1376, 2014.

[119] M. Rsm, C. O. Laser, K. R. Milkey, A. R. Samsudin, A. K. Dubey, and P. Kidd, “Comparison between Taguchi Method and Response Surface,” *Jordan J. Mech. Ind. Eng.*, vol. 8, no. 1, pp. 35–42, 2014.

[120] Y. Wu, F. Zhou, and J. Kong, “Innovative design approach for product design based on TRIZ , AD , fuzzy and Grey relational analysis,” *Comput. Ind. Eng.*, vol. 140, no. August 2019, pp. 1062–76, 2020.

[121] C. J. Tzeng, Y. H. Lin, Y. K. Yang, and M. C. Jeng, “Optimization of turning operations with multiple performance characteristics using the Taguchi method and Grey relational analysis,” *J. Mater. Process. Technol.*, vol. 209, no. 6, pp. 2753–2759, 2009.

[122] K. S. Prakash, P. M. Gopal, and S. Karthik, “Multi-objective optimization using Taguchi based grey relational analysis in turning of Rock dust reinforced Aluminum

MMC," *Measurement*, vol. 157, 2020.

[123] B. Rajeswari and K. S. Amirthagadeswaran, "Experimental investigation of machinability characteristics and multi- response optimization of end milling in aluminium composites using RSM based grey relational analysis," *Measurement*, vol. 105, pp. 78–86, 2017.

[124] H. S. Lu, C. K. Chang, N. C. Hwang, and C. T. Chung, "Grey relational analysis coupled with principal component analysis for optimization design of the cutting parameters in high-speed end milling," *J. Mater. Process. Technol.*, vol. 9, pp. 3808–3817, 2008.

[125] F. Xu, S. Zhang, K. Wu, and Z. Dong, "Multi-response optimization design of tailor-welded blank (TWB) thin- walled structures using Taguchi-based gray relational analysis," *Thin-Walled Struct.*, vol. 131, no. April, pp. 286–296, 2018.

[126] S. P. Arun Kumar Srirangan, "Multi-response optimization of process parameters for TIG welding of Incoloy 800HT by Taguchi grey relational anaysis," *Eng. Sci. Technol. an Int. J.*, no. 19, pp. 811–817, 2016.

[127] M. Chen, Y. Ho, W. Hsiao, T. Wu, S. Tseng, and K. Huang, "Optimized laser cutting on light guide plates using grey relational analysis," *Opt. Lasers Eng.*, vol. 49, pp. 222–228, 2011.

[128] K. F. Tamrin, Y. Nukman, N. A. Sheikh, and M. Z. Harizam, "Determination of optimum parameters using grey relational analysis for multi-performance characteristics in CO 2 laser joining of dissimilar materials," *Opt. Lasers Eng.*, vol. 57, pp. 40–47, 2014.

[129] S. P. Shanmugarajan B, Rishabh Shrivastava, "Optimization of laser welding parameters for welding of P92 material using Taguchi based grey relational analysis," *Def. Technol.*, no. 12, pp. 343–350, 2016.

[130] L. Kwang, C. Chung, S. Long, and H. Feng, "Optimizing multiple quality characteristics via Taguchi method-based Grey analysis," *J. Mater. Process. Technol.*, vol. 182, pp. 107–116, 2007.

[131] V. Prajapati, J. J. Vora, S. Das, and K. Abhishek, "Study of parametric influence and welding performance optimization during regulated metal deposition (RMD ^{TM}) using grey integrated with fuzzy taguchi approach," *J. Manuf. Process.*, vol. 54, no. February, pp. 286–300, 2020.

[132] Y. S. Tarng, S. C. Juang, and C. H. Chang, "The use of grey-based Taguchi methods to determine submerged arc welding process parameters in hardfacing," *J. Mater. Process. Technol.*, vol. 128, pp. 1–6, 2002.

[133] H. K. Kohl and K. Peng, “Thermal stability of the superalloys Inconel 625 and Nimonic 86,” *J. Nucl. Mater.*, vol. 101, no. 3, pp. 243–250, 1981.

[134] K. Poorhaydari, B. M. Patchett, and D. G. Ivey, “Estimation of cooling rate in the welding of plates with intermediate thickness,” *Weld. J. (Miami, Fla)*, vol. 84, no. 10, 2005.

[135] R. S. Chandel, “Electrode melting and plate melting efficiencies of submerged arc welding and gas metal arc welding,” *Mater. Sci. Technol. (United Kingdom)*, vol. 6, no. 8, pp. 772–777, 1990.

[136] J. J. Valencia and C. T. Corporation, “Thermophysical Properties,” vol. 15, no. Ref 24, pp. 468–481, 2008.

[137] J. N. DuPont and A. R. Marder, “Thermal efficiency of arc welding processes,” *Weld. J. (Miami, Fla)*, vol. 74, no. 12, pp. 406-s, 1995.

[138] H. Y. Wan, Z. J. Zhou, C. P. Li, G. F. Chen, and G. P. Zhang, “Effect of scanning strategy on grain structure and crystallographic texture of Inconel 718 processed by selective laser melting,” *J. Mater. Sci. Technol.*, vol. 34, no. 10, pp. 1799–1804, 2018.

[139] D. Zhang, W. Niu, X. Cao, and Z. Liu, “Effect of standard heat treatment on the microstructure and mechanical properties of selective laser melting manufactured Inconel 718 superalloy,” *Mater. Sci. Eng. A*, vol. 644, pp. 32–40, 2015.

[140] J. S. Zuback and T. DebRoy, “The hardness of additively manufactured alloys,” *Materials (Basel).*, vol. 11, no. 11, 2018.

[141] J. Adamiec, “High temperature corrosion of power boiler components cladded with nickel alloys,” *Mater. Charact.*, vol. 60, no. 10, pp. 1093–1099, 2009.

[142] K. Devendranath Ramkumar *et al.*, “Studies on microstructure and mechanical properties of keyhole mode Nd:YAG laser welded Inconel 625 and duplex stainless steel, SAF 2205,” *J. Mater. Res.*, vol. 30, no. 21, pp. 3288–3298, 2015.

[143] J. Fuchs, C. Schneider, and N. Enzinger, “Wire-based additive manufacturing using an electron beam as heat source,” *Weld. World*, vol. 62, no. 2, pp. 267–275, 2018.

[144] J. C. Heigel, “Thermo-Mechanical Model Development and Experimental Validation for Directed Energy Deposition by,” p. 217, 2015.

[145] S. Wen and Y. C. Shin, “Comprehensive predictive modeling and parametric analysis of multitrack direct laser deposition processes,” *J. Laser Appl.*, vol. 23, no. 2, p. 022003, 2011.

[146] F. Mazzucato, A. Aversa, R. Doglione, S. Biamino, A. Valente, and M. Lombardi, “Influence of process parameters and deposition strategy on laser metal deposition of 316L powder,” *Metals (Basel).*, vol. 9, no. 11, pp. 11–14, 2019.

[147] L. E. Criales, Y. M. Arısoy, B. Lane, S. Moylan, A. Donmez, and T. Özel, "Predictive modeling and optimization of multi-track processing for laser powder bed fusion of nickel alloy 625," *Addit. Manuf.*, vol. 13, pp. 14–36, 2017.

[148] R. Ghorbel, A. Ktari, and N. Haddar, "Experimental analysis of temperature field and distortions in multi-pass welding of stainless cladded steel," *Int. J. Adv. Manuf. Technol.*, vol. 113, no. 11–12, pp. 3525–3542, 2021.

[149] P. Zareh and R. J. Urbanic, "Experimental analysis of single layer multi-track deposition of clad beads with variable overlap percentages," *Int. J. Adv. Manuf. Technol.*, vol. 109, no. 5–6, pp. 1511–1525, 2020.

[150] J. Kim, J. Kim, and C. Pyo, "Comparison of mechanical properties of ni-al-bronze alloy fabricated through wire arc additive manufacturing with ni-al-bronze alloy fabricated through casting," *Metals (Basel).*, vol. 10, no. 9, pp. 1–15, 2020.

[151] P. Chandramohan, S. Bhero, B. A. Obadele, and P. A. Olubambi, "Laser additive manufactured Ti – 6Al – 4V alloy : tribology and corrosion studies," pp. 3051–3061, 2017.

[152] W. Wu, J. Xue, and P. Yao, "A comparative study on single- and double-arc deposition processes," *Mater. Manuf. Process.*, vol. 35, no. 3, pp. 346–353, 2020.

[153] T. Artaza, A. Suárez, M. Murua, J. C. García, I. Tabernero, and A. Lamikiz, "Wire arc additive manufacturing of Mn4Ni2CrMo steel: Comparison of mechanical and metallographic properties of PAW and GMAW," *Procedia Manuf.*, vol. 41, pp. 1071–1078, 2019.

[154] N. Çömez and H. Durmuş, "Corrosion behavior and mechanical properties of cold metal transfer welded dissimilar AA7075-AA5754 alloys," *J. Cent. South Univ.*, vol. 27, no. 1, pp. 18–26, 2020.

Research outcomes

Papers published in journals

1) **D. T. Sarathchandra**, M.J. Davidson, "Process parameters effect on SS304 beads deposited by Additive Manufacturing", Materials and Manufacturing Process, Volume 35, 2020 - Issue 7 Pages 852-858 (SCI Indexed, IF: 3.35)
2) **D. T. Sarathchandra,** M.J. Davidson "Effect of heat input on mechanical and microstructural properties of single-pass deposition of Inconel 625 processed through wire arc additive manufacturing" Journal of Process Mechanical Engineering: SAGE Part E, 0(0) 1–10 DOI: 10.1177/09544089211004718 (SCI Indexed, IF: 1.60)
3) **D. T. Sarathchandra**, M.J. Davidson "Multi decision criteria optimization of Inconel 625 depositions for development of additive manufactured components using grey relational analysis*",* Metallurgical and Materials Engineering, https://doi.org/10.30544/586 (ESCI)
4) **D. T. Sarathchandra**, M.J. Davidson, "Effect of wire arc deposition parameters on bead geometry and melting characteristics of Inconel 625 superalloy" (Under communication)
5) **D.T. Sarathchandra,** M.J. Davidson**, "**Compression, wear, corrosion, and microstructure studies of dissimilar deposition of Inconel 625 on SS 304 processed wire additive manufacturing"(Under communication)

Papers presented in conferences

1. **D. T. Sarathchandra**, M.J. Davidson "Effect of processing errors on additively manufactured components" International Conference on Advances in Minerals, Metals, Materials, Manufacturing and Modelling (ICAM5-2019), NIT Warangal

2. **D.T. Sarathchandra**, M.J. Davidson "Grey relational multi decision analysis of SS304 bead characteristics processed in wire arc deposition process for additive manufacturing", International Conference on Recent Advances in Manufacturing (ICRAM-2020), SVNIT Surat

Brief Biography of the Candidate

Mr. Sarathchandra Dongari completed his undergraduate studies in Mechanical Engineering from Bapatle Engineering College, Bapatla, Guntur Dist, Andhrapradesh State (Acharya Nagarjuna University, India) in 2009. He obtained his Master degree in Mechanical Engineering - Manufacturing specialization from National Institute of Technology Warangal, Warangal, India in 2011. He worked as Engineer in Tech Mahindra Ltd, Hyderabad from 2011 to 2014. Currently, he is a Research Scholar at National Institute of Technology, Warangal, India. His major research interests are additive manufacturing, wire arc deposition process, optimization of manufacturing processes, multi criterion decision making and non conventional machining process etc.